Modelling Oxygen Permeability through Top coat and Thermally Grown Oxide in dense $Yb_2Si_2O_7$ Environmental Barrier Coatings

Sonia Singh

A thesis submitted to the Faculty of Engineering in partial fulfilment of the requirement for the degree of

MASTER OF APPLIED SCIENCE

in Advanced Materials and Manufacturing

Ottawa-Carleton Institute for Mechanical and Aerospace Engineering

University of Ottawa

Ottawa, Canada.

Abstract

Environmental barrier coatings (EBCs) are multi-layered systems used to protect hot section components of advanced gas turbine engines from aggressive environments. The state-of-art EBC system consists of a top coat and a bond coat applied on a ceramic substrate. While Ytterbium disilicate (YbDS) is the most used top coat material, Si or SiC are often preferred for the bond coat. During operation, a continuous influx of oxidants through the top coat often leads to reaction with the bond coat to form an additional silica (SiO_2) layer called thermally grown oxide (TGO). The growth kinetics of the TGO significantly affects the durability of EBCs. At a critical TGO thickness, the growth stresses exceed the SiO_2-bond coat interface strength, resulting in EBC spallation, exposure of the substrate, and eventual failure of the system.

The oxidant permeation is a key determinant of the TGO growth kinetics. Therefore, the main objective of this study is to investigate the oxidant diffusion through the EBC system using physics-based and numerical modelling. The oxygen permeability constants for YbDS top coat and TGO are systematically evaluated and quantified in terms of thermodynamics using defect reactions and the parabolic rate constant (kp), respectively. Dry and wet oxygen conditions as well as different temperatures, partial pressures and top coat modifiers are investigated.

The results offer evidence that the oxygen permeability constant for the YbDS top coat is an order of magnitude higher than for the TGO. As such, the TGO hinders the oxidant diffusion stronger, proving to be the diffusion rate controlling layer. Moreover, water vapor strongly increases the oxidant permeation with defect reactions playing a key role. It is suggested that the mass transfer through the top coat is primarily by outward

ytterbium ion diffusion and inward oxygen ion movement, with the latter being dominant, particularly in wet environments. The effect of top coat modifiers on oxidant permeation is composition sensitive and seems to be related to their interaction with oxygen ions and their mobility.

Acknowledgements

Two years are a time long enough to go through several different situations and sometimes troubles, and to realize that most of them would have been even more hard to overcome without people around me. For this reason, there are many people that deserve my gratitude for their scientific or human contribution to the realization of this thesis.

Firstly, It is a pleasure for me to express my gratitude to both my supervisors Dr. Michel Nganbe (Chair of the Department of Mechanical Engineering) and Dr. Kuiying Chen (Senior Research Officer, Aerospace Portfolio, NRC Ottawa) for their immense support and encouragement during my Master's thesis.

I would like to thank Dr. Kuiying Chen and Dr. Michel Nganbe for their guidance, inspiration, support and especially patience throughout this research work. Dr. Chen introduced me to the technical details and helped me to better understand every tiny detail of this field. Also, I would like to thank Dr. Michel Nganbe for his invaluable suggestions and brain-storming discussions. He always helped me to upgrade the way of writing and being patient in reading and correcting my thesis. We worked together as a team to tackle every technical difficulty. They have given me their precious time and guided me in optimizing my research. I am grateful to both for their faith in me.

I acknowledge the financial support from Dr. Chen and Dr. Nganbe in the form of Research Assistantship. Also, Dr.Nganbe extended his financial help by having me as his Teaching Assistant and offering an opportunity to be part of a project team, in the present pandemic (COVID-19) situation.

I would like to extend my gratitude to Ali Mansur and Ericsson Chenebuah for their moral support during my studies. A special thanks to Dr. Fabio Variola for having me his TA. Also, I would like to thank Alexander Steeves, Leon Guo, Alexis Tanner, and Dr. Nafisa Bano who helped me to understand the details of my TA duties.

Finally, I would like to thank my parents and my younger brother for their inspirational messages, support, and love. I am thankful to my fiancé Abhikaran Singh, for being by my side. Without their support and understanding, I would never have completed my work.

List of Abbreviations

APS	Air Plasma Spray
BC	Bond Coat
BSAS	Barium Strontium Aluminum Silicate
CMAS	Calcium-Magnesium-Aluminum Silicate
CMC	Ceramic Metal Matrix Composites
CTE	Coefficient of Thermal Expansion
CVD	Chemical Vapor Deposition
CVI	Chemical Vapor Infiltration
DFT	Density Functional Theory
EBC	Environmental Barrier Coating
EB-PVD	Electron Beam-Physical Vapor Deposition
FOD	Foreign Object Damage
MI	Melt Infiltrated
PS-PVD	Plasma Spray - Physical Vapor Deposition
RE	Rare Earth
SiC/SiC	SiC fiber reinforced SiC composites
SEM	Scanning Electron Microscope
SFC	Specific Fuel Consumption
TBC	Thermal Barrier Coatings
TC	Top Coat
T/EBCs	Thermal/Environmental Barrier Coatings
TGO	Thermally Grown Oxide
YbDS	Ytterbium Disilicate

YbMS	Ytterbium Monosilicate
YSZ	Yttria Stabilized Zirconia

Table of Contents

List of Figures

List of Tables

1 Introduction

With rapid advances in gas turbine engine technology, hot-section components are being exposed to an increasingly harsher environment with water vapor as one of inevitable combustion by-products. Water vapor has proven to substantially accelerate the oxidation of the bond coat, leading to more rapid formation and growth of the TGO. Consequently, experimental observations suggest that EBC protected Si based-CMC substrates can fail faster when exposed to water vapor containing environments compared to dry oxygen conditions. However, the prevailing fundamental oxidation mechanisms are still unexplored to date.

To address this challenge, there are continuous ongoing efforts to improve the design, material selection and coating systems for advanced gas turbine engines that are enabling even more exceptional high temperature capabilities. Thermodynamically, the engine performance increases with the inlet temperatures, which in turn provides important ecological and environmental benefits [1]. However, although current coating systems perform well at high temperatures, there are still considerable opportunities for further improvements as gas turbines remain far below the maximum hydrocarbon combustion temperatures [2]–[4].

In addition to the extremely high temperatures, materials used in turbine hot sections are subjected to thermal shocks, hot-corrosion, steep temperature gradients, and high-pressure gas. As such, in addition to accelerated oxidation and corrosion caused by water vapour, coating failures can occur due to thermal-mechanical loading, high temperature creep, and continuous loading-unloading fatigue [5] [6].

To meet such demanding requirements, advanced metal alloys (superalloys) and ceramics are either currently used or are being explored. Since decades, Ni-based or Co-based superalloys have been successful used with application temperatures around 1000°C [1] [3]. In such environments, ceramic coating systems such as multi-layered thermal barrier coatings (TBC) are the standard and allow the inlet temperature to increase by 140°C above the metal substrate melting point. Continuously increasing requirements for higher engine efficiencies lead to the never-ending improvement in the TBC systems. For example, TBC systems with an in-built cooling reported a total temperature increment of 250°C above the substrate melting point [7]. However, with the continuous increase in combustion temperatures, superalloys are reaching their limits [3].

Figure 1-1 displays the incremental evolution of high temperature materials and coating systems illustrating the potential of CMCs (Si-based and non-Si based) and EBCs for extremely high gas inlet temperature applications.

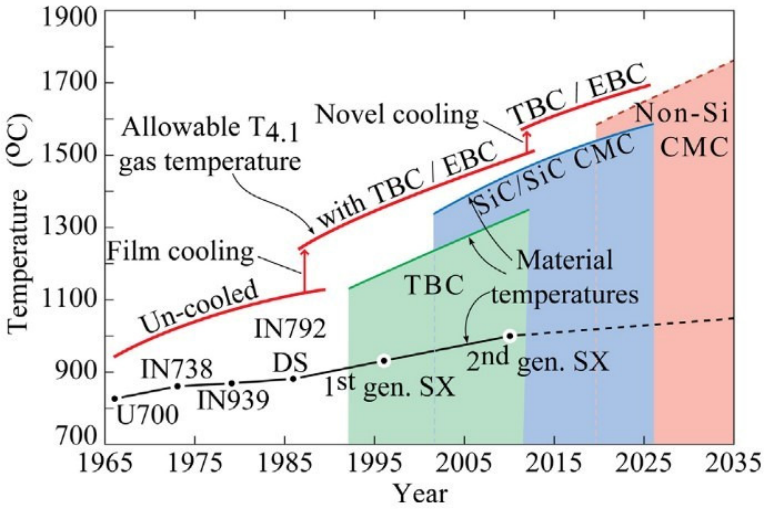

Figure 1-1: Evolution of gas turbine materials and coating systems versus inlet gas temperature ($T_{4.1}$). SX designates a single crystal superalloy [1].

To further enhance engine efficiency, ceramic metal matrix composites (CMCs) are being considered as replacement for superalloy substrates in hot-section applications. CMCs offer almost fifty percent weight reduction in comparison to Ni-based superalloys and enable higher thrust as well as two percent reduction in fuel consumption [1] [8]. They also have a higher melting point, appreciable resistance to penetration, good thermal shock resistance, and low density [9] [10].

Silicon carbide fiber reinforced silicon carbide matrix composites (SiC/SiC-CMCs) have proven to be a viable high-temperature ceramic material for engine hot section applications. In dry oxygen, they demonstrate high oxidation resistance due to the formation of a silica protective layer [1]. However, in water vapour containing combustion environments, this protective layer is prone to volatilization, which limits the application of uncoated SiC/SiC-CMCs [11]. Thus, additional oxidation and corrosion protection is needed, which is often in the form of a multi-layered coating system called Environmental Barrier Coating (EBC).

Like TBCs, EBCs consist of different layers including a top coat, an intermediate coat (if required), and a bond coat. These layers are required to have a low mismatch of coefficient of thermal expansion (CTE), limited surface recession in the combustion environment, good adherence, and phase stability along with chemical stability [12]. The material selection for each layer and the design of a robust EBC system have evolved into three generations. An additional layer of silica, called thermally grown oxide (TGO), generally grows between the top coat or the intermediate coat and the bond coat. This TGO layer constitutes an extra barrier limiting oxidant flux towards the CMC substrate. However, the TGO growth induces interface stresses. Once the TGO reaches a critical thickness, spallation of the whole EBC system can occur.

Furthermore, dense and crack-free EBC coatings are ideal to efficiently limit the permeation of the oxidants, such as oxygen and water vapour, through the top coat and TGO, thus protecting the SiC/SiC-CMCs from environmental degradation [12]. The presence of porosity and other defects can substantially affect this function.

Therefore, there is a need to further investigate EBC materials or processing techniques to control the TGO growth and improve EBC life. As such, EBC systems are still at an infant stage and a great deal of design optimizations is possible through both experimentation and simulation. In general, the conventional experimental approach involves lengthy sample preparation and expensive test set-ups. Its capacity to identify the active diffusion-controlling layer (TC or TGO) is also limited. In contrast, physics based and numerical modelling approaches are versatile and low-cost, allowing broader and more exploratory investigations. In the current case, modelling can enable to preliminarily elucidate the oxidation mechanisms, assess the performance, assist in material selection, and contribute in optimizing the coating structure [13].

To lay a better foundation for the current study, the following Literature Review chapter 2 enlightens the oxidation mechanism, oxygen permeability constant and key applicable equations. The Methodology is then described in Chapter 3 where a more profound elaboration on oxygen permeability constant equations for both the TC and the TGO is presented. The obtained Modelling Results are subsequently given in Chapter 4, followed by the Discussion in Chapter 5 to elaborate on the impact of different demand parameters and implications for EBC systems. The thesis closes with the Conclusions in Chapter 6 and suggestions for Future Work in Chapter 7.

2 Literature Review

2.1 Environmental Barrier Coatings (EBCs)

Environmental Barrier Coatings (EBCs) are known as prime-reliant coatings. Their function is to protect ceramic matrix composite (CMCs) substrates [4], such as Si-based CMC substrates that find application in hot-sections of advanced gas-turbine engines. Aggressive gas turbine conditions are created by high temperature and high pressure, as well as high speed water vapor flow. To sustain this aggressive environment, the Si-based CMC is covered with a dense EBC coating which hinders the diffusion or permeation of oxidants, and protects the substrate from recession or volatilisation [12]. Continuous improvements aim at prolonging the life-time of CMC components in aggressive combustion environment, by increasingly high temperature-resistant external barrier coatings or Environmental Barrier Coatings (EBCs) [14]. To date, the protective coating composition has evolved to its third generation. The selection of candidate materials is based strictly on the pre-requisites and key requirements. Parts of multilayer system are discussed in this work. Furthermore, the stability of EBC in the presence of water vapor is discussed in detail.

2.1.1 Ceramic Matrix Composites (CMCs)

Since 1970s, Si-based Ceramic Matrix Composites have been studied extensively as potential materials to replace the metallic components in gas turbines [15]. This is because Si-based Ceramic Matrix Composites are more stable at high temperatures [16] and have lower specific weight. They are classified as monolithic non-oxide ceramic matrix composites [17].

In late 1970s, SiC fiber reinforced SiC composites were fabricated using processes like chemical vapor infiltration (CVI-SiC/SiC), melt-infiltrated reaction sintering (MI-SiC/SiC), polymer infiltration and pyrolyzation (PIP-SiC/SiC) [18]. In contrast to monolithic silicon nitride (Si_3N_4) based composites that are prone to catastrophic failure because of low damage tolerance, carbon reinforced SiC matrix composites (C/SiC-CMCs) and silicon carbide reinforced silicon carbide matrix composites (SiC/SiC-CMCs) exhibit good toughness. Also, C/SiC-CMCs and SiC/SiC-CMCs have good thermal shock resistance and excellent wear resistance. Thus, Si-based CMCs can be seen as considerably reliable materials for high temperature applications such as hot section components of advanced gas turbines [3] and combustion liners, blade tracks or shrouds, and airfoil blades or vanes. Moreover, the final properties of CMC substrate depend on their microstructure that can be controlled by the choice of the manufacturing method. The cross-section of the Trent 1000 turbofan manufactured by the Rolls Royce Corporation is displayed in Figure 2-1 below.

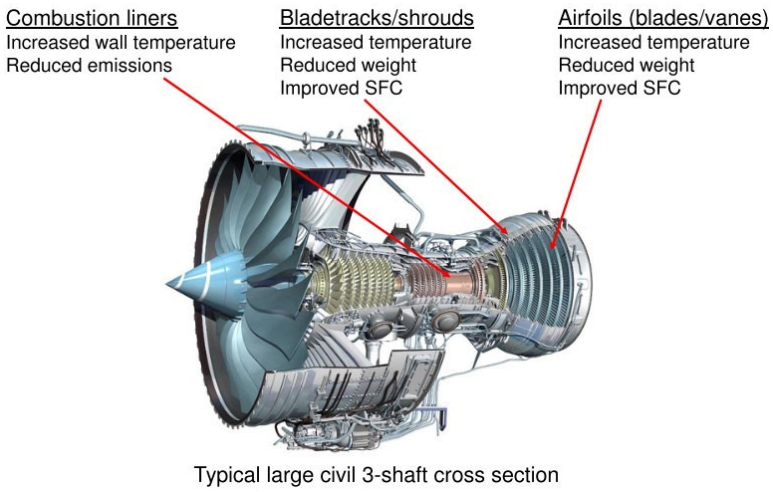

Figure 2-1: Cross-sectional view of a typical Trent 1000 turbofan with arrows pointing to SiC/SiC/-CMC substrates in combustion liners, blade tracks or shrouds, and airfoil blades or vanes [19].

In the Trent 1000 turbofan that is used for aero turbine engines, the combustion liners are made of SiC/SiC CMCs (non-oxide CMC), whereas oxide CMCs are often used in typical energy turbines. The main advantages for using SiC/SiC CMCs (in blade tracks or shrouds and airfoil blades or airfoil vanes) are increased inlet temperature, reduced engine weight, limited emissions, all of which enable lower specific fuel consumption (SFC) and improved engine efficiency [14].

It has been reported that CMCs have high oxidation resistance at high temperature in dry oxygen conditions. But in wet oxygen conditions such as those containing water vapor, they are prone to surface recession, and thus, can have limited durability. Water vapor is one of the by-products of fuel combustion reaction and constitutes about 10% of the operating environment in aero turbines. It was identified as the main cause of SiC recession [20].

In dry oxygen conditions, silicon reacts with oxygen according to Equation (2.1) to form a protective silicon dioxide (SiO_2) layer [21]:

$$SiC + 1.5O_2(g) = SiO_2 + CO(g) \quad (2.1)$$

Likewise, SiC can react with water vapor as shown in Equation (2.2) [14]. However, the formed silicon dioxide layer can further react with water vapor according to Equations (2.3) to (2.5) to form silicon hydroxide or silicon oxyhydroxide by-products that are volatile and can lead to the loss of environmental protection [20]. This phenomenon is known as surface recession.

$$SiC + 3H_2O\ (g) = SiO_2 + 3H_2(g) + CO\ (g) \quad (2.2)$$

$$SiO_2 + H_2O\ (g) = SiO(OH)_2(g) \quad (2.3)$$

$$SiO_2 + 2H_2O\ (g) = Si(OH)_4(g) \quad (2.4)$$

$$2SiO_2 + 3H_2O\ (g) = Si_2O(OH)_6(g) \qquad (2.5)$$

The ensuing simultaneous oxidation and surface recession can leave behind a porous SiO_2 layer. The developed porosity provides easy paths for oxidant diffusion to the SiC/SiC-CMC substrate. Figure 2-2 illustrates the oxidation, surface recession and porosity formation when the SiC/SiC-CMC substrate is in contact with combustion gases [15].

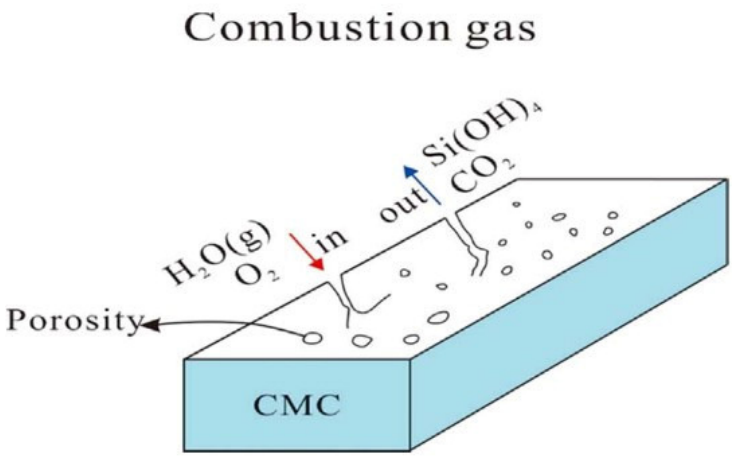

Figure 2-2: Schematic illustration of oxidation, surface recession and porosity formation in a SiC/SiC-CMC substrate in contact with combustion gases [15].

The logical solution to the surface recession is to insulate the SiC/SiC-CMC substrate from combustion gases. The insulation is achievable through the application of external protective coatings, mostly environmental barrier coatings. The primary function of such protective coatings is to hinder the oxidant diffusion, and prevent their interaction with the SiC/SiC-CMC substrate [22].

2.1.2 Evolution of Environmental Barrier Coatings

EBCs are a multilayer system whereby the layers are chemically and thermally compatible with each other and with the Si-based CMC substrate. Three generations of

EBC materials have been developed so far: the first generation is a bi-layer; the second generation EBC system is a tri-layer for enhanced stability; and the third generation can be either bi-layer or tri-layer depending on the final application. The EBC systems continue to evolve with increase in temperature capability as shown in Figure 2-3.

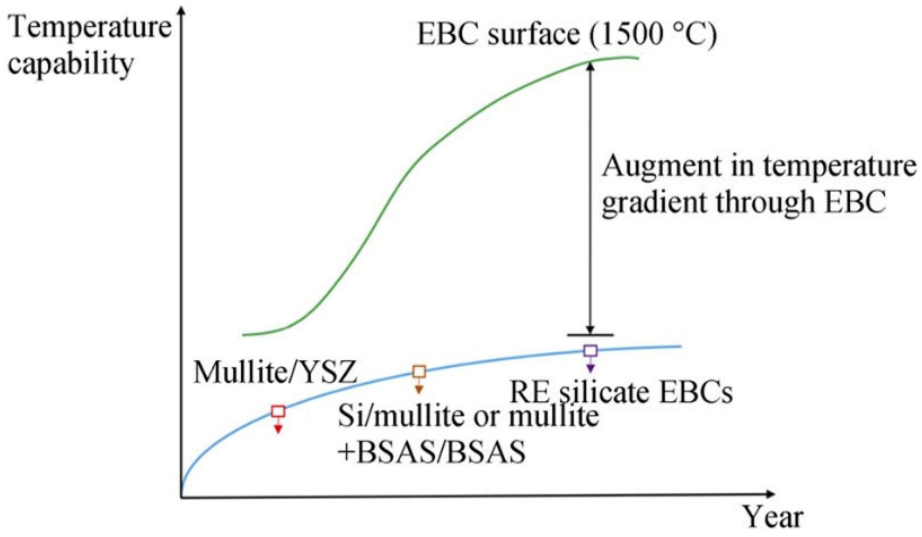

Figure 2-3: Evolution of EBC systems with increasing temperature capability of the used materials [6].

In 1990, the mullite coating ($3Al_2O_3.2SiO_2$ or $Al_6Si_2O_{13}$) was developed as the first generation EBC material for application on SiC/SiC-CMC substrates [4]. Mullite has impressive properties which make it a preferred material for the top coat. In comparison to the SiC/SiC-CMC substrate, mullite has comparable coefficient of thermal expansion (CTE), better chemical compatibility, and has excellent adherence [16] [23].

The main limitation of mullite coatings is delamination when exposed to thermal cycling conditions around 1000°C application temperature. In fact, mullite is amorphous when deposited on SiC/SiC-CMC at ambient temperature. At 1000°C however, mullite undergoes crystallisation leading to coating shrinkage accompanied

by crack formation (Figure 2-4), which results in eventual coating spallation [16]. Pre-heating plasma sprayed SiC/SiC-CMC substrates prior to mullite coating deposition to temperatures higher than the mullite crystallization temperature (~1000°C) was proven to be an effective solution. This constituted the second generation of mullite coatings with improved crack resistance and improved adherence [24]. Another limitation of mullite is its relatively high silica activity (~0.3-0.4), which means the selective reaction of silica with water vapor to form volatile silicon hydroxide that can result in porous mullite coatings. This puts considerable limitations on their application in wet environments [16]. A potential solution is the application of additional refractory protective coatings, such as refractory oxide, with low to no silica activity.

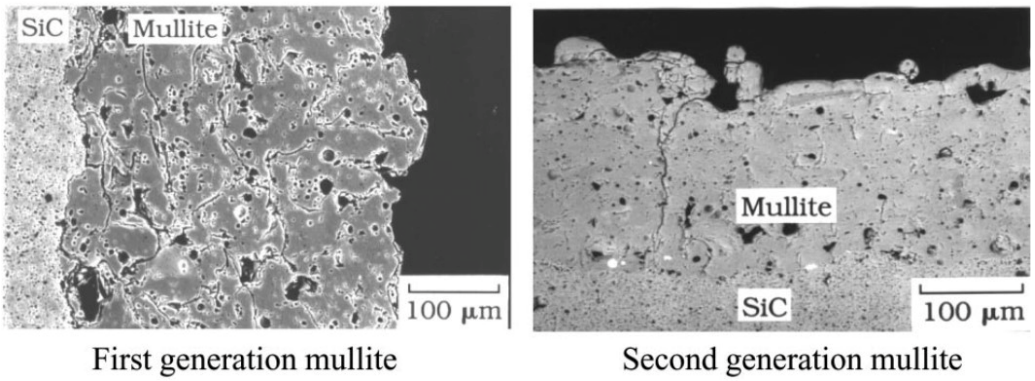

Figure 2-4: Comparative micrographs illustrating the considerable reduction in the amount of cracks and porosity in the second generation as compared to the first generation mullite coatings [25].

Basically, the first generation EBC systems were replicates of thermal barrier coating (TBC) systems. In TBC systems, the top coat material is often yttria-stabilized zirconia (7YSZ: $ZrO_2 + 7$ wt % Y_2O_3) and has proven effective in protecting a metallic substrate, in most cases superalloys. As such, it seemed logical to use yttria-stabilized zirconia as top coat in the first generation of environmental barrier coatings. First tests conducted

at temperatures up to about 1300°C yielded good results for a few hundred hours [16]. Also, 7YSZ coatings provided adequate protection against wet environments and proved relatively stable in water vapor. However, the considerably higher coefficient of thermal expansion (CTE) of 7YSZ coating compared to the SiC/SiC-CMC substrate was a great concern. The CTE mismatch and sintering at temperatures above 1200 °C promoted in-plane tensile stresses, followed by vertical cracks that provided easy pathways for oxidants to diffuse to the SiC/SiC-CMC substrates.

Second generation EBC systems consist of three layers: a bond coat (silicon based); an intermediate coat (mullite or mixture of mullite and BSAS); and a top coat (BSAS, Barium Strontium Aluminum Silicate ($1\text{-}xBaO\text{-}xSrO\text{-}Al_2O_3\text{-}2SiO_2$, $0 \leq x \leq 1$)) [16]. The BSAS top coat has excellent crack resistance, low CTE mismatch with Si-based CMC, low silica activity (below 0.1), low elastic modulus, and better environmental durability [23]. The low elastic modulus of BSAS reduces the in-plane tensile stress. Also, the mixture of BSAS and mullite as intermediate coat improves the crack resistance compared to mullite alone. Improved crack resistance enhances the coating stability in combustion environments. Furthermore, the silicon bond coat provides strong bonding between coating and substrate [25]. An application example of EBC coated SiC/SiC-CMC is the combustor liner in three Solar Turbines Centaur 50s gas turbine engines as shown in Figure 2-5.

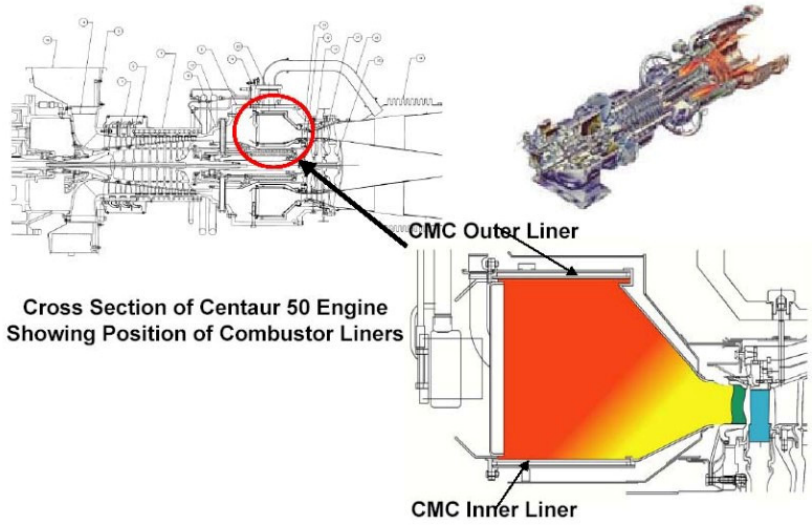

Figure 2-5: Use of the BSAS/BSASA+ mullite /Si coated SiC/SiC substrate in the Solar Centaur 50S combustor [4].

The system successfully completed the 14000 hours engine durability test [14] [16].

A key concern of BSAS coatings is its chemical reaction with silica (SiO_2, called thermally grown oxide, TGO). The BSAS-SiO_2 reaction forms low-melting glass near 1300°C, potentially leading to the premature degradation and failure of the EBC system [15]. Figure 2-6 (a) shows the cross-sectional view of a melt infiltrated (MI) SiC/SiC-CMC substrate with a BASA/Si (EBC system) exposed to 1300°C in 90% H_2O +10% O_2 wet oxygen for 100 hours. The test consisted of 2 -hour cycles. Figure 2-6 (b) is the magnified section of the area around a formed SiO_2-BASA glass phase, while Figure 2-6 (c) shows the BSAS-SiO_2 phase diagram illustrating the formation point of the low melting glass phase with the eutectic near 1311°C at 49 wt% SiO_2, which is expected to be similar to the BSAS-SiO_2 system [23].

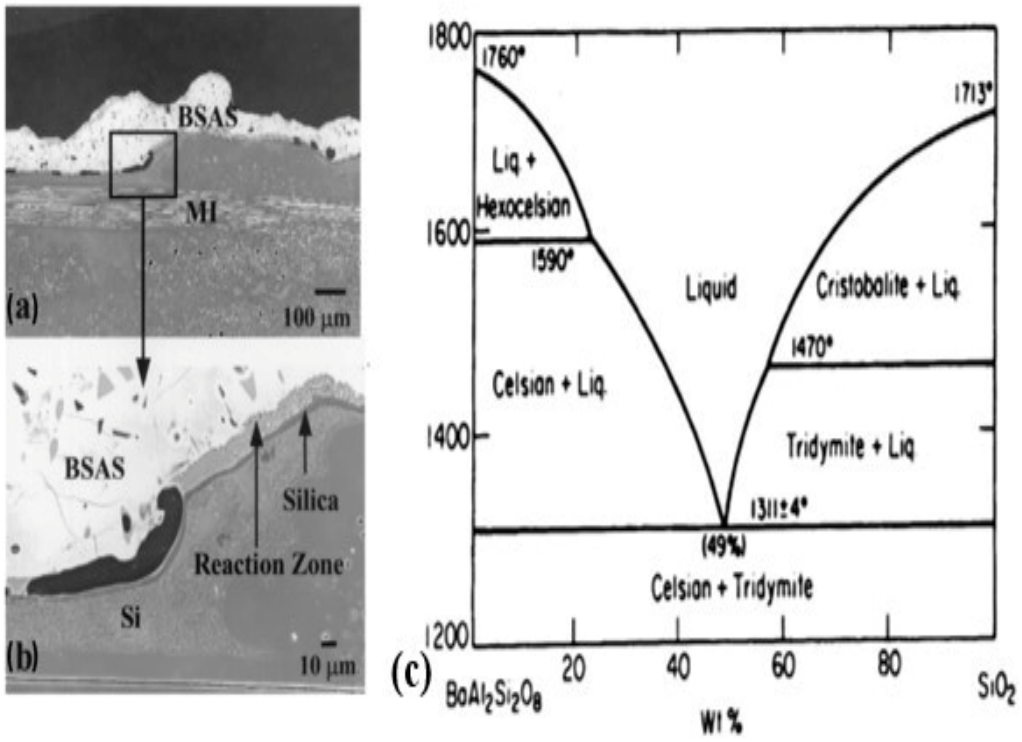

Figure 2-6: Illustration of the BSAS-SiO_2 reaction: (a) melt infiltrated SiC/SiC-CMC substrate coated with Si/BSAS EBC system after loading using 2 hour thermal cycles in 90%H_2O+10% O_2 at 1300°C for 100 h; (b) magnified section showing the formed low-melting glass phase; (c) BAS-SiO_2 phase diagram illustrating the eutectic at 49 wt% SiO_2 where the low melting glass phase forms [23].

The third generation EBC system has rare-earth-silicates as top coat. Rare earth silicates are more desirable thanks to properties like low silica activity, phase stability, and similar coefficient of thermal expansion to the Si-based ceramic substrates. In particular, rare earth silicates like yttrium, ytterbium, lutetium, and gadolinium are of high interest [26]. They have higher chemical stability compared to BSAS even in the presence of water vapor and are superior thermal insulators [16]. Their phase transformation takes place only at temperatures much higher than application conditions. They can be disilicates in the form of $RE_2Si_2O_7$, where RE stands for Y

(Yttrium), Tm (Thulium), Er (Erbium), or Ho (Holmium). However, disilicates often have various polymorphs with large density differences, which can make them unsuitable for EBC systems. In contrast, rare earth monosilicates are in the form RE_2SiO_5, with RE standing for Lu (Lutentium), Yb (Ytterbium), Y or Er. They have no polymorphs [27] and are, therefore, more appropriate as top coat materials in EBC systems. Lately, the tri-layer EBC system YbMS (ytterbium monosilicate)/mullite/Si has gained popularity. It has a low surface recession in the combustion environment and each of the three layers is thermo-chemically compatible within the EBC system [28].

Through thickness cracks or mud cracks or vertical cracks, as shown in Figure 2-7, are the main concerns for YbMS coatings. A potential solution is to apply Yb-disilicate (YbDS) to SiC/SiC-CMC substrates. This combination has a lower CTE mismatch, which substantially limits mud cracking [29]. The level of CTE mismatch between the individual layers and to the substrate determines the depth of vertical cracks in EBCs. In the case of SiC/SiC-CMC substrates, the vertical cracks are arrested either within the intermediate coat or at the intermediate coat/bond coat interface due to the low CTE of the bond coat (Si) compared to the SiC/SiC-CMC substrate. This low CTE of the bond coat develops compressive stresses that can stop the crack.

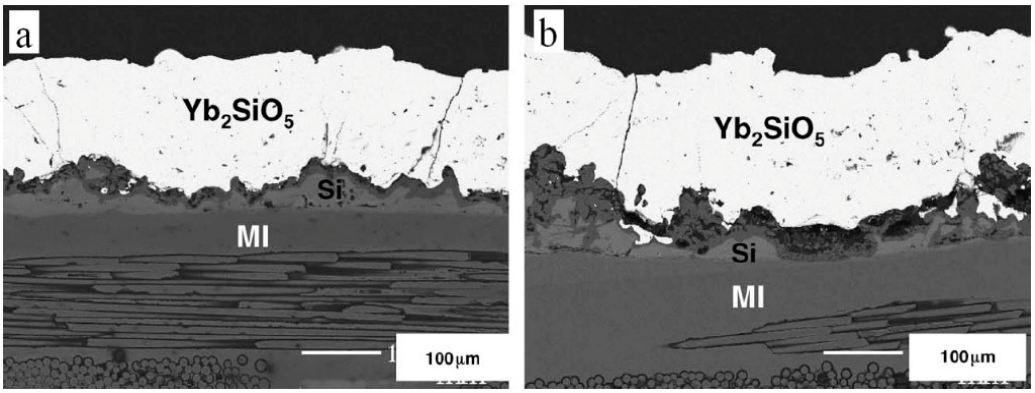

Figure 2-7: SEM images of through thickness mud cracks in EBC systems applied on melt infiltrated (MI) SiC/SiC composite: a) in silicon/mullite + SAS/Yb_2SiO_5; b) in silicon/mullite/ Yb_2SiO_5 [3].

In contrast, for the Si_3N_4 substrate, the vertical crack can travel through the entire EBC system to eventually stop only at the bond coat/substrate interface. This is due to the higher CTE of the Si bond coat compared to the Si_3N_4 - CMC substrate that develops tensile stresses within the bond coat, promoting crack propagation [3].

Overall, even though YbMS has a lower water vapor recession, YbDS is preferred as top coat because of its lower CTE mismatch. The CTE of ytterbium disilicate (4-6 × 10^{-6} $^{\circ}C^{-1}$) is similar to that of the SiC substrate (4.5-5.5×10^{-6} $^{\circ}C^{-1}$), whereas, the CTE of monosilicate ytterbium disilicate (7-8×10^{-6} $^{\circ}C^{-1}$) is quite higher compared to SiC substrate [17]. But, the comparatively high silica activity of the YbDS tends to promote reaction with water vapor to form YbMS. Thus, in wet environments, the YbDS top coat contains both disilicate and monosilicate phases of ytterbium. The YbDS top coat dominates near the bond coat interface, while the YbMS dominates at the external interface in immediate contact with water vapor.

Recently, beyond the evolution of EBC systems over three generations, to meet the rising demand of increasingly high temperature applications at up to 1700°C, hybrid thermal/environmental barrier coatings (T/EBCs) are proposed [9] [12] [30]. The thermal insulation coating (T) is applied on existing EBC systems as shown in Figure 2-8.

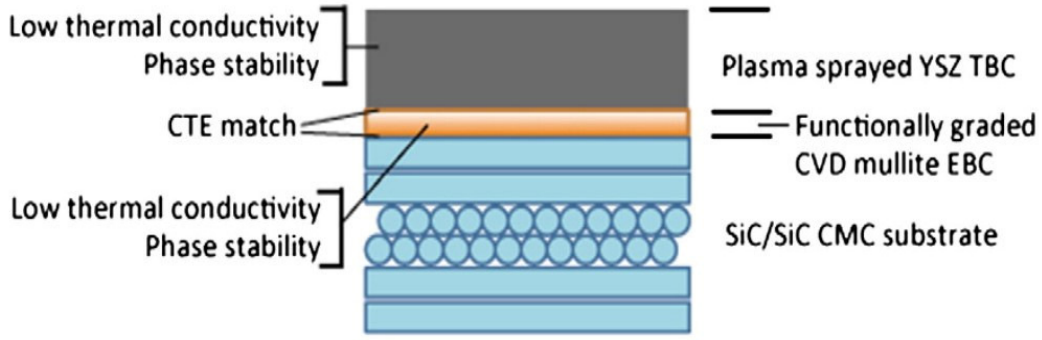

Figure 2-8: SiC/SiC CMC substrate with a T/EBC hybrid coating for high temperature applications up to 1700°C [9].

The considered thermal barrier coatings are mostly HfO_2 (Hafnium dioxide)-based and ZrO_2 (Zirconium dioxide)-based. But, the major concern is their larger CTE compared to EBCs. To confront this issue, a functionally graded intermediate layer can be applied between TBC and EBC [12].

2.1.3 Key requirements for the selection of the EBC materials

One of the biggest challenges of the EBC system is to find candidate materials that satisfy all the key design requirements [23] [25]. The bond coat (BC) is sandwiched between the substrate and the top coat (TC). It is designed to provide improved adherence to the SiC/SiC-CMC substrate, whereas the top coat protects from water vapor and provides additional thermal insulation. In most cases, pure silicon is used as

bond coat for SiC/SiC substrates because of their similar CTE: the CTEs of silicon and SiC/SiC CMC are 3.5-4.5 $\times 10^{-6}$ $^{\circ}C^{-1}$ and 4.5-5.5 $\times 10^{-6}$ $^{\circ}C^{-1}$, respectively.

Furthermore, depending on the final application requirements, additional layers can be introduced for specific functions like to facilitate chemical compatibility, for environmental durability, etc. Moreover, EBC systems are designed to restrict the diffusion of oxidants to the substrate [31]–[33]. The selection of candidate materials for each layer is based on the following criteria [14]:

a. Adherence:

The top coat refractory oxide can often not readily adhere to the SiC/SiC-CMC substrate. Therefore, an additional layer of bond coat is often used to achieve good adhesion. Till date, Si has proven to be among the most efficient bond coat materials for Si-based CMC substrate. Silica formation, often in the form of thermally grown oxide at the silicon bond coat / top coat interface can provide additional oxidation resistance [14].

b. Coefficient of Thermal Expansion (CTE):

As EBC systems are exposed to thermal cycles for prolonged periods of time, the CTE mismatch between the coating and the base substrate may lead to the premature failure of the whole system. Therefore, the basic criterion for the material selection of different EBC layers is to have a similar CTE compared to the base substrate. Conventional refractory oxides like ZrO_2, HfO_2, and Al_2O_3 (Alumina) have high CTE compared to Si-based CMCs, and are, therefore, less appropriate. In contrast, the CTE of Y_2SiO_5, mullite, and BSAS is comparable to that of Si-based CMCs as shown in Figure 2-9 and Table 2-1 [14], making them more appropriate as top coat materials.

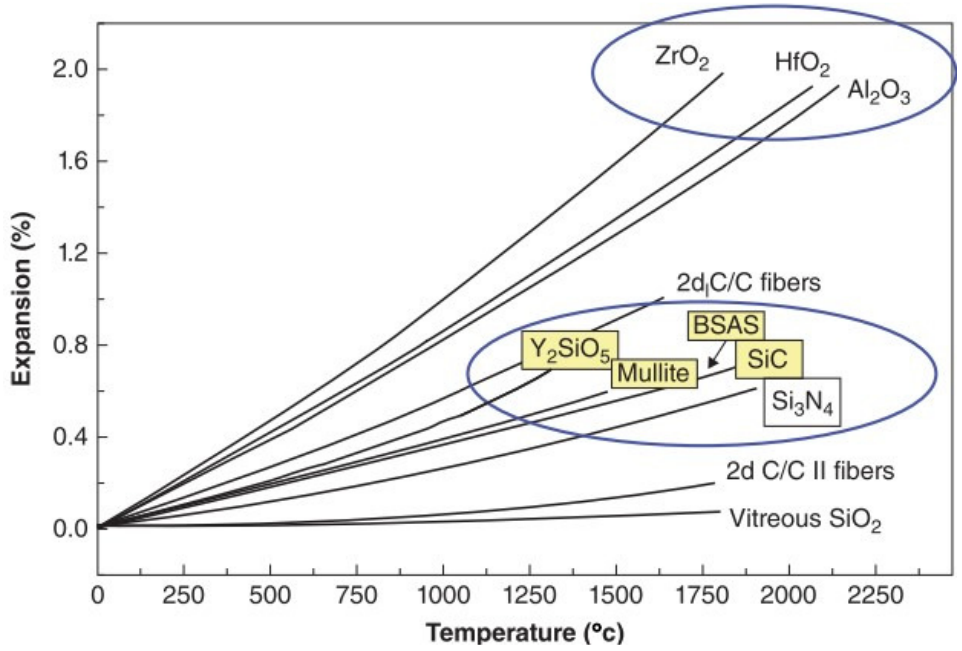

Figure 2-9: Thermal expansion percentage for refractory oxides compared to SiC and Si_3N_4 substrate materials [14].

Table 2-1: Coefficient of thermal expansion, melting temperatures and application of EBC coating materials [14].

Material	CTE ($\times 10^{-6}$ °C^{-1})	Melting Point (°C)	Application
Y_2SiO_5	5–6	1980	
Er_2SiO_5	5–7, 7–8[a]	1980	
Yb_2SiO_5	3.5–4.5, 7–8[a]	1950	
$Lu_2Si_2O_7$	3.8	unknown	
$Sc_2Si_2O_7 + Sc_2O_3$	5–6	1860[b]	Topcoat
$Yb_2Si_2O_7$	4–6	1850	
Yb_2O_3	6.8–8.4	2415[c]	
BSAS (monoclinic)	4–5	1300	
BSAS (hexagonal)	7–8	1300	
Mullite	5–6	1800	Intermediate coat
Alumina	6.0–8.4	2072	
Si	3.5–4.5	1400	Bond coat
SiC, SiC/SiC	4.5–5.5	2545	Substrate
Si_3N_4	3–4	1875	

[a] more recent value reported.
[b] Lower-melting eutectic at 1770 °C on Sc_2O_3-rich side and 1660 °C on SiO_2-rich side.
[c] Undergoes pre-melt phase transformation at 2360 °C.

c. Phase stability and chemical stability:

In addition to previously mentioned requirements, it is also important for each layer of the multi-layered EBC system to have a stable phase during thermal cyclic conditions at elevated temperatures. This is because phase transformations can generate cracks, which may provide easy pathways for oxidants to reach the substrate and eventually cause premature failure of the entire EBC system [14]. Moreover, on the one hand, if the coefficients of thermal expansion (CTEs) of the different EBC layers are higher than that of the SiC/SiC-CMC substrate, the EBC can develop tensile biaxial residual stresses. On the other hand, if the CTEs of the coating layers are lower compared to the SiC substrate, the EBC layers can develop compressive biaxial residual stresses. The level of residual stresses in the different coating layers of a BSAS/mullite/Si EBC system applied on a SiC substrate are illustrated in

Figure 2-10 [34]. In this case, the celsian BSAS phase is under compressive residual stress, whereas the hexacelsian BSAS phase is under tensile residual stress.

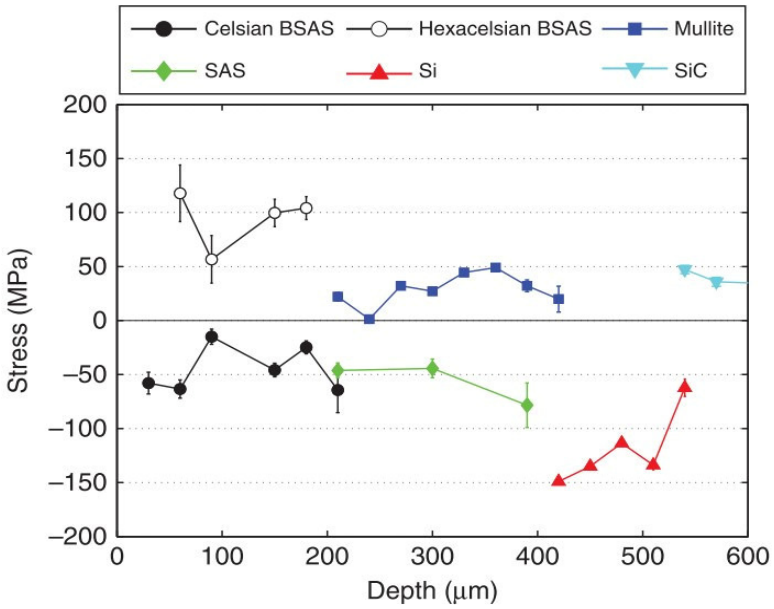

Figure 2-10: Biaxial residual stress versus coating depth for different materials of each layer (BSAS, mullite, Si, SiC) in multilayer BSAS/mullite/Si/SiC, EBC systems exposed to 1300 °C for 20 hours [35].

d. Water vapor stability:

Another important requirement is the coating durability in the presence of water vapour as determined by the amount of weight loss per unit area per unit time in the given environmental conditions. The weight loss with respect to the inverse of temperature for different materials like SiC, mullite, and BSAS is compared in Figure 2-11. The environmental conditions are identical for all three materials, including a water vapor partial pressure (P_{H2O}) of 0.5 atm, a total pressure (P_{total}) of 1 atm, and a gas velocity (v) of 4.4 cm/sec. It can be seen that the water vapor stability is in the descending order BSAS > Mullite > SiC.

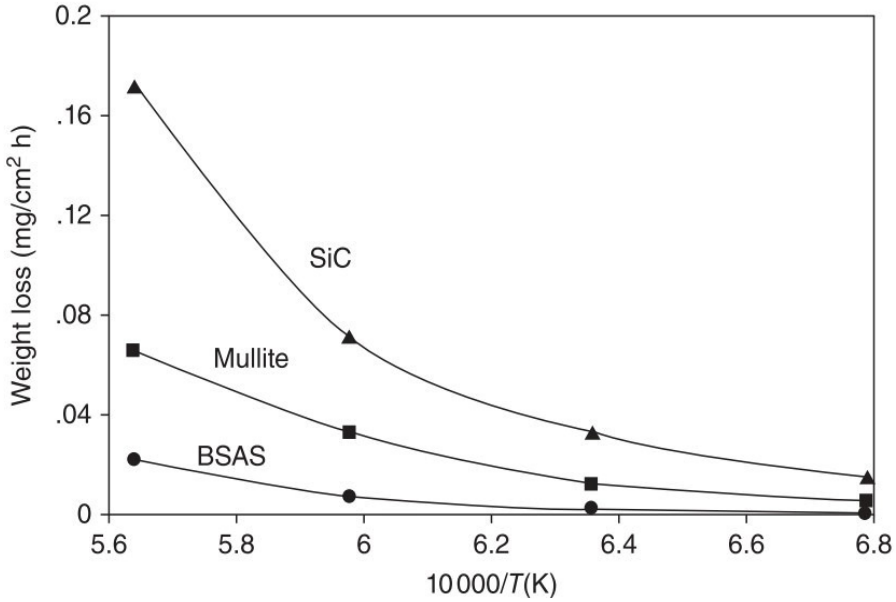

Figure 2-11: Water vapor stability of SiC, mullite and BSAS in an environment with P_{H2O} = 0.5 atm, P_{total} = 1 atm and v = 4.4 cm/sec [14].

2.1.4 Effect of water vapor on top coat materials

As previously discussed, rare earth silicates are good candidates for the EBC top coat application, especially in a combustion environment. The top coat is in direct contact with a highly demanding environment including (a) erosion by particles, (b) foreign / domestic object damage (FOD), and (c) calcium-magnesium-aluminum silicate (CMAS) deposition [36]. Also, the water vapor present in the aggressive combustion environment can deteriorate the top coat. For instance, high silica activity top coats tend to react with water vapor and undergo water vapor recession as shown in Equation (2.6) [37].

$$aMO_x.\,b\,SiO_2 + 2H_2O(g) = Si(OH)_4(g) + a.\,MO_x.\,(b-1)SiO_2 + \text{porosity} \quad (2.6)$$

This is the case of rare earth silicate top coats that are susceptible to water vapor recession. For instance, ytterbium disilicate ($Yb_2Si_2O_7$) reacts with water vapor to form a ytterbium monosilicate (Yb_2SiO_5) and a volatile silicon hydroxide as shown in Equation (2.7).

$$Yb_2Si_2O_7 + 2H_2O = Yb_2SiO_5 + Si(OH)_4(g) \quad (2.7)$$

Wang and Liu [38] investigated the water vapor recession behaviour of some rare earth disilicates by first-principle calculations (DFT). They observed that yttrium disilicate ($Y_2Si_2O_7$), thortveitite ($Sc_2Si_2O_7$), $Yb_2Si_2O_7$, and lutetium disilicate ($Lu_2Si_2O_7$) have similar crystal structure, in which the double-tetrahedral silica group (Si_2O_7) is linked with one RE element as shown in Figure 2-12. The silicon atoms share strong bonds with oxygen atoms. Therefore, it can be expected to show strong corrosion resistance in water vapor. Moreover, the type of rare earth element linked to the Si-O pair affects its bond strength, and consequently the water vapor recession level. The authors

observed a stronger Si-O bond strength when linked to Yb followed by the cases of linkage with Sc, Y, and Lu, leading to the descending order of resistance to water vapor recession: $Yb_2Si_2O_7 > Sc_2Si_2O_7 > Y_2Si_2O_7 > Lu_2Si_2O_7$. In addition, it was observed that the higher Si-O bond population leads to higher resistance to water vapor recession as seen in Table 2-2.

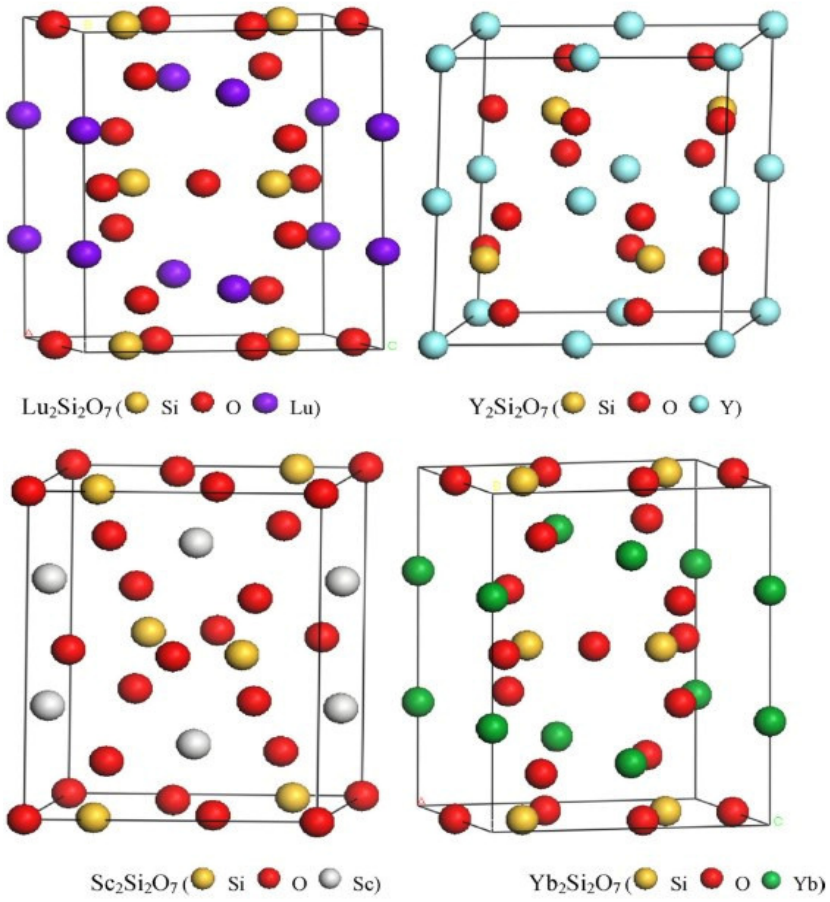

Figure 2-12: Crystal structures of four different rare earth silicates [38].

Table 2-2: Rare earth disilicates and their respective Si-O bond population [38].

Rare earth silicate	**Si-O bond population**
$Lu_2Si_2O_7$	0.5575

$Y_2Si_2O_7$	0.5938
$Sc_2Si_2O_7$	0.6000
$Yb_2Si_2O_7$	0.6125

As can be seen in Figure 2-13, EBC coatings substantially reduce the weight loss of ceramics such as Si_3N_4 substrates in comparison to the bare Si_3N_4 where silica is the only protective coatings [39].

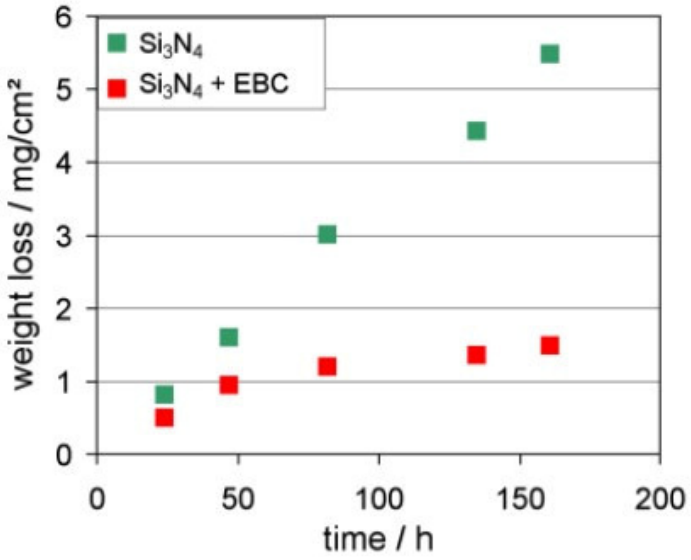

Figure 2-13: Comparing weight loss with time for a silica protective coating and EBC on a Si_3N_4 substrate [40].

2.1.5 Coating Deposition Process

The selection of the coating deposition process is based on the substrate complexity, the required coating durability, and the manufacturing costs [41]. The most prevalent coating deposition methods are: air plasma spray (APS); sputtering; electron-beam-assisted physical vapor deposition (EB-PVD); slurry deposition; sol-gel; chemical vapor deposition (CVD); and plasma spray assisted physical vapor deposition (PS-

PVD) [31]. It is observed that the coating properties change with different coating deposition processes. For instance, Table 2-3 compares the typical coating properties obtained using CVD and APS processes. Every coating deposition process has its own merits and demerits. However, APS is the most used technique for EBC coating deposition [42].

Table 2-3: Comparison of typical coating properties obtained using either CVD or APS [9].

Coating property	CVD	APS
Porosity	Dense	Porous
Cracks	None	Inherent
Adhesion	Superior (chemical bonding)	Moderate, requires addition bond coat
Composition	Easy to manipulate	Difficult to manipulate
Thickness	Thin	Thick
Crystallinity	Complete crystalline	Amorphous/crystalline
Manufacturability	Slow individual, but batch	Fast, but cannot batch
Uniformity	Not line of sight (uniform)	Line of sight (non-uniform)

2.2 Defect structures in top coat

Ceramic or oxide structures consist of both cations and anions. The concentration of cations and anions is such that the overall electroneutrality is maintained. The deviations from the long-range parent crystal structure are known as defect structure. The positively charged cations can move from a lattice point to an interstitial position, and the created interstitial ion ($M_i^{\bullet\bullet}$) - vacancy (V_M'') pair is known as Frenkel defect as shown in Figure 2-14 (a). There is no additional charge as the concentration of cations and anions remains constant. Another defect scenario is when one cation and one anion are simultaneously removed, leaving behind a pair of vacancies (V_M'',$V_O^{\bullet\bullet}$). Such defects are known as Schottky defects as shown in Figure 2-14(b) [43].

Equilibrium Schottky and Frenkel defect reactions are described in Equations (2.8) and (2.9), respectively [43] [46]:

Schottky: $$nil \Leftrightarrow V_M'' + V_O^{\bullet\bullet} \quad (2.8)$$

Frenkel: $$M_M^X \Leftrightarrow M_i^{\bullet\bullet} + V_M'' \quad (2.9)$$

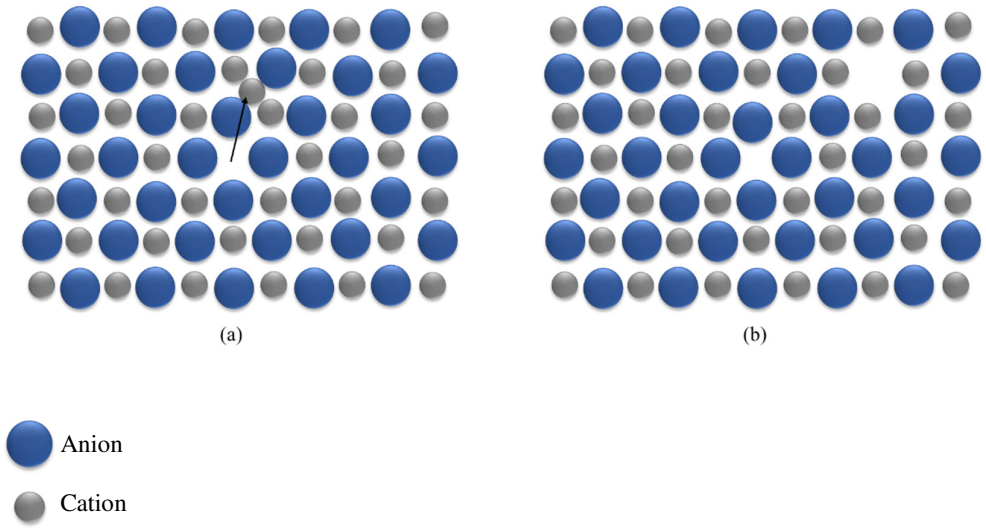

Figure 2-14: Ceramic defect structures: (a) Frenkel defect; and (b) Schottky defect.

Furthermore, the equilibrium concentration of defects in a crystal structure can be estimated using thermodynamic principles. The Gibbs free energy determines the defect formation feasibility with the three stability conditions designated as: $\Delta G = 0$ applies at equilibrium; $\Delta G > 0$ leads to instability; and $\Delta G < 0$ produces stable phase or crystal structure [45]. The negative Gibbs free energy at constant pressure and temperature can be written as [46]:

$$\Delta G = n(\Delta H - T\Delta S_{vibr}) - T\Delta S_c < 0 \quad (2.10)$$

Where ΔH represents the change in enthalpy; ΔS_{vibr} is a vibrational entropy; and ΔS_c is the configurational entropy. As shown in Figure 2-15, the enthalpy of formation is

directly proportional to the concentration of defects. At a fixed temperature, the configurational entropy (S_c) becomes more negative as the concentration of defects and the degree of randomness increases, thus ΔG becomes more negative. At equilibrium, the defect concentration corresponds to $n_{d,eq}$, and the ΔG has a minimum value [46].

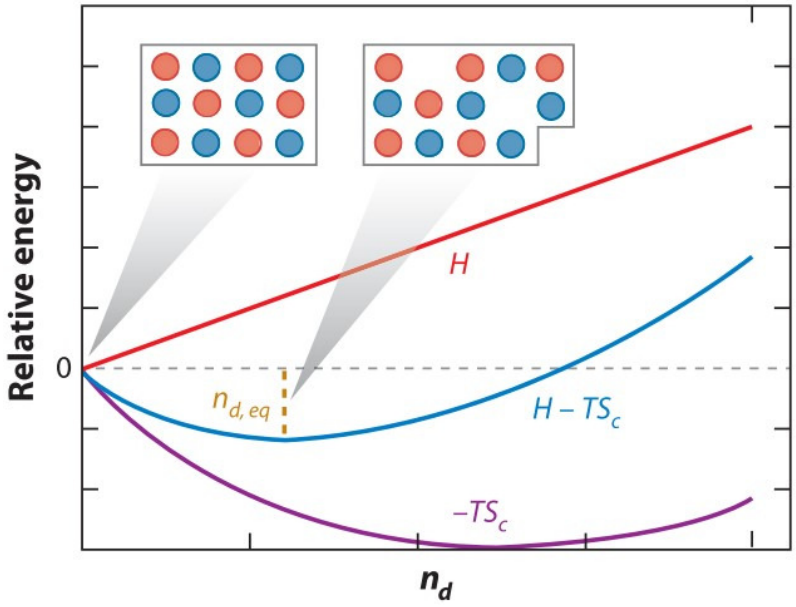

Figure 2-15: Change in enthalpy of formation (H), configurational entropy (S_c), and Gibbs free energy ($H\text{-}TS_c$) with respect to defect concentration (n_d) [46].

In addition, the following definitions can be made under the assumption that the total number of lattice sites is N, and n is the number of defect sites. The vibrational entropy change ΔS_{vibr} is defined as the difference between vibration frequency around defects and that in the undisturbed lattice, while the configurational entropy change ΔS_{config} is defined as the logarithm of the probability of defect to occupy the total available number of sites. The defect concentration is then given as [46]:

$$n_d \approx N \exp(\Delta S_{vibr}) \exp\left(-\frac{\Delta H}{kT}\right) \qquad (2.11)$$

Where k is the Boltzmann constant.

2.2.1 Effect of partial pressure on defect concentration

The interaction of the gas with the solid at the surface is such that ionic defects generate in the solid, including Frenkel defects, Schottky defects, or electronic carriers (electron-hole pairs). The generic defect reaction at equilibrium can be written as [46]:

$$M_M^X + O_O^X \Leftrightarrow M_{M,S}^X + O_{O,S}^X + V_M'' + V_O^{\bullet\bullet} \tag{2.12}$$

Where *M* and *O* on the left-hand side of the equation are the cations and the anions, respectively. The subscripts and the superscripts indicate the lattice positions and the charges of each ion or vacancy. Thus *M* and *O* ions are located at their lattice respective sites with neutral charges. Likewise, on the right-hand side, the subscripts *M*, *S* indicate that M ions have moved to surface sites, leaving behind a negatively charged vacancy denoted as V_M''. Similarly, the subscripts *O*, *S* indicate that *O* ions have moved to surface sites, generating a positively charged vacancy denoted as $V_O^{\bullet\bullet}$ [46].

The change in solid composition due to the interaction with the gas (X_2) phase can take place by either oxidation or reduction reactions. In the oxidation reaction, a cation vacancy (V_M'') along with a hole ($2h^{\bullet}$), and a neutral anion at a lattice site (X_X) form according to [44]:

$$\frac{1}{2}X_2(g) \leftrightharpoons X_X + V_M'' + 2h^{\bullet} \tag{2.13}$$

Where the oxidation equilibrium constant $K_{oxidation}$ is calculated as:

$$K_{oxidation} = [V_M''][h^{\bullet}]^2 P_{X_2}^{-1/2} \tag{2.14}$$

Where P_{X_2} is the partial pressure of the gas phase.

In the reduction reaction, positively charged anion vacancies ($V_X^{\bullet\bullet}$) generate together with an electron pair ($2e'$) to maintain electroneutrality. The defect reaction is written as [47]:

$$X_X \leftrightharpoons \frac{1}{2}X_2(g) + V_X^{\bullet\bullet} + 2e' \tag{2.15}$$

The reduction equilibrium constant $K_{reduction}$ is:

$$K_{reduction} = [V_X^{\bullet\bullet}]\,[e']^2 P_{X_2}^{1/2} \tag{2.16}$$

The electronic conductivity is affected by multiple factors including chemical composition, type of defects, and their respective concentrations, the partial pressure of the gaseous phase in the environment, and solid temperature. Moreover, the dominant defect reaction type depends on the oxygen partial pressure as shown in the Brouwer diagram in Figure 2-16. The diagram is also known as Kröger-Vink diagram and graphically illustrates the dominant defect structure as a function of partial pressure [44]. The oxide structure can be doped with two dopant types: an acceptor, and a donor cation, where the doped cation replaces the parent cation. The corresponding charge in each case relies on the type of dopant added. If the doped cation has a charge lower than the parent cation, it is called an acceptor cation that induces an overall negative charge. In contrast, a dopant with a higher charge than the parent cation is called donor cation which results in a positively charged oxide system. For a cation with the same charge as the parent cation, the overall system retains charge neutrality.

In general, the overall electroneutrality is maintained. This means, the total negatively charged defects (left side of the reaction) are equal to the total positively charged

defects (right side of the reaction). The defect reaction for the electroneutrality equation at equilibrium for acceptor dopants is given as:

$$[A'_M] + 2[O''_i] + n = [D^{\bullet}_M] + 2[V^{\bullet\bullet}_O] + p \qquad (2.17)$$

Where A'_M is the negatively charged acceptor dopant at cation (M) lattice sites; O''_i is the negatively charged oxygen ion residing at interstitial positions; and n is the negatively charged electronic charge (electrons). The positively charged $D^{\bullet}_M$ is the donor dopant; $V^{\bullet\bullet}_O$ is the positively charged oxygen vacancy; and p is the positively charged electronic charge (holes).

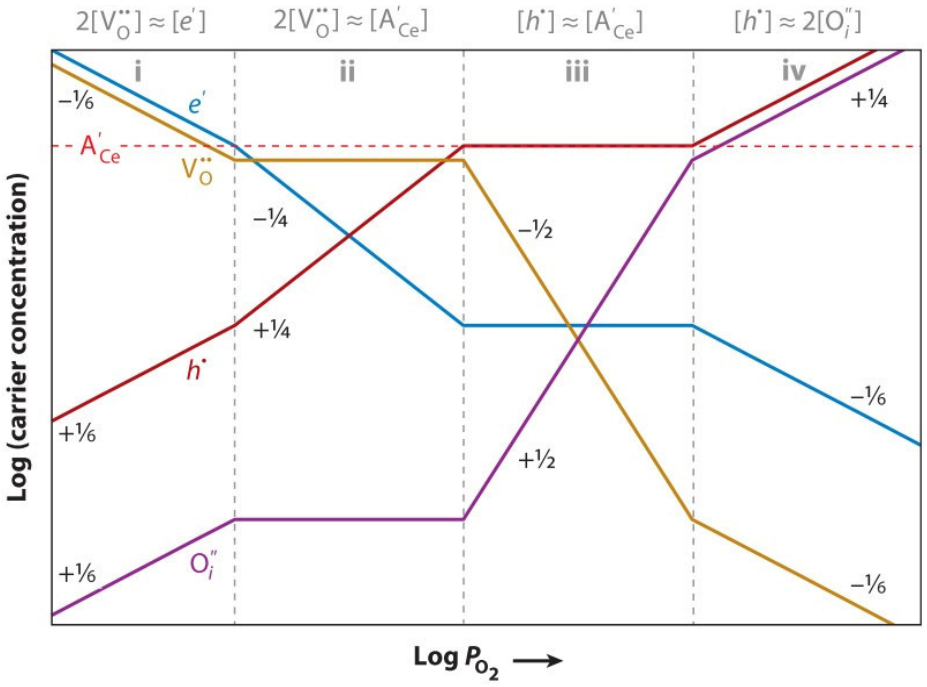

Figure 2-16: Isothermal Brouwer diagram illustrating the defect concentrations versus the oxygen partial pressure. Here ceria is doped with an acceptor ion [46].

The diagram has four regions differentiated based on the different defect pairs, which are considered for calculation using the electroneutrality Equation (2.17). The logarithm of the defect concentration is proportional to the oxygen partial pressure. For

example, $[V_O^{\bullet\bullet}] \propto P_{O_2}^m$, with *m* being the slope for the corresponding defect reaction as depicted in Figure 2-16. In the lowest oxygen partial pressure region (i) where $2[V_O^{\bullet\bullet}] \approx [e']$, the concentrations of oxygen vacancies and electrons are higher compared to the concentrations of oxygen ions (at the interstitial site) and holes (electronic carrier). For the oxygen partial pressure region (ii) with $2[V_O^{\bullet\bullet}] \approx [A'_{Ce}]$, the major defect pair is oxygen vacancies and acceptor dopant (with a negative charge). In region (iii) with $[h^{\bullet}] \approx [A'_{Ce}]$, the negatively charged dopants are compensated by positively charged electronic carriers (hole). Finally, in the highest oxygen partial pressure region (iv) with $[h^{\bullet}] \approx 2\,[O_i'']$, the concentration of oxygen ions at interstitial sites is equal to the concentration of positively charged electron carriers [46].

2.2.2 Effect of water vapor on defect concentration

In wet environments, additional oxygen partial pressure is created by the water vapor dissociation reaction as:

$$\mathrm{H_2O\ (g) = H_2(g) + 1/2\ O_2(g)} \qquad (2.18)$$

The dissociation of water vapor is driven by the Gibbs free energy minimization according to Equation (2.19) [48] .

$$\Delta G^o = -230000 - 8.14\ln(T) + 9.25T \qquad (2.19)$$

The formation of water vapor in the combustion environment is inevitable. In this study, a SiC/SiC-CMC substrate coated with an EBC system is studied up to a temperature of around 1316 °C or 1589 K. The standard Gibbs free energy estimated according to Equation (2.19) is negative with a value of -215.34 kJ/mol, indicating that water vapor dissociation takes place. The dissociation reaction produces hydrogen along with oxygen. Hydrogen tends to dissolve in oxides as protons with positive charges that

occupy interstitial sites. The most common Kröger-Vink notation for protons is $H_i^{\cdot}$. The proton dissolution equation can be written as [49] [50]:

$$H_2(g) + 2O_O^X = 2OH_O^{\bullet} + 2e' \qquad (2.20)$$

Also, protons are more stable around oxygen ions because they sit within a negatively charged electron cloud. Therefore, they can be termed as hydroxide ions with a positive charge and are denoted as $OH_O^{\bullet}$.

2.3 Oxidation mechanism

The oxidation of metal and their alloys is possible in two ways: the oxidant (oxygen or water vapor) can diffuse inward from the gas/oxide interface through the existing metal oxide and react with metal atoms at the oxide/metal interface. Or the metal atoms can migrate outward through the oxide to react with the oxidant at the gas/oxygen interface [51], as displayed in Figure 2-17. In general, the chemical potential difference of ions and charge carriers at the gas/oxide and oxide/metal interfaces drives the ionic and electronic migration, from the higher to the lower chemical potential [52]. The growth of the metal oxide film over time is quantitatively described by Wagner's parabolic scaling theory [53]–[55].

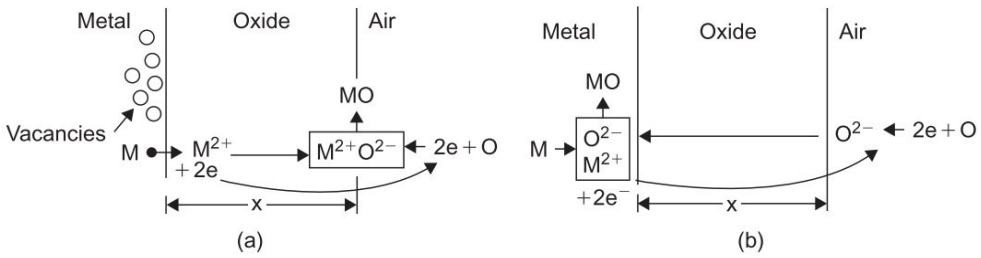

Figure 2-17: Illustration of metal oxidation mechanisms: (a) at the gas/oxide interface; and (b) at the oxide/metal interface [53].

In 1933, Wagner [54] proposed the oxide scale growth model, wherein the scale growth rate is assumed to be dependent on the diffusion of ions (cations or anions) or free carriers (electrons as negative charge carriers or holes as positive charge carriers). The ions and free carriers diffuse independently. In this approach, the diffusion of ions and free charge carriers through the metal oxide scale is assumed to be the rate-controlling mechanism, resulting in a parabolic growth rate of the oxide scale. The complete oxidation process involves the reduction of oxidants at the gas/oxide interface and the oxidation of the metal at the oxide/metal interface. Wagner's model emphasizes local equilibrium, which means the reactions at the gas/oxide and oxide/metal interfaces are at equilibrium, or the reaction at the interfaces is faster in comparison to the diffusion through the oxide. The mass transfer in metal oxides is by metal or oxygen vacancies as point defects. The resulting metal oxide growth rate equation in term of the number of equivalents (dñ) per unit area (A) per unit time (dt) is:

$$\frac{d\tilde{n}}{Adt} = \frac{1}{\xi}\left\{\frac{\tilde{c}}{2}\int_{P^{i}_{X_2}}^{P^{o}_{X_2}}\left[\left(\frac{z_M}{|z_X|}\right)D_M + D_X\right]d\ \ln P_{X_2}\right\} = \frac{\tilde{k}}{\xi} \qquad (2.21)$$

Where ξ is the instantaneous scale thickness; $\tilde{c}$ is the number of equivalents per cubic centimetre; D_M and D_x are cation and anion self-diffusion coefficients, respectively; $P^{i}_{X_2}$ is the oxidant partial pressure at the oxide/metal interface; $P^{o}_{X_2}$ is the oxidant partial pressure at the gas/oxide interface; Z_M and Z_X are the cation and anion, respectively.

2.3.1 Mass transfer in top coat (TC)

Kitaoka et al. [56] studied the mass transfer in an undoped α-Al_2O_3 wafer subjected to a steep oxygen partial pressure gradient at high temperatures (1973 K). The overall alumina formation was found to be controlled by the oxygen permeability constant,

determined by the inward movement of oxygen ions and outward movement of the aluminum ions. Wada et al.(2011) [57] further studied the anionic and cationic mass transfers via vacancies across the alumina wafer. Wada et al.(2017) [58] also studied the mass transfer in polycrystalline ytterbium disilicate (YbDS) at high temperature (1673 K) under identical oxygen partial pressure gradient as for α-Al_2O_3. The mass transfer mechanism in both alumina and ytterbium disilicate seemed to be identical. Therefore, the oxygen permeability constant expression used to describe mass transfer can also be considered identical for both YbDS and α-Al_2O_3.

The mass transport process in YbDS can be explained by the defect model [59]. The mass transport is by oxygen and ytterbium vacancy migration. The formation of vacancies is controlled by the oxygen partial pressure at the gas /YbDS interface, while the vacancy movement is controlled by the partial pressure gradient. Two cases can be distinguished depending on partial pressure level:

In the first case with low oxygen partial pressure, for instance, Po_2(hi) = 1Pa and Po_2(lo) = 10^{-9}Pa, the mass transport process takes place in the following steps:

i. Oxygen gas adsorbed at gas/YbDS interface, which is the surface with Po_2(hi).
ii. Oxygen vacancies form at YbDS/oxide (TGO) interface with Po_2(lo).
iii. The flux of positive oxygen vacancies ($V\ddot{o}$), along with negatively charged electron ($e^{\cdot}$), migrate from the Po_2(lo) surface to the Po_2(hi) surface.
iv. The adsorbed oxygen ($O_2(g)$) occupies vacant sites (O_0^x) as shown by the following defect reaction:

$$^1/_2\, O_2(g) + V\ddot{o} + 2e' = O_o^x \qquad (2.22)$$

In the second case with high oxygen partial pressure, for instance, with Po_2(hi) =10^5Pa and Po_2(lo) = 1Pa, the transport process proceeds in the following steps:

i. The Yb^{3+} (cation) diffuses from the surface with the low oxygen partial pressure Po_2 (lo) at the YbDS (TC)/oxide (TGO) interface to the gas/YbDS interface with the high oxygen partial pressure Po_2(hi).

ii. The oxygen gas (O_2) adsorbed at the gas/YbDS interface occupies oxygen lattice positions.

iii. The formed negative metal vacancies (V_{Yb}'''), accompanied with positively charged holes ($2h^{\bullet}$), migrate from the surface at Po_2(hi) to the surface at Po_2(lo).

iv. The metal vacancies annihilate by the reverse of the defect equation below at the YbDS/TGO interface, followed by the ejection of oxygen gas.

$$^1/_2\, O_2(g) = O_o^x + {}^2/_3\, V_{Yb}''' + 2h^{\bullet} \qquad (2.23)$$

The charge neutrality within the YbDS is maintained by keeping the concentration of electrons equal to that of oxygen vacancies or holes. Similarly, the concentration of holes is equal to that of metal vacancies. The total mass transfer in the YbDS wafer was determined as the sum of oxide and ytterbium ion migration driven by the chemical potential gradient, independent of the diffusion of cations (ytterbium ion) and anions (oxygen ion) taking place in opposite directions.

The dependence of vacancy concentration on oxygen partial pressure is given as [55]:

$$[V_O^{\bullet\bullet}] = \left(4K_{V_O^{\bullet\bullet}}\right)^{-1/3}.P_{02}^{-1/6} \qquad (2.24)$$

$$[V_{Yb}'''] = \left(4K_{V_{Yb}'''}\right)^{3/8}.P_{02}^{3/16} \qquad (2.25)$$

Diffusion experiments conducted at 1400°C with varying oxygen partial pressure differences ΔP_{O_2} of 10^{-9}Pa/1Pa, 10^{-5}Pa/1Pa; 10^{4}Pa/1Pa, 10^{5}Pa/1Pa showed that the dominant migrating species depend on ΔP_{O_2} across the wafer. Under low oxygen partial pressure conditions (10^{-9}Pa/1Pa), oxygen ions were found to migrate preferentially, and the exponent *n* was -1/6 as shown in Equation (2.24). On the other hand, for high oxygen partial pressure conditions (10^{5}Pa/1Pa), ytterbium ions permeation dominated, and the exponent n was 3/16 as per Equation (2.25).

2.3.2 Mass Transfer in TGO

In combustion environments, oxidants like H_2O and O_2 diffuse through the top coat and react with the silicon bond coat [60] to form silicon dioxide (SiO_2) at the TC/BC interface [61].

Figure 2-18 illustrates the steps in TGO formation assuming the silicon oxidation, and therefore, the TGO formation takes place at the TGO/BC interface, which means oxygen diffusing across the entire thicknesses of both the top coat and the TGO.

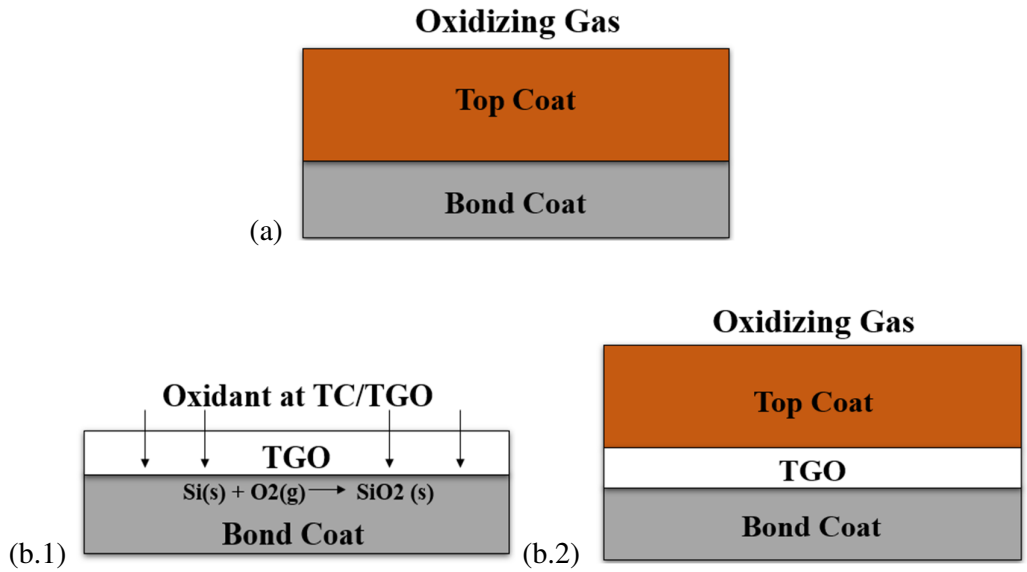

Figure 2-18: Steps of the TGO formation at BC/TGO interface; (a) at time *t*=0, TGO thickness h=0; (b.1) and (b.2) at the time *t*=*t*, TGO thickness h=h, the bond coat reacts with oxygen to form the silica TGO.

2.3.2.1 Oxidation of Silicon

The rate of oxidation of silicon can be quantified in terms of TGO thickness as a function of time (h^2/t). Another method to measure the oxidation kinetics is the weight change of specimens exposed to the oxidizing gaseous environment ($(\Delta wt)^2/t$) [62]. Generally, the oxidation of pure metals follows either the linear oxidation law, the parabolic oxidation law, or the logarithmic oxidation law. The linear oxidation law defines that the rate of the oxide thickness growth is directly proportional to the exposure time, whereby the rate-controlling step is predominantly reactions at the gas/oxide interface. The parabolic oxidation law defines that the square of the oxide scale thickness is directly proportional to the exposure time. In this case, the oxidant diffusion through the oxide scale is the rate-controlling step. The logarithmic oxidation law is not observed for the oxidation of silicon [63] and is generally observed in very thin films. All three types of oxidation behavior are illustrated in Figure 2-19.

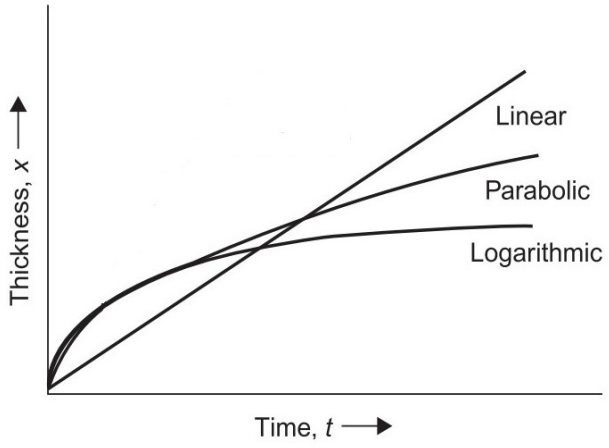

Figure 2-19: Three oxidation laws for the oxidation of pure metals [53].

The equation for the parabolic oxidation is given below:

$$h^2 = k_p t \tag{2.26}$$

Where h is the oxide thickness; k_p is the parabolic rate constant; and t is the exposure time. As the parabolic oxidation is diffusion controlled, the process is thermally activated and the minimum energy required to diffuse across the oxide is called the activation energy Q_a as per the following expression [55]:

$$k_p = k_o \exp\left[-\frac{Q_a}{RT}\right] \tag{2.27}$$

Here, k_o is the pre-exponential factor; R is the universal gas constant; and T is the absolute temperature.

The equation for the linear oxidation law is [29]:

$$h = k_l t \tag{2.28}$$

With h and t being the oxide thickness and the exposure time as defined earlier for the parabolic oxidation law; and k_l is the linear rate constant.

The oxidation of SiC leads to the formation of a silicon dioxide scale and carbonaceous by-products including CO, CO_2, and C as illustrated in Figure 2-20 [64] [65]. The oxidation kinetics involves simultaneous inward diffusion of oxidants such as O_2, O^{-2}, O, and outward diffusion of carbonaceous by-products.

With reference to Figure 2-20, C_1^* is the equilibrium concentration of oxidants at the gas/SiO_2 interface; and C_2^* is the equilibrium concentration of carbonaceous by-products at the SiO_2/SiC interface. At the outer gas/SiO_2 interface, C_{10} is the concentration of oxidants; and C_{21} is the concentration of the carbonaceous by-products. At the inner SiO_2/SiC interface, C_{11} is the concentration of oxidants; and C_{20}

is the concentration of the carbonaceous by-products [65]. Two possible rate-controlling steps are illustrated in Figure 2-20. If the inward diffusion of oxidants is the slower step, the concentration of carbonaceous by-products at both inner and outer surfaces of silicon dioxide is identical as shown in Figure 2-20 (a). However, if the outward diffusion of carbonaceous by-products is the slower step, the concentration of oxidants at either side of silicon dioxide is equal as shown in Figure 2-20(b) [65].

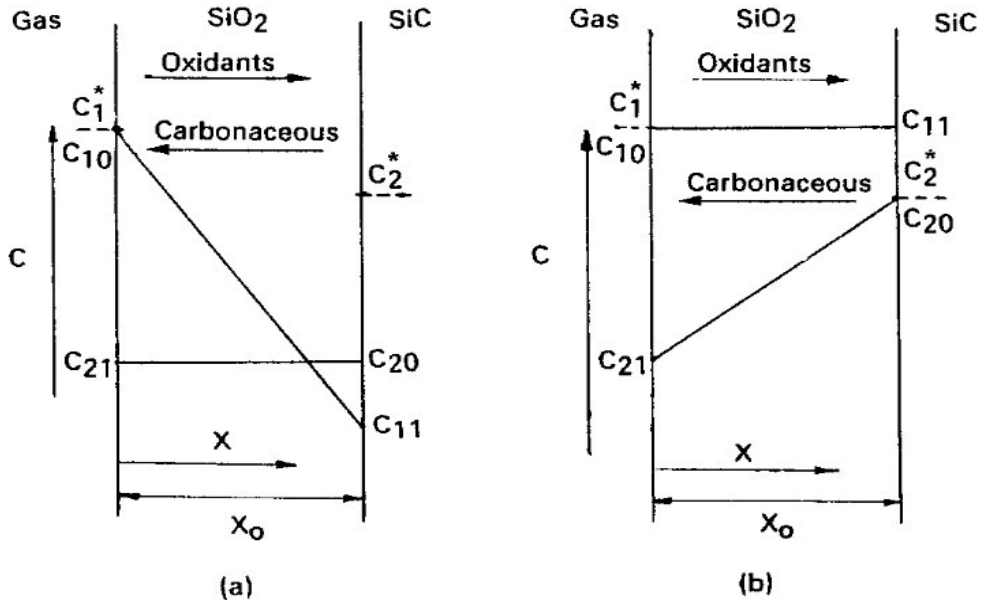

Figure 2-20: Oxidation of SiC with simultaneous inward diffusion of oxidants and outward diffusion of carbonaceous by-products: (a) oxidants diffuse at slower rates; (b) carbonaceous by-product diffuse at slower rates [65].

2.3.2.2 TGO growth kinetics

The prominent materials for the EBC top coat are mullite, yttria-stabilized zirconium (YSZ), barium-strontium aluminosilicate, and $RE_2Si_2O_7$ [66]. Oxygen (O_2) is the main oxidant for dry oxygen conditions, whereas, water vapor (H_2O) is the main oxidant for wet oxygen conditions [19]. In both conditions, diffusion of either molecular oxygen or atomic/ionic oxygen takes place, and a thermally grown oxide (TGO) layer forms.

Figure 2-21 shows the oxidant diffusion mechanism through TC and TGO (i.e., SiO_2) for a CMC substrate with Si as the bond coat.

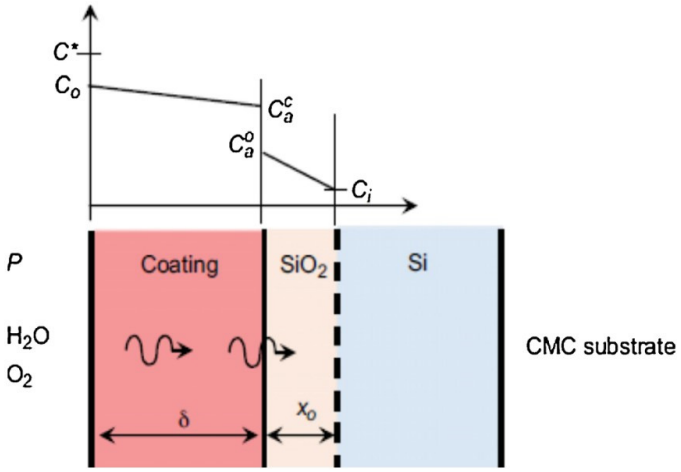

Figure 2-21: Growth of silicon dioxide (TGO) at top coat-Si (bond coat) interface [67].

In Figure 2-21, *P* is the partial pressure of the gaseous oxidant in the environment; C^* is the concentration of the oxidant at equilibrium; C_o is the oxidant concentration at the gas/top coat (TC) interface; C_a^o is the oxidant concentration in top coat at TC/TGO interface; C_a^c is the oxidant concentration in the TGO at the TC/TGO interface; C_i is the oxidant concentration at the TGO/bond coat interface; δ is the top coat thickness; and x_o is the TGO thickness.

In this context, Lu and Wang [66] studied the TGO formation and growth kinetics for $Yb_2Si_2O_7$ based EBC coating materials in different corrosive environments. They concluded that oxygen ions are dominant oxidants in conditions where the partial pressure of water vapor (H_2O) is up to 0.5 atm, while H_2O is the dominant oxidant at H_2O partial pressures near 1 atm.

2.4 EBC modes of failure

The possible modes of failure of EBC systems were illustrated by Lee [36] and can include the deposition of calcium-magnesium-alumina-silicate (CMAS); the erosion of the top coat; foreign object damage (FOD); and the water vapor recession. For the purpose of this research, however, diffusion and TGO formation leading to eventual failure of the EBC system is the focus. As such, the presence of oxygen and water vapor are studied as the main factors. Specifically, as the bond coat reacts with oxidants, the TGO grows, increasing its thickness and creating growth stresses at the interface. When the TGO reaches a critical thickness, the accumulated growth stresses become greater than the interface bond strength. This leads to crack formation and propagation at the TGO/bond coat interface, and eventually to the spallation of the EBC system, limiting its lifetime. A schematic illustration of oxidant flow, TGO formation, and EBC system failure is shown in Figure 2-22.

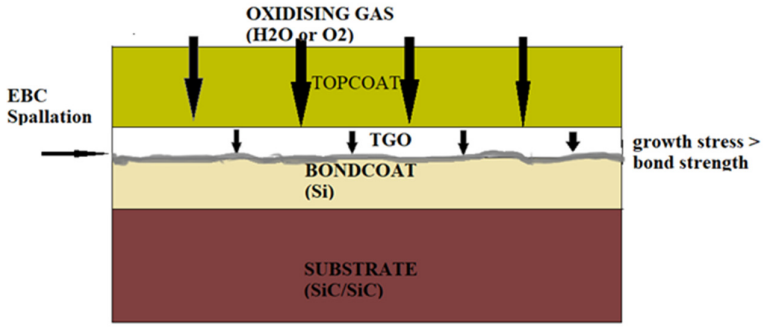

Figure 2-22: Schematic illustration of oxidant flux, TGO formation, and failure of the EBCs.

In practice, it is difficult to avoid the TGO formation, but it is a logical and standard approach to retard or control its growth in order to delay EBC spallation. Indeed, Klemm et al. [17] successfully delayed the TGO formation by restricting the diffusion flux of oxidants. Their EBC system consisted of a YbDS top coat, a YbDS+SiC

intermediate layer, and a Si bond coat on a SiC/SiC-CMC substrate. The SiC particles in the YbDS layer preferentially oxidized, restricting oxidants from reaching and reacting at the critical bond coat interface. In this case, the SiC particles acted as getters to hinder the oxidant permeation through the top coat, thereby reducing the rate of TGO growth.

Also, Lee [36] proposed to control the TGO growth through chemical modifications of the EBC system. Refractory oxides such as alumina, mullite, YAG (yttrium aluminum garnet), TiO_2(titania), referred to as modifiers, were added to the YbDS top coat. Although the modifiers effectively improved the lifetime of the coatings compared to the unmodified top coat, each of them had its own characteristic effect on the TGO growth rate.

2.5 Oxygen permeability

The permeability of the oxygen through top coat and the TGO determines their ability to protect the substrate material from being oxidized, eventually causing EBC system failure [68]. In general terms, permeability is defined as the amount of gas permeated per unit area per unit time. The mathematical expression used for oxygen permeability is the same as for the flux. At steady-state, when temperature and oxygen partial pressure is constant at both surfaces [69] [70], Fick's first law applies and is written as:

$$\mathrm{J} = \mathrm{P} = -\mathrm{D}\frac{\mathrm{dC}}{\mathrm{dx}} \tag{2.29}$$

Where *J* is the oxygen flux equal to *P* that is the oxygen permeability in the direction of the coating thickness; $\frac{dC}{dx}$ is the concentration gradient across the thickness of the coatings; and *D* is the oxygen diffusion coefficient.

Ogura et al. [70] directly related the oxygen permeability to the oxygen defect concentration gradient, where the oxygen defect concentration at each surface of the coating is described in terms of oxygen partial pressure. Hereby, diffusion is considered under steady-state conditions as described in Equation (2.30).

$$P = -D\frac{k(P_2^n(O_2) - P_1^n(O_2))}{l} \tag{2.30}$$

Where k is the equilibrium constant; $P_1(O_2)$ and $P_2(O_2)$ are the oxygen partial pressure at either surface of the wafer; n is the exponent that depends on the oxygen defect reaction at each of the wafer surfaces exposed to oxygen; and l is the wafer thickness. In this consideration, the amount of soluble oxygen at the interface is directly proportional to P^n [69].

In most practical situations, diffusion is in a non-steady state. Therefore, the oxygen permeation or oxygen flux is time-dependent and the concentration gradient or oxygen partial pressure gradient changes with time. Non-steady state diffusion is expressed in Fick's second law, as shown below:

$$\frac{dc}{dt} = D(\frac{d^2c}{dx^2}) \tag{2.31}$$

2.5.1 Oxygen permeability constant

The oxygen permeability constant has been immensely studied to understand oxygen permeation through various ceramic oxides and high-temperature protective coatings like alumina, beryllia, yttria [69], and zirconia [70] under different oxygen partial pressure gradients. It is defined as the permeability multiplied by the thickness of the material *(P.l)*, as in Equation (2.32) below.

$$P.l = \frac{\text{molar equivalents of Oxygen}}{\text{sq. m} * \text{sec}} * \text{m} = \text{mol/m.sec} \qquad (2.32)$$

Courtright et al. [69] called it permeability normalized for unit thickness, which indicates the amount of oxygen permeating through a barrier with a fixed thickness (l).

2.5.2 Experimental oxygen permeability constant

An experimental method to measure the oxygen permeability constant is to study a wafer of a known oxide material in terms of oxygen permeation through a known sample thickness and a known permeation surface area. The experimental set-up is such that an oxygen partial pressure gradient is produced across the thickness of the wafer. Oxygen gas along with argon is introduced at a fixed gas flow rate in one chamber at one side of the wafer, and the permeated oxygen is swept with noble gas (argon) at the opposite side of the chamber. The permeated oxygen is measured using a zirconia oxygen sensor [57] [70]–[72]. The set-up is shown in Figure 2-23.

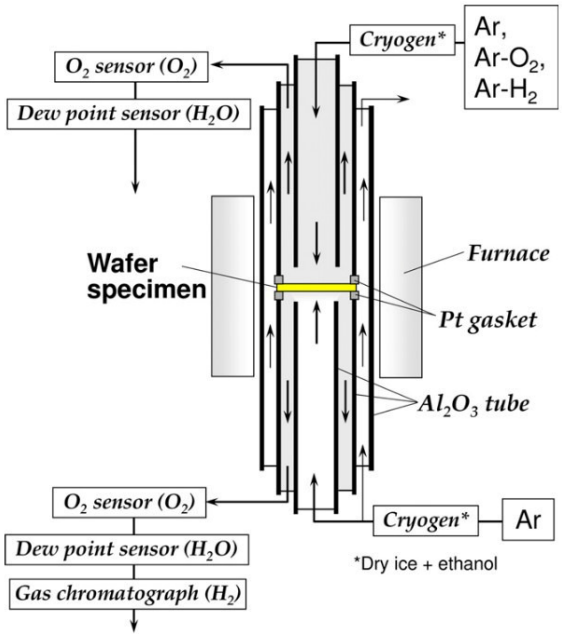

Figure 2-23: Experimental set-up for oxygen permeability measurement [71].

The mathematical expression for the calculation of the oxygen permeability using experimental parameters is given in Equation (2.33).

$$P.l = \frac{C_p.Q.l}{V_{st}.S} \tag{2.33}$$

The permeability (P) is defined as the product of the ratio of the permeated oxygen concentration (C_p) and the test gas flow rate (Q) per exposed wafer surface (S), per unit standard molar volume of an ideal gas (V_{st}). Multiplying the permeability by the wafer thickness (l) yields the oxygen permeability constant *(P.l)*.

2.5.3 Models for oxygen permeability constant

2.5.3.1 Oxygen permeability constant through top coat (YbDS)

Wada et al. [58] calculated the oxidant flux permeating through a ytterbium disilicate wafer of known thickness. The permeation was considered to be due to the oxygen ions and the ytterbium ions only, independently. The diffusion contribution of silicon ions to the total flux is assumed negligible as silicon shares a strong covalent bond with oxygen [71]. The total permeability of the oxidant is then calculated in terms of oxygen permeability constant as:

$$4P.l = \int_0^l J_{TO}\,dx \tag{2.34}$$

Where J_{TO} (mol/m^2 .sec) is the total permeability of oxidants across the wafer of thickness l (m), with $P.l$ as calculated earlier in Equation (2.33). All parameters in the equations are either known or can be experimentally acquired.

The total flux that permeates through the typical $Yb_2Si_2O_7$ top coat is given as the sum of ytterbium ion and oxygen ion mass transfer. Also, the authors expressed the total oxygen permeation through a polycrystalline wafer as:

$$4\,P.l = A_i(P_{O_2}(\mathrm{hi})^n - P_{O_2}(\mathrm{lo})^n) \tag{2.35}$$

Where A_i is a temperature dependent frequency factor; subscript i indicates ytterbium (Yb) or oxygen (O); n depends on the defect reaction; Po_2(hi) and Po_2(lo) are relative oxygen partial pressures in contact with opposite interfaces of the wafer.

They expressed the oxygen permeability constant as in Equation (2.36) [58]:

$$\begin{aligned} 4P.l = {} & A_{yb}(P_{O_2}(\mathrm{h}_i)^{\frac{3}{16}} - P_{O_2}(lo)^{\frac{3}{16}}) \\ & + A_o(P_{O_2}(\mathrm{h}_i)^{-\frac{1}{6}} - P_{O_2}(lo)^{-\frac{1}{6}}) \end{aligned} \tag{2.36}$$

2.5.3.2 Oxygen permeability through TGO (SiO2)

Deal and Grove [73] proposed a model that describes the oxidation of silicon in two stages: linear oxidation and parabolic oxidation. Three oxidant flux equations were considered: the flux equation for gas transport from the bulk of the surrounding environment to the gas/oxide interface; the flux equation for the oxidant diffusion across the oxide layer; and the flux equation for the reaction of the oxidant at the oxide/metal interface. The mass balance at the two surfaces of the oxide layer was assumed to be under steady-state conditions. They derived the general form of the linear-parabolic oxidation model as:

$$x_o^2 + A\,x_o = B\,(t + \tau) \tag{2.37}$$

Where x_o is the oxide thickness; B and A are parabolic and linear rate constants, respectively; t is the time; and τ is a constant that accounts for the initial oxide thickness at time $t = 0$.

Sullivan [67] reformulated the Deal-Grove linear-parabolic oxide growth equation to study the oxygen permeability through the EBC system. They focused mainly on the oxygen permeability through the TGO. They used experimental values for the TGO thickness with respect to time to fit the equation. The modified linear rate constant A for the top coat-TGO system was introduced by curve-fitting, while the parabolic rate constant B was considered independent of the top coat. They also considered different coatings as bond coat with the modified rate constant being linearly proportional to each coating thickness. This modified linear rate constant is the summation of simple linear constants stating the ratio of oxidant permeability in oxide to the oxidant permeability in the TGO layer.

3 Modelling Methodology

A comparative study of oxidant permeation through both top coat (TC) and thermally grown oxide (TGO) layers can provide information on the effect of each of the two layers on oxidation and damage of the EBC system. Moreover, the study of the relative oxygen permeability constant of TC and TGO in both dry oxygen and water vapour environments can allow to understand the impact of each of the two oxidants. Also, factors like time, temperature, gas partial pressure, and modifier addition affect the total oxygen permeability constant. In this chapter, the methodologies used to modify the oxygen permeability constant equations for the TC and to derive the oxygen permeability constant equation for the TGO are presented.

The oxygen permeability constant for the top coat (TC) in dry oxygen conditions is described in sub-section 2.5.3.1. Here, Equation (2.36) defined earlier in the Literature Review, is used to estimate the oxygen permeability constant using exponents 3/16 and -1/6, respectively. Moreover, the interaction of water vapor with the oxygen vacancy concentration and metal vacancy concentration is evaluated using defect equilibrium reactions. Here, the exponents used for the oxygen permeability constant in the Literature Review Equation (2.35) are designated as p and q for the oxygen vacancy concentration and the metal vacancy concentration, respectively.

The general overview of the parameters required to calculate the oxygen permeability constant in both top coat and TGO layers is depicted in the flowchart in Figure 3-1

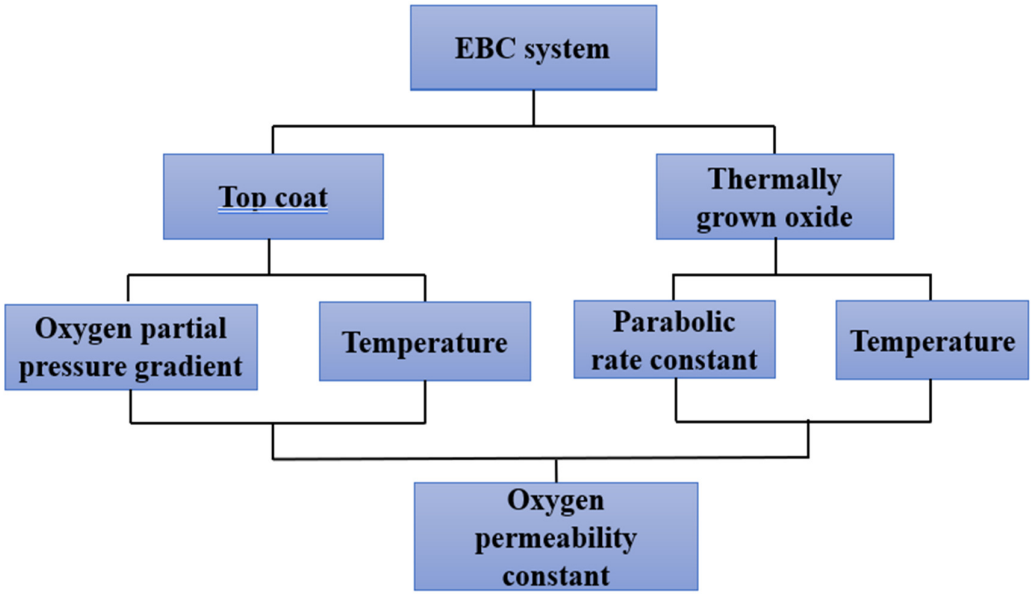

Figure 3-1: Flowchart of factors affecting the oxygen permeability constant for top coat and TGO layers.

3.1 Water vapor effect on oxygen permeability constant through top coat

The oxygen permeability constant, as initially described in Equation (2.36), strongly depends on the used exponents, which in turn depend on the prevailing defect reactions. In this study, four assumptions are made following the approach by Wada et al. [58] in an effort to describe the effect of water vapor on the defect concentration.

Assumption 1: The ytterbium disilicate unit cell consists of two types of cations (Yb^{3+}, Si^{4+}) and an oxide anion (O^{2-}). However, the metal vacancy formation is assumed to be solely due to Yb^{3+}ions, and that of anion vacancy due to O^{2-} ions.

Assumption 2: The dominant defects for the ytterbium disilicate are the Schottky defects. Therefore, interstitial defects are ignored. In general terms, the equation for charge neutrality is written as:

$$\text{nil} \leftrightharpoons V_M'' + V_O^{\bullet\bullet} \tag{2.8}$$

Where V_M'' are the metal vacancies located at metal lattice sites; and $V_O^{\bullet\bullet}$ are the oxygen vacancies at oxygen lattice sites.

Assumption 3: The volatilization of ytterbium disilicate in the presence of water vapor is ignored.

Assumption 4: The ytterbium disilicate is crystalline.

Table 3-1 below summarizes the Kröger-Vink notations used in this work.

Table 3-1: Kröger-Vink notations used in this work:

Symbol	Definition
$\boldsymbol{O_o^x}$	Neutrally charged oxygen at normal lattice sites
$\boldsymbol{V_o^{\bullet\bullet}}$	Positively charged oxygen vacancy at oxygen lattice sites
$\boldsymbol{V_M'''}$	Negatively charged metal vacancy at metal lattice sites.
$\boldsymbol{OH_o^{\bullet}}$	Positively charged proton at oxygen lattice sites
$\boldsymbol{h^{\bullet}}$	Positively charged hole
$\boldsymbol{e'}$	Negatively charged electron.

Subscripts symbolize the lattice location: as *o* and *M* indicate oxygen and metal lattice sites, respectively. Superscripts symbolize the charge on the defect as: ^{x} neutral or zero charges; $^{\bullet}$ (+1) positive charge; $^{\bullet\bullet}$ (+2) positive charges; $'$ (-1) negative charge; and $'''$ (-3) negative charge.

In wet oxygen conditions, water vapor is in direct contact with the top coat. The gaseous water molecule dissociation at the surface has a considerable effect on both the oxygen vacancy concentration and the ytterbium vacancy concentration. The assumed two

equations for water molecule dissociation can be described as in Equation (2.18) in the Literature Review (re-written below) and Equation (3.12), without proton (first case in sub-section 3.1.1) and with a proton (second case in sub-section 3.1.2), respectively.

3.1.1 First Case

One mole of gaseous water molecule dissociates into one mole of hydrogen gas (no protonic effect) and a half mole of oxygen gas as:

$$H_2O(g) \rightarrow H_2(g) + {}^1\!/_2\, O_2(g) \tag{2.18}$$

Four types of defects, with charges $[V_{yb}'''], [e'], 2[V_O^{\bullet\bullet}], [h^{\bullet}]$, are involved as illustrated in the equilibrium defect reaction Equations (3.2) and (3.7).

To maintain electroneutrality, the total negative charge should be equal to the total positive charge as:

$${}^2\!/_3\,[V_{yb}'''] + [e'] = 2[V_O^{\bullet\bullet}] + [h^{\bullet}] \tag{3.1}$$

3.1.1.1 Effect of water vapor partial pressure on the oxygen vacancy concentration

The oxidation reaction at the top coat interface exposed to gas (gas/top coat interface) is retrieved from the Literature Review Equation (2.22) as rewritten below:

$${}^1\!/_2\, O_2 + V_O^{\bullet\bullet} + 2e' \rightarrow O_O^x \tag{2.22}$$

Adding Equation (2.18) and Equation (2.22), we obtain

$$H_2O + V_O^{\bullet\bullet} + 2e' \rightarrow H_2(g) + O_0^x \tag{3.2}$$

And the equilibrium constant for Equation (3.2) can be written as:

$$k_{3.2} = \frac{[O_o^x].p_{H2}}{[V_O^{\bullet\bullet}][e']^2.p_{H2O}} \quad (3.3)$$

From Equation (3.2), it can be seen that only the defect pair $[e'], [Vö]$ takes part in the reaction, which means the contributions of other defects are neglected: $[V_{yb}'''] = [h^{\bullet}] = 0$.

Thus, Equation (3.1) can be reduced to

$$[e'] = 2[V_O^{\bullet\bullet}] \quad (3.4)$$

Substituting $[e'] = 2[Vö]$, and $[O_o^x] = 1$ in Equation (3.3) yields

$$k_{3.2} = \frac{1\,.\,p_{H2}}{[V_O^{\bullet\bullet}](2[V_O^{\bullet\bullet}])^2.\,p_{H2O}} \quad (3.5)$$

or

$$[V_O^{\bullet\bullet}] = \left(\frac{k_{3.2}\,p_{H2}}{4}\right)^{1/3}.p_{H2O}^{-1/3} \quad (3.6)$$

3.1.1.2 Effect of water vapor partial pressure on the metal vacancy concentration

The oxidation reaction at the gas/top coat interface can be described by revisiting Equation (2.23) given earlier in the Literature Review chapter:

$$^1/_2\,O_2(g) \rightarrow O_o^x + {}^2/_3\,V_{yb}''' + 2h^{\bullet} \quad (2.23)$$

Adding Equation (2.18) and Equation (2.23), the equation describing the water dissociation for metal vacancy formation can be written as

$$H_2O \rightarrow O_o^x + {}^2/_3\,V_{yb}''' + 2h^{\bullet} + H_2(g) \quad (3.7)$$

and the equilibrium constant is

$$k_{3.7}= \frac{\left[V_{yb}'''\right]^{2/3}\ [h^{\bullet}]^2[O_O^x].p_{H2}}{p_{H2O}} \tag{3.8}$$

The dominant defect pair in Equation (3.7) is $[V_{yb}'''], [h^{\bullet}]$. Therefore, the electroneutrality Equation (3.1) can be simplified to

$$^2/_3\,[V_{yb}'''] =[\,h^{\bullet}] \tag{3.9}$$

Substituting $^2/_3\,[V_{yb}'''] =[\,h^{\bullet}]$ and $[O_O^x] =1$ (the activity of the neutral oxygen at lattice site) in Equation (3.8) yields

$$k_{3.7}= \ ^4/_9 \frac{\left[V_{yb}'''\right]^{2/3}\ \left[V_{yb}'''\right]^2.1\,.\,p_{H2}}{p_{H2O}} \tag{3.10}$$

with

$$[V_{yb}'''] = \left(^4/_9 \frac{k_{3.7}}{p_{H2}}\right)^{3/8}.p_{H2O}^{3/8} \tag{3.11}$$

Considering Equations (3.6) and (3.11), it can be seen that the equilibrium constant is dependent on both the water vapor partial pressure and the hydrogen gas partial pressure. However, if the partial pressure of hydrogen is assumed to be constant, the oxygen vacancy concentration becomes proportional to $p_{H2O}^{-1/3}$, which means the ytterbium vacancy concentration is proportional to $p_{H2O}^{3/8}$.

3.1.2 Second Case

One mole of gaseous water molecules interacts with two oxygen atoms in the parent lattice to form a half mole of oxygen gas and two moles of protons as:

$$H_2O(g)+2O_O^x \rightarrow 2OH_O^{\bullet} + 2e' + {}^1/_2\,O_2(g) \tag{3.12}$$

The defects formed at equilibrium in this reaction are $[V_{yb}'''], [e'], 2[V_O^{\bullet\bullet}], [h^{\bullet}], [OH_O^{\bullet}]$ as described in Equations (3.14) and (3.19).

Again, to maintain electroneutrality, the total negative charge should be equal to the total positive charge. Therefore, Equation (3.1) can also be written as:

$$3[V_{yb}'''] + [e'] = 2[V_O^{\bullet\bullet}] + [h^{\bullet}] + [\,OH_O^{\bullet}] \tag{3.13}$$

Here, the proton defect ($[\,OH_O^{\bullet}]$) is an additional entity.

3.1.2.1 Effect of water vapor partial pressure on the oxygen vacancy concentration

The oxidation reaction at the gas/top coat interface can be retrieved from the Literature Review Equation (2.22):

$$^1/_2\, O_2 + V_O^{\bullet\bullet} + 2e' \rightarrow O_o^x \tag{2.22}$$

Adding Equation (3.12) and Equation (2.22), we obtain

$$H_2O(g) + V_O^{\bullet\bullet} + O_o^x \rightarrow 2OH_O^{\bullet} \tag{3.14}$$

and the equilibrium constant for Equation (3.14) is

$$k_{3.14} = \frac{[OH_O^{\bullet}]^2}{[O_O^x]\,[V_O^{\bullet\bullet}].p_{H2O}} \tag{3.15}$$

The dominant defect pair in Equation (3.13) is $[OH_O^{\bullet}]$, $[V_O^{\bullet\bullet}]$. Thus, the electroneutrality Equation can be reduced to

$$[OH_O^{\bullet}] = 2[V_O^{\bullet\bullet}] \tag{3.16}$$

Substituting $[OH_O^{\bullet}] = 2[V_O^{\bullet\bullet}]$ and $[O_O^x]$ =1 (activity of the neutral oxygen at lattice sites) in Equation (3.15), we obtain

$$k_{3.14} = \frac{4\,.\,[V_O^{\bullet\bullet}]^2}{[V_O^{\bullet\bullet}].\ p_{H2O}.1} \tag{3.17}$$

with

$$[V_O^{\bullet\bullet}] = \left(\frac{k_{3.14}}{4}\right)^1 . \ p_{H2O} \tag{3.18}$$

3.1.2.2 Effect of water vapor partial pressure on the metal vacancy concentration

The possible oxidation reaction at the gas/top coat interface is retrieved from the Literature Review Equation (2.23) as rewritten below:

$$^1/_2\, O_2(g) \rightarrow O_o^x + {}^2/_3\, V_{yb}''' + 2h^\bullet \tag{2.23}$$

Adding Equation (2.23) and Equation (3.12) yields

$$H_2O(g) + O_0^x \rightarrow 2OH_O^\bullet + 2e' + {}^2/_3\, V_{yb}''' + 2h^\bullet \tag{3.19}$$

and the equilibrium constant is

$$k_{3.19} = \frac{[OH_O^\bullet]^2 [V_{yb}''']^{2/3} [e']^2 \ [h^\bullet]^2}{[O_O^x] . p_{H2O}} \tag{3.20}$$

Equation (3.19) and the corresponding equilibrium constant $k_{3.19}$ indicate four defect concentrations. However, we can assume one defect pair as dominant and the other defect pair as negligible.

Firstly, we assume the dominant defect pair in Equation (3.13) is $[V_{yb}''']$, $[OH_O^\bullet]$.

In that case, the equilibrium constant $k_{3.19}$ can be written as

$$k'_{3.19} = \frac{[OH_O^\bullet]^2 [V_{yb}''']^{2/3}}{[O_O^x] . p_{H2O}} \tag{3.21}$$

Maintaining electroneutrality as per Equation (3.13) yields

$$3[V_{yb}'''] = [OH_O^\bullet] \tag{3.22}$$

Substituting $3[V'''_{yb}] = [OH^{\bullet}_{O}]$ and $[O^{x}_{o}]$ =1 (activity of the neutral oxygen at lattice sites) yields

$$k'_{3.19} = \frac{9\left[V'''_{yb}\right]^{2/3}\left[V'''_{yb}\right]^{2}\cdot 1}{p_{H2O}} \tag{3.23}$$

with

$$[V'''_{yb}] = \left(\frac{k'_{3.19}}{9}\right)^{3/8}\cdot p^{3/8}_{H2O} \tag{3.24}$$

Secondly, we assume the dominant defect pair in Equation (3.13) is $[e']$, $[OH^{\bullet}_{O}]$. In that case, the equilibrium constant $k_{3.19}$ can be written as

$$k''_{3.19} = \frac{[OH^{\bullet}_{O}]^2[e']^2}{[O^{x}_{o}]\cdot p_{H2O}} \tag{3.25}$$

Again, maintaining electroneutrality according to Equation (3.13) yields

$$[e'] = [OH^{\bullet}_{O}] \tag{3.26}$$

And Equation (3.25) reduces to

$$k''_{3.19} = \frac{[OH^{\bullet}_{O}]^4}{p_{H2O}} \tag{3.27}$$

Meaning:

$$[OH^{\bullet}_{O}] = (k''_{3.19})^{1/4}\cdot p^{1/4}_{H2O} \tag{3.28}$$

Thirdly, we assume the dominant defect pair in Equation (3.13) is $[V'''_{yb}]$, $[h^{\bullet}]$. In that case, $k_{3.19}$ can be written as

$$k'''_{3.19} = \frac{[h^{\bullet}]^2\left[V'''_{yb}\right]^{2/3}}{[O^{x}_{o}]\cdot p_{H2O}} \tag{3.29}$$

And maintaining electroneutrality requires

$$3[V'''_{yb}] = [h^{\bullet}] \tag{3.30}$$

Substituting $3[V'''_{yb}] = [h^{\bullet}]$ and $[O_o^x]$ =1 (activity of the neutral oxygen at lattice sites) in Equation (3.13) yields

$$k'''_{3.19} = \frac{9\left[V'''_{yb}\right]^{2/3}\left[V'''_{yb}\right]^{2}.1}{p_{H2O}} \tag{3.31}$$

with

$$[V'''_{yb}] = \left(\frac{k'''_{3.19}}{9}\right)^{3/8} . p_{H2O}^{3/8} \tag{3.32}$$

In summary, Equation (3.17) suggests that the oxygen vacancy concentration is directly proportional to the water vapor partial pressure (p_{H2O}). Equations (3.24) and (3.32) indicate that the metal vacancy concentration depends parabolically on the water vapor partial pressure, with the exponent being 3/8, meaning a linearly proportional relationship to $p_{H2O}^{3/8}$. Moreover, the defect reaction Equation (3.28) shows that the proton concentration depends parabolically on the water vapor partial pressure with an exponent of 1/4. However, this can be ignored in our particular case as the oxygen permeability constant equation for the top coat is only related to the metal vacancy concentration and the oxygen vacancy concentration.

3.2 Oxygen permeability constant equation for TGO

The rate of growth of silicon dioxide or silica TGO on the bond coat is directly proportional to the diffusivity of the oxidizing species, to the oxygen partial pressure gradient across the TGO thickness ($\frac{dp}{dh}$), and to the molar volume of silica (V_{SiO_2}), as described in Equation (3.33). Moreover, the TGO growth rate is inversely proportional

to the number of moles (m) of the diffusing species reacting with 1 mole of silicon to form 1 mole of Silicon dioxide.

$$\frac{dh}{dt} = -\frac{V_{SiO_2}}{m} \cdot D \cdot \frac{dp}{dh} \tag{3.33}$$

The negative sign in Equation (3.33) indicates that diffusion occurs from the high oxygen partial pressure at the TC/TGO interface to the low oxygen partial pressure at the TGO/BC interface.

The oxygen permeability constant for TGO is estimated using Fick's first law of diffusion as described in Equation (3.34) assuming stationary diffusion.

$$-D \cdot \frac{dp}{dh} = J \tag{3.34}$$

Where J is the oxidant flux through the TGO.

For simplicity, we assume O_2 be the only diffusing specie. Therefore, Equation (3.33) can be rewritten as

$$\frac{dh}{dt} = \frac{V_{SiO_2}}{m} \cdot J_{O_2} \tag{3.35}$$

And then

$$dh = \frac{J_{O2} \cdot V_{SiO_2}}{m} \cdot dt \tag{3.36}$$

Integrating Equation (3.36) between h = 0 at t = 0 and h = h at t = t as illustrated earlier in Figure 2-18, we obtain

$$\int_{h=0}^{h=h} dh = \int_{t=0}^{t=t} \frac{J_{O2} \cdot V_{SiO_2}}{m} \cdot dt \tag{3.37}$$

$$(h - 0) = \frac{J_{O2} \cdot V_{SiO_2}}{m} \cdot (t - 0) \tag{3.38}$$

$$h = \frac{J_{O2} \cdot V_{SiO_2}}{m} \cdot t \tag{3.39}$$

Now, multiplying both sides by h and rearranging, we obtain

$$h^2 = \frac{J_{O2} \cdot h. V_{SiO_2}}{m} \cdot t \tag{3.40}$$

Also, considering that

$$\frac{h^2}{t} = kp \tag{3.41}$$

And substituting Equation (3.41) into Equation (3.40), we can rearrange to obtain

$$J_{O2} . h = \frac{m . kp}{V_{SiO_2}} \tag{3.42}$$

or

$$J_{02} . h = \frac{kp}{V_{SiO_2}} \quad m = 1, \text{for } O_2 \text{ reaction with silicon} \tag{3.43}$$

Here $J_{02} . h$ is the product of the flux and TGO thickness, which is defined as the oxygen permeability constant for TGO [69].

To estimate the TGO volume (V_{SiO2}), we consider Equation (2.1) describing the reaction of oxygen with silicon to form silicon dioxide:

$$Si\ (s) + O_2\ (g) = SiO_2\ (s) \tag{3.44}$$

Hereby, 1 mole of O_2 reacts to form 1 mole of SiO_2.

To estimate the molar volume (V_{SiO2}) of amorphous silica formed per mole of oxygen, we consider the density of SiO_2, ρ_{SiO2}(amorphous) = 2.2 g/cm^3, and its molecular weight, M_{SiO2} = 28+2*16 = 60 g/mole. As such, its density can be estimated as:

$$\text{Density} = \frac{\text{Weight}}{\text{Volume}} \tag{3.45}$$

Or the volume calculated as:

$$\text{Volume} = \frac{\text{Weight}}{\text{Density}} \tag{3.46}$$

$$V_{SiO_2} = \frac{60\ \text{g/ mole}}{2.2 * 10^6 \text{g/m}^3} = 27.27 * 10^{-6}\ \text{m}^3/\ \text{mol} \tag{3.47}$$

3.3 Oxygen permeability constant equation to describe experimental values

Equations (2.36) and (3.42) provide the oxygen permeability constant values for TC and TGO, respectively. The estimation of oxygen permeating through the top coat is done by using the volume of silicon dioxide (TGO) formed with respect to exposure time [74] as it depends on the amount of oxygen reacting with the bond coat. The expression is:

$$P = \frac{\rho_{SiO_2} * \mathbb{V}_{SiO_2}}{M_{SiO_2}.t} \tag{3.48}$$

In equation (3.48), $\mathbb{V}_{SiO2}$ is the TGO volume per unit area (x*y) as illustrated in

Figure 3-2 ; ρ_{SiO2} is the density of SiO_2; M_{SiO2} is the molecular weight of SiO_2; and t is the exposure time.

The oxygen permeability constant can then be written as:

$$P.l = \frac{\rho_{SiO_2} * \mathbb{V}_{SiO_2}}{M_{SiO_2}.t} * l \quad (l\ is\ the\ topcoat\ thickness) \tag{3.49}$$

The permeation area S and $\mathbb{V}_{SiO2}$ (m^3/m^2) for TGO is mathematically expressed as:

$$S = x * y \tag{3.50}$$

$$V_{SiO_2} = \frac{x * y * h}{S} \tag{3.51}$$

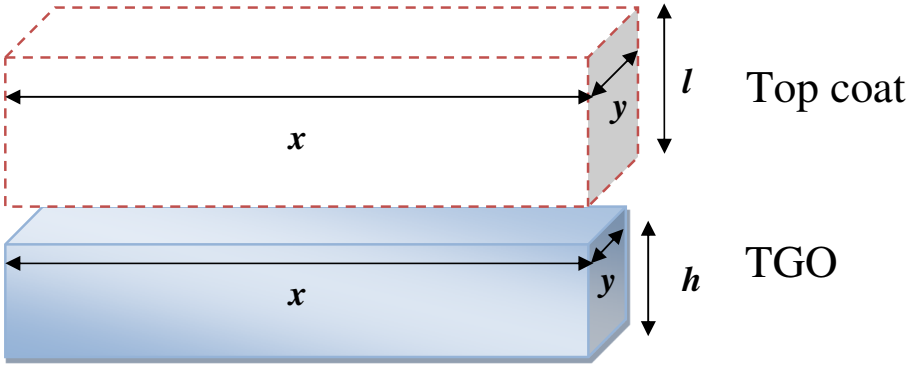

Figure 3-2: Top coat and TGO dimensions at time = t (hours).

Tables 3-2 and 3-3 summarize the constants and nomenclature used in this study.

Table 3-2: Exponents for dry oxygen and wet oxygen conditions.

Condition	p exponent value	q exponent value
Dry oxygen	-1/6	3/16
Wet oxygen (without proton)	-1/3	3/8
Wet oxygen (with a proton)	1	3/8

Table 3-3: Nomenclature of the equations.

Coating	Equation	Nomenclature

Top coat	$4P.l = A_o(P_{O_2}(h_i)^p - P_{O_2}(lo)^p) + A_{y_b}(P_{O_2}(h_i)^q - P_{O_2}(lo)^q)$	Equation A
Top coat	$P.\ l = \frac{\rho_{SiO2} * \gamma_{SiO2}}{MSiO_2.t} * l$	Equation B
TGO	$J_{O_2}.h = \frac{mk_P}{V_{S_iO_2}}$ m=1, for O_2 diffusing specie	Equation C

The total permeability constant values for the top coat are estimated using Equation A and the different combinations of p and q exponents are shown in Table 3-2.

3.4 Determining the variables for oxygen permeability constant calculations

To calculate the oxygen permeability constant, the initial parameters need to be estimated. In this section, the used software and parameters are introduced. It shall be noted that the percentage of porosity present in the top coat can affect the oxidant permeation. In an effort to account for this, the porosity or void present in the top coat is subtracted from its original thickness (l) as shown in Equation (3.52).

$$\text{Effective top coat thickness } (l') = (100 - \%\text{age porosity}) * l \quad (3.52)$$

The percentage of porosity is estimated using Image J software analysis of SEM micrographs of the top coat material.

3.4.1 Estimation of the A_o and A_{yb} factors

The temperature is one of the major factors influencing the oxygen permeability constant. Correspondingly, the Arrhenius relationship is used to describe the variation of A_o and A_{yb} with temperature (both notated in Equation (3.53) as A_i).

$$A_i = A_i^* \exp(^{-Q_i}/_{RT}) \quad (3.53)$$

Where A_i^* is the pre-exponential factor; Q_i is the activation energy for oxidant permeation; R is the gas constant; and T is the temperature in Kelvin. A_o and A_{yb} determine the oxygen vacancy mobility and the ytterbium vacancy mobility with respect to temperature, respectively.

Figure 3-3 and Figure 3-4 below show the log-log plots of A_o and A_{yb} as functions of the inverse of temperature.

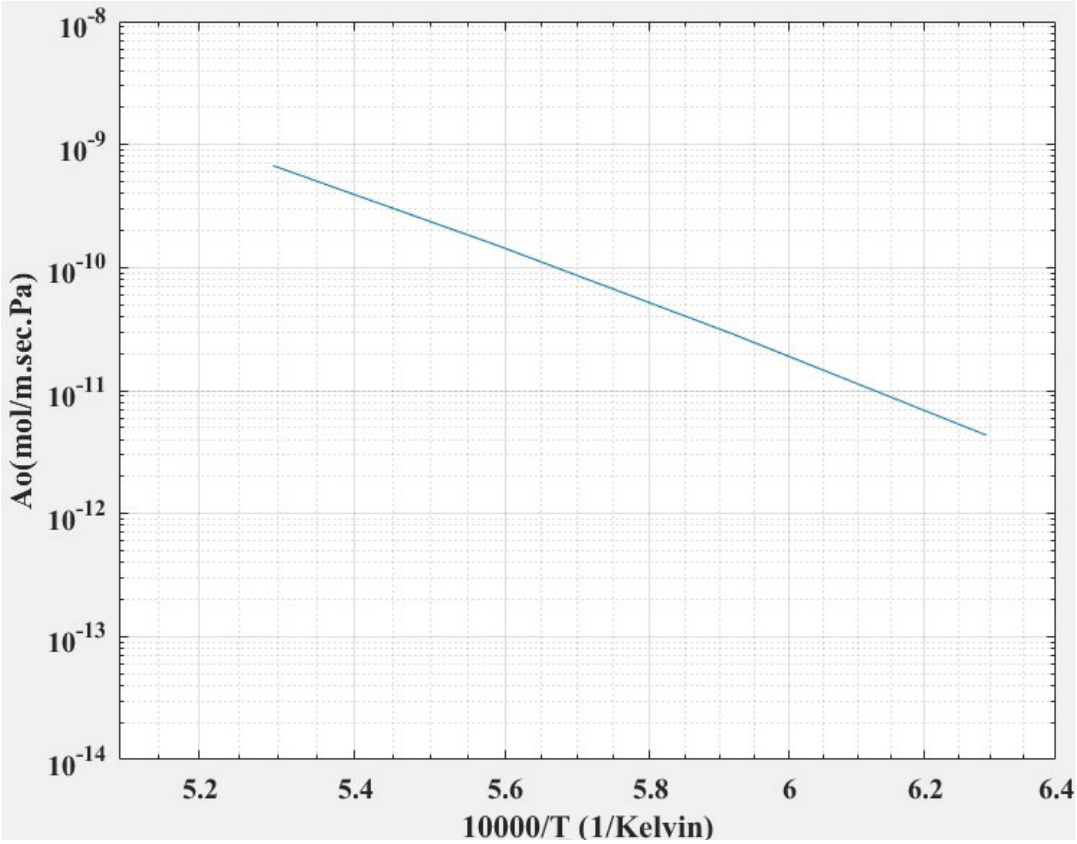

Figure 3-3: Oxygen vacancy mobility with respect to temperature [59].

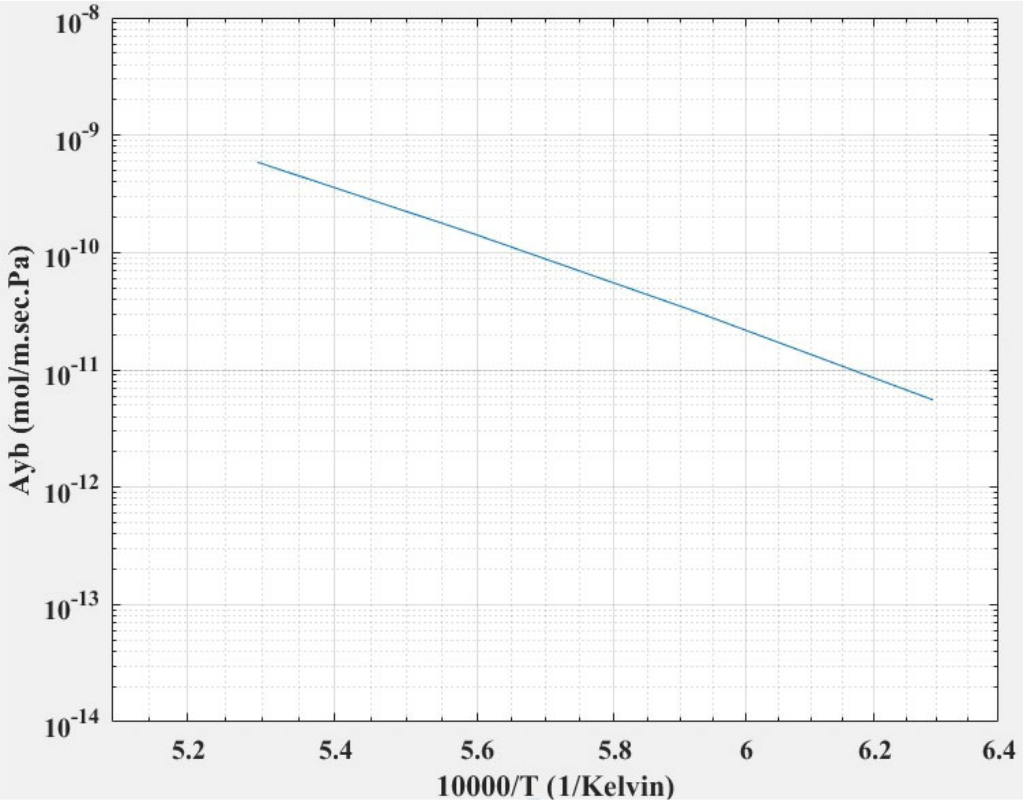

Figure 3-4: Ytterbium vacancy mobility with respect to temperature [59].

3.4.2 Estimation of the oxygen partial pressure at the TC/TGO interface and of the parabolic rate constant

FactSage is used to estimate the oxygen partial pressure at the TC/TGO interface. It is a thermodynamic Databank System at a single place, introduced in 2001. It is a combination of FACT-Win/F*A*C*T and CemSage/SOLGASMIX thermochemical packages. This combination offers a large thermochemical database and translates the data into useful information under variable conditions. The used *FactSageEdu* package is an open-source that is available online at www.FactSage.com.

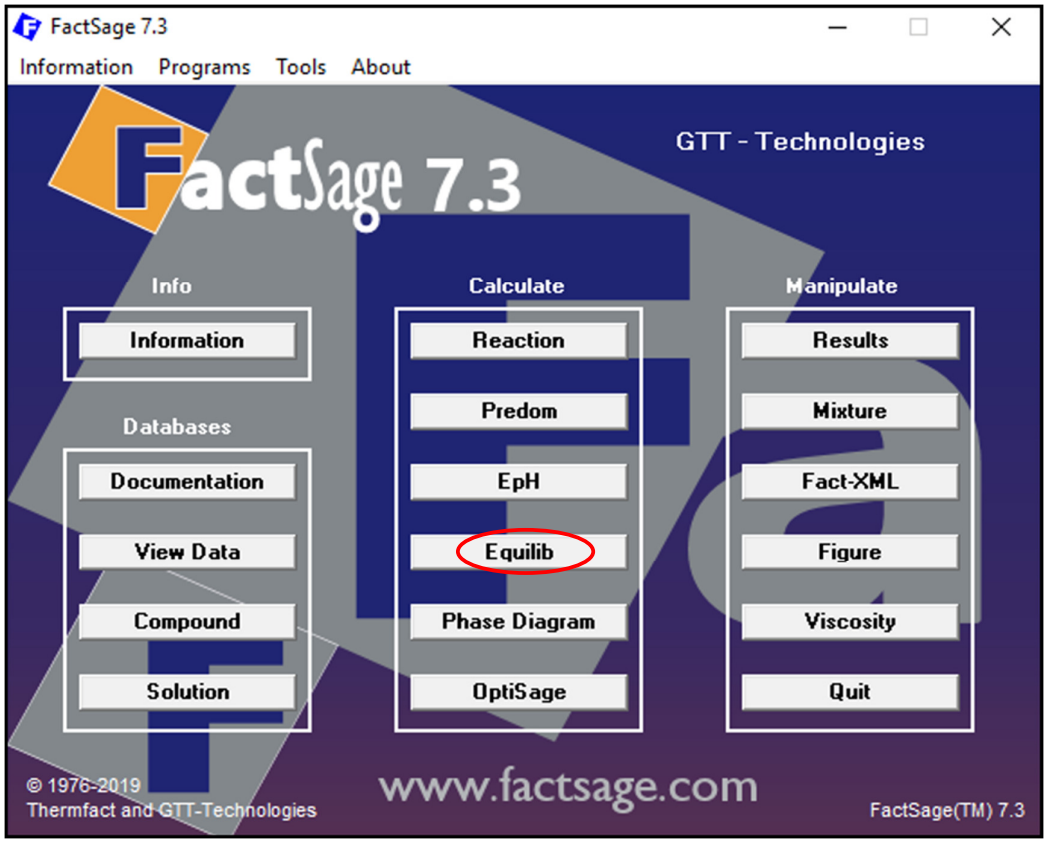

Figure 3-5: FactSageEdu 7.3 displaying various modules; the red mark indicates the Equilib module used in this study.

The platform offers multiple modules as illustrated in Figure 3-5. They include: (1) the Info module that provides necessary instructions about the module overview; (2) the Databases module contains a large database for compounds and elements; (3) the Calculate module enables the user to compute the various thermochemical properties for a single element or a system; and (4) the Manipulate module allows users to pre-define the reactant input and get the result in the desired manner [75].

In this study, the *Equilib sub-module* within the Calculate module is used to estimate the oxygen partial pressure at the TC/TGO interface. In our case, the input

material/system is $Yb_2Si_2O_7$-SiO_2-O_2, where $Yb_2Si_2O_7$ is the top coat material, and SiO_2 is the TGO material in equilibrium with the O_2 partial pressure. The inputs are initial conditions, the temperature (degree Celsius), and the total pressure (atm) of interest.

The main shortcoming of the FactSageEdu - open source is the limitation of the number of input elements. Specifically, only chemical systems with three elements or less can be studied to obtain the partial pressure. For instance, it is possible to study the $Yb_2Si_2O_7$-SiO_2-O_2 system that contains the three elements: Yb, Si, and O. But, the water vapor cannot be included in the study as it would form a fourth element in the system: $Yb_2Si_2O_7$-SiO_2-H_2O, or Yb, Si, O, H. To address this limitation, the water vapor is studied by considering the same equilibrium oxygen partial pressure at the TC/TGO interface as obtained from the three-element system $Yb_2Si_2O_7$-SiO_2-O_2.

To estimate the Parabolic rate constant kp, we consider that the rate of growth of TGO, expressed as the square of the TGO thickness, is linearly related to time (t). The parabolic rate constant described in Equation (3.41) is then obtained using non-linear curve fitting of the h^2-t plot.

3.4.3 Estimation of the top coat porosity using the Image J software

To estimate the porosity percentage in the top coat, image analysis is performed on SEM micrographs obtained from existing literature using the Image J software. Its user interface is illustrated in Figure 3-6. This software is developed by the National Institutes of Health, USA, and gained popularity due to its simple user interface. It is easy to extract relevant information like grain size, porosity, particle size, and more.

While working on this software, it is very important to keep proper magnification of the image to be studied, as over-magnified or under-magnified images can alter the results. Moreover, the selection of proper imaging contrast, brightness, and operating mode is important for accurate results.

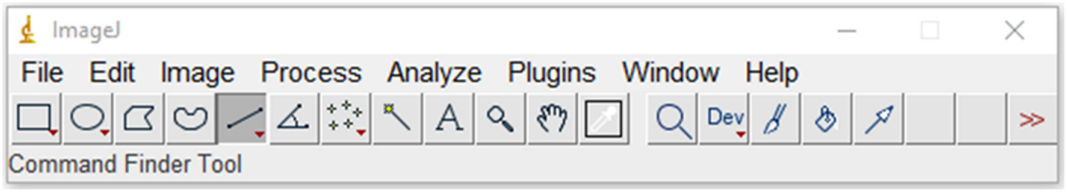

Figure 3-6: Image J software menu bar.

For image analysis, areas of interest are selected on a cross-sectional SEM image. The image is then converted into a binary image. The scale is adjusted to match the image magnification, and the gray scale threshold is adjusted to allow the software to properly differentiate pores from their surrounding material. The porosity percentage is finally retrieved from the percentage area section. Additional information like average pore size, total area, Feret diameter, Feret angle, and circularity can also be obtained using this software.

4 Results

To understand the effect of partial pressure, three different environment conditions: 10% H_2O + 90% O_2, 50% H_2O + 50% O_2, and 90% H_2O + 10% O_2 are studied at a constant temperature of 1523 K. Later, the effect of temperature is investigated on the 50% H_2O + 50% O_2 environment at 1423 K, 1473 K, 1523 K, and 1573 K. Finally, the effect of top coat dopants is explored by considering the following modifiers: Yb_2Si_2O (100 wt% $Yb_2Si_2O_7$); 6A (6 wt% alumina + 94 wt% $Yb_2Si_2O_7$); M2Y (1.39 wt% mullite + 2.33 wt% YAG + 96.28 wt% $Yb_2Si_2O_7$); 3M (2.78 wt% mullite + 97.22 wt% $Yb_2Si_2O_7$); 2Y (2.33 wt% YAG + 97.67 wt%$Yb_2Si_2O_7$); M5Y (1.39 wt% mullite + 4.66 wt% YAG + 93.95 wt% $Yb_2Si_2O_7$); M (1.39 wt% mullite + 98.61 wt% $Yb_2Si_2O_7$); AT (1 wt% alumina + 1 wt% titania + 98 wt% $Yb_2Si_2O_7$); MT (1.39 wt% mullite + 1 wt% Titania + 97.61 wt% $Yb_2Si_2O_7$). Table 4-1 lists the formed TGO thickness values for different top coat compositions, oxidizing environment and exposure times of 100 hrs, 500hrs and 1000 hrs in wet environment containing oxygen and water vapor.

Table 4-1: Thermally grown oxide (TGO) thickness (μm) with respect to time (hr) for different top coat compositions and oxidizing environment [36]**.**

Top coat	**Thickness (μm) at 100 hr**	**Thickness (μm) at 500 hr**	**Thickness (μm) at 1000 hr**
$Yb_2Si_2O_7$ (dry oxygen)	0.8	2.0	3.3
$Yb_2Si_2O_7$ (wet oxygen)	4.7	10.6	13.2

6A	0.2	1.3	1.9
M2Y	1.0	1.4	1.7
3M	1.4	1.4	2.5
2Y	1.5	3.7	3.7
M5Y	0.8	1.3	2.4
M	4.0	11.6	16.3
AT	3.4	7.4	10.0
MT	4.8	10.8	10.8

*wet environment conditions = 90% H_2O + 10 % O_2.

Using the Origin 6.1 software and the experimental data in Table 4-1, the parabolic rate constant (kp, in Equation (2.26)) is calculated as the slope of the linear relationship between the square of the TGO thickness and the exposure time. The estimated parabolic rate constants (kp) for all the investigated EBC systems are given in Table 4-2 and show the effect of both oxygen and water vapor.

Table 4-2: Parabolic rate constants for Silicon dioxide (TGO) in dry and wet oxygen environments for different top coat compositions at 1589K.

Top coat	**Conditions**	**Parabolic rate constant kp ($\mu m^2/hr$)**
$Yb_2Si_2O_7$	Dry oxygen	0.01
$Yb_2Si_2O_7$	Wet oxygen	0.184
6A	Wet oxygen	0.00354
M2Y	Wet oxygen	0.00315
3M	Wet oxygen	0.00292

2Y	Wet oxygen	0.01648
M5Y	Wet oxygen	0.00529
M	Wet oxygen	0.26553
AT	Wet oxygen	0.10201
MT	Wet oxygen	0.14069

*dry oxygen condition = 21% O_2; wet environments = 90% H_2O + 10 % O_2.

To include the effect of temperature, the temperature dependent oxygen partial pressures in equilibrium with $Yb_2Si_2O_7$ – SiO_2 at the TC/TGO interface are obtained using the FactSage 7.3 software as summarized in Table 4-3. The detailed steps to retrieve the data are provided in the Appendix.

Table 4-3: Oxygen partial pressure at TC/TGO interface with respect to temperature from FactSage 7.3 software.

Temperature (Kelvin)	**Oxygen Partial Pressure (atm)**	**Oxygen Partial Pressure (Pa)**
1423	$1.0866*10^{-11}$	$1.10*10^{-6}$
1473	$4.9512*10^{-11}$	$5.02*10^{-6}$
1523	$2.0385*10^{-10}$	$2.07*10^{-5}$
1573	$7.6579*10^{-10}$	$7.76*10^{-5}$
1589	$1.15*10^{-9}$	$1.17*10^{-4}$

* 1 atm = 101325 Pascal

It can be seen in Table 4-3 that the oxygen partial pressure at the TC/TGO interface increases with temperature. Now, the partial pressure unit in Equation A is pascal. Thus, the obtained partial pressure unit has to be converted from atm to pascal (Pa) by multiplying by factor 101325.

Figure 4-1 contains the porosity percentage in the top coat as measured using the Image J analyser. It can be seen that the porosity after 1000 thermal cycles of 1-hour duration with 1589 K peak temperature is lower than the as-sprayed coatings, suggesting that sintering and densification take place over the time at high temperature [76].

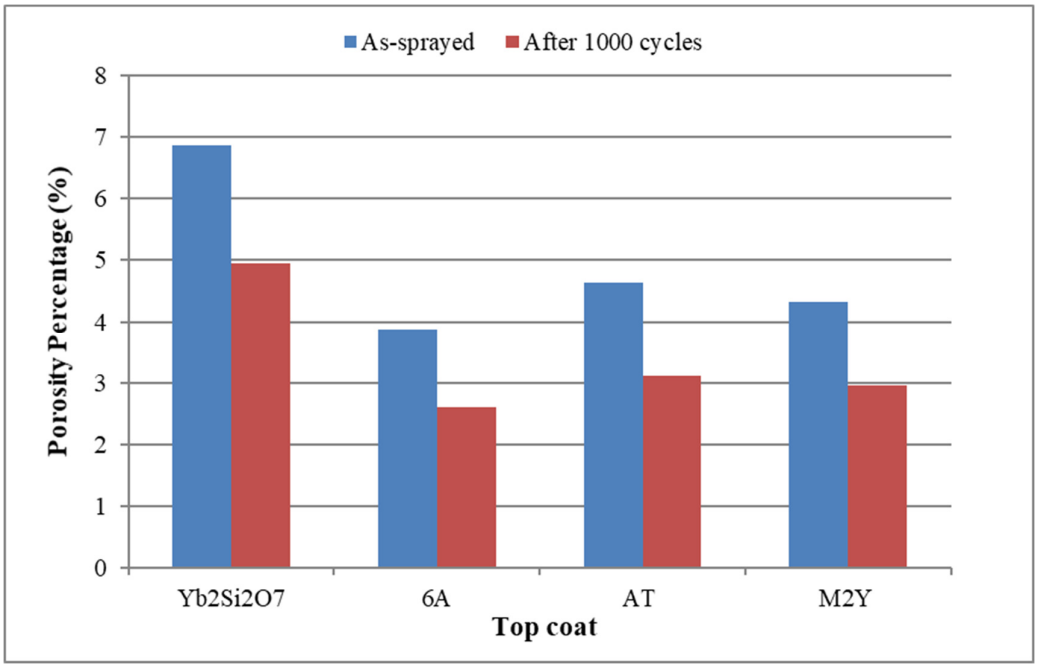

Figure 4-1: Percentage porosity in top coat samples, as-sprayed, and after 1000 thermal cycling. The cycle duration is 1 hour and the peak temperature is 1589 K.

Table 4-4 summarizes the oxygen permeability constants for top coat in as-sprayed and after 1000 cycle conditions. The values are nearly identical, suggesting that the porosity has a negligible effect on the top coat oxygen permeability constant. Thus, for further study, we ignore the effect of porosity and consider the top coat to be fully dense without consideration of porosity.

Table 4-4: Effect of porosity percentage on the top coat oxygen permeability constant.

Conditions	**Oxygen permeability constant (TC, mol/m. sec)**
No porosity	$1.23*10^{-10}$
As-sprayed	$1.15*10^{-10}$
After 1000 cycles	$1.17*10^{-10}$

*Equation A is used to calculate the oxygen permeability constants at 1589 K in wet environment with 90% H_2O and 10% O_2.

Figure 4-2 shows the temperature dependence of the oxygen permeability constant in dry oxygen from the literature [69] and as calculated in this work using parabolic rate constants from the literature [73].

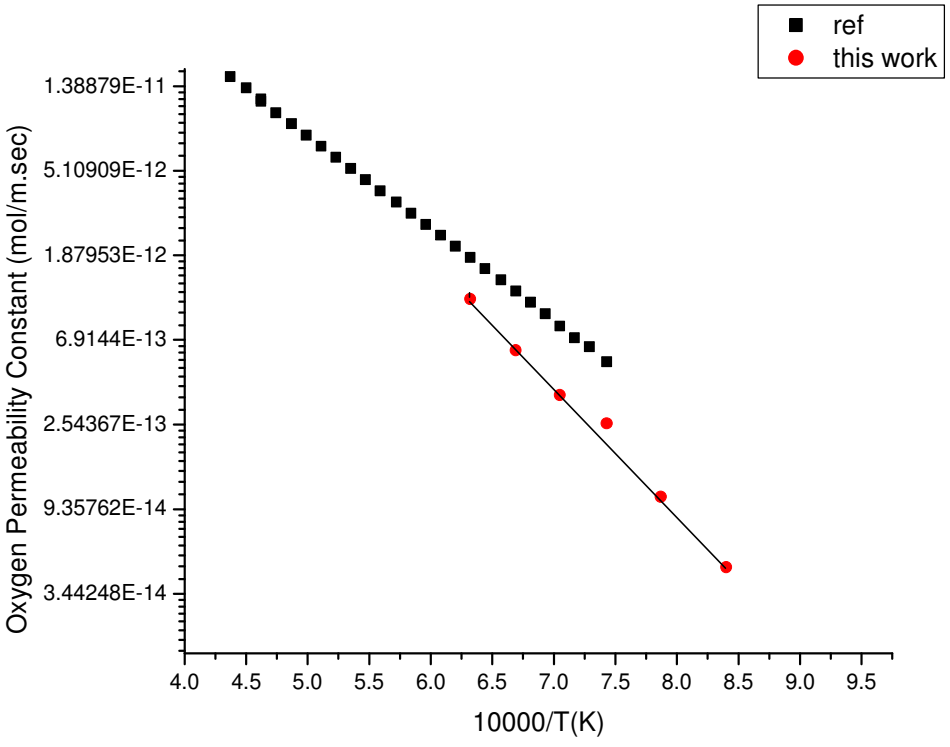

Figure 4-2: Temperature dependence of the oxygen permeability constant through TGO.

To obtain comparable literature values for validation, the oxygen permeability constant units are converted from grams of O_2 per unit thickness per unit time to mol/m.sec, as demonstrated in Equation (4.1).

$$\frac{gram\ of\ O_2}{cm.sec} = \frac{1}{32} * \frac{1}{10^{-2}} \frac{mole}{m.sec} \tag{4.1}$$

Both literature and calculated values show a similar trend whereby the oxygen permeability constant of silicon dioxide (TGO) increases with temperature or with decreasing inverse of the temperature (1/T). This good agreement validates Equation C. Therefore, it is used for further calculations in the following sub-sections.

4.1 TC and TGO oxygen permeability constants

For the top coat, the modelled relationship between the oxygen permeability constant in dry oxygen and the oxygen partial pressure gradient at 1589 K is given in Figure 4-3. The used oxygen permeability constant input parameters are given in Table 4-5.

Table 4-5: Parameters used to calculate the top coat oxygen permeability constant.

Parameters	
Temperature	1589 K
A_{yb}	$1.39*10^{-12}$
A_o	$1.08*10^{-12}$
'p' exponent	- 1/6
'q' exponent	3/16

The frequency factors A_{yb} and A_o are taken from Figure 3-4 and Figure 3-3, respectively, while the p and q exponents are taken from Table 3-2, and experimental datas are taken from Table 4-1 and Table 4-2.

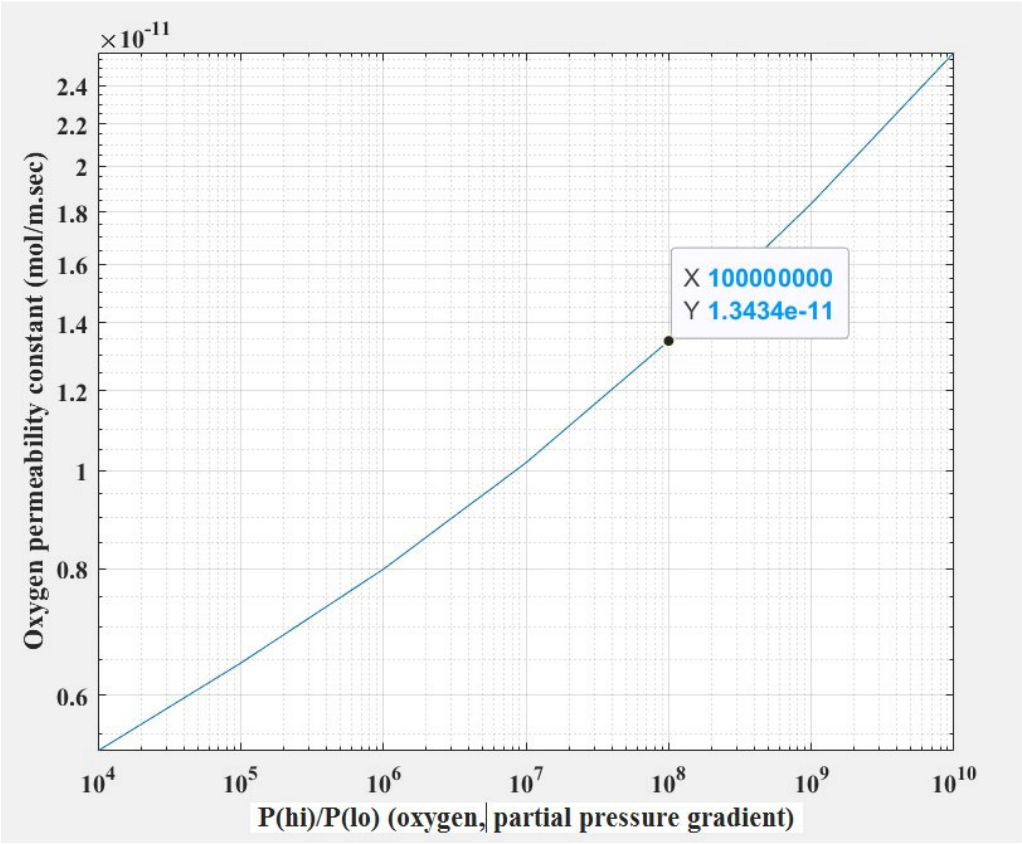

Figure 4-3: Estimated log-log plot of the oxygen permeability constant of the top coat versus oxygen partial pressure gradient in dry oxygen.

Considering the specific case of this study where the oxygen partial pressures are $2.13*10^4$ Pa at the gas/TC interface and $1.17*10^{-4}$ Pa at the TC/TGO interface, the oxygen partial pressure gradient (P(hi)/P(lo)) can be calculated as 10^8, and the resultant TC oxygen permeability constant as $1.343*10^{-11}$mol/m.sec as indicated by the data point highlighted in Figure 4-3. For the TGO, an oxygen permeability constant of $1.01862*10^{-13}$ mol/m.sec is estimated for the dry oxygen condition using the parabolic

rate constant (kp) calculated considering data from Table 4-2. It is found that the oxygen permeability constant of TGO is lower than that of TC, which is in agreement with previous findings [36].

In contrast to dry oxygen, the p and q constants strongly dependent on the defect reaction in wet oxygen as derived earlier in section 3.1 and summarized in Table 3-2. In this study, both wet oxygen cases of defect reactions, with proton and without proton, are considered to calculate the oxygen permeability constant of the top coat using Equation A as shown in Table 4-6.

Table 4-6: Oxygen permeability constants of the top coat in wet oxygen at 1589 K for defect reactions with and without proton.

Case	**p exponent**	**q exponent**	**Oxygen permeability constant TC (mol/m.sec)**
Wet oxygen (without proton)	-1/3	3/8	$1.23*10^{-10}$
Wet oxygen (with proton)	1	3/8	$-9.87*10^{-08}$

* wet oxygen condition (90% H_2O + 10% O_2)

The results in Table 4-6 suggest that for the defect reaction with proton, the oxygen permeability would be negative, which is opposite to the fundamental laws of diffusion. Therefore, this case is discarded, and further calculations are based only on the case of defect reaction without proton. The estimation is based on Equation A and the input parameters are summarized in Table 4-7. The results are also plotted in Figure 4-4 and

show that the oxygen permeability constant of TC increases with the water vapor partial pressure gradient across the layer.

Table 4-7: Parameters used to calculate the oxygen permeability constant of the top coat in wet oxygen.

Parameters	
Temperature	1589 K
A_{yb}	$1.39*10^{-12}$
A_o	$1.08*10^{-12}$
p exponent	-1/3
q exponent	3/8

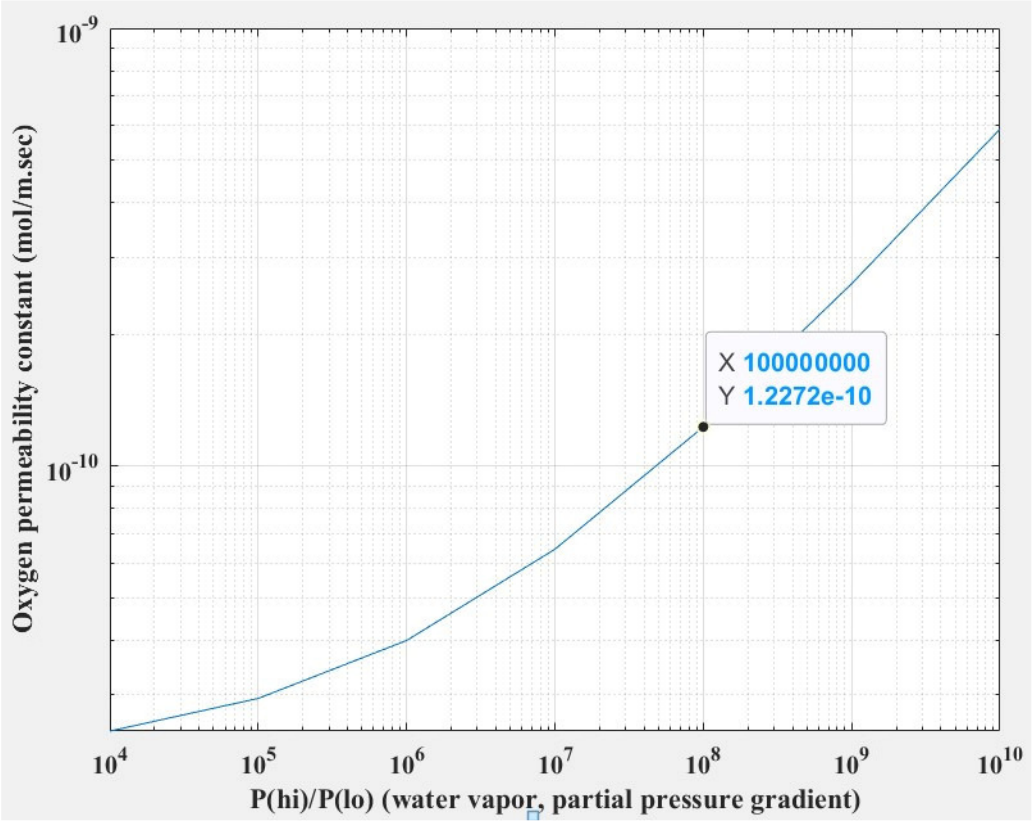

Figure 4-4: Oxygen permeability constant of the top coat versus the oxygen partial pressure gradient.

In the specific case of this study, the water vapor partial pressure at the gas/TC interface P(hi) is $9.13*10^{4}$ Pa and that at the TC/TGO interface P(lo) is $1.165*10^{-4}$ Pa. The corresponding TC oxygen permeability constant is estimated as $1.23*10^{-10}$mol/m.sec as indicated by the data point highlighted in Figure 4-4 above.

The oxygen permeability constant of TGO is estimated to be $3.74*10^{-12}$ mol/m.sec in wet oxygen as calculated using the parabolic rate constant (kp) from Table 4-2, which is lower than that of TC, similar to the previous results for the dry oxygen environment. This is confirmed by Table 4-8 suggesting that the oxygen permeability constant of TC is nearly 131 times and 33 times higher than that of TGO in dry and wet oxygen conditions, respectively, in agreement with the findings of Sullivan [67]. Therefore, we can conclude that the TGO seems to be the diffusion rate controlling layer for both dry and wet oxygen conditions.

Table 4-8: Ratios of oxygen permeability constant of TGO over TC in dry and wet oxygen conditions.

Conditions	**Ratio ($\frac{TGO}{TC}$)**
Dry oxygen	0.0076
Wet oxygen	0.0304

* wet oxygen (90% H_2O = 10% O_2), dry oxygen (21% O_2) at 1589 K.

Furthermore, the oxygen permeability constants of TC and TGO layers are compared in Table 4-9 for both dry oxygen and wet oxygen conditions after 1000 hrs exposure at 1589 K.

Table 4-9: Ratios of oxygen permeability constants between dry oxygen and wet oxygen conditions at 1589 K, exposed for 1000 hrs.

Oxygen permeability constant (mol/m. sec)	**Ratio** $(\frac{Wet}{Dry})$
TC	9.18
TGO	18.35

It can be seen that water vapor strongly increases the oxygen permeation through both TC and TGO. The increases are by factors 9.16 and 18.35 for the top coat and TGO, respectively.

Table 4-10 compares the TC and TGO oxygen permeability constants obtained in this study to available literature data [68].

Table 4-10: Oxygen permeability constants through TC and TGO as obtained in this work and from literature; and the ratio of oxygen permeability constants through TC and TGO of this work to reference work in dry oxygen.

Reference	**TC (mol/m. sec)**	**TGO (mol/m. sec)**	**TC** $(\frac{This\ work}{Reference})$	**TGO** $(\frac{This\ work}{Reference})$
Deal and Grove , Sullivan*	7.83×10^{-12}	1.176×10^{-13}	1.72	0.866

Norton , Sullivan*	$4.47x10^{-12}$	$6.72x10^{-14}$	3.00	1.52
This work	$1.34x10^{-11}$ (dry oxygen)	$1.02x10^{-13}$ (dry oxygen)		
	$\hat{}1.23x10^{-10}$ (wet oxygen)	$\hat{}3.74x10^{-12}$ (wet oxygen)		

*literature values are taken from reference [67]; ^ oxygen permeability constant in wet oxygen conditions.

4.2 Role of the different factors in determining the oxygen permeability constant

4.2.1 Effect of exposure time

Equations A and C are time independent as they assume steady-state permeation, meaning the rate of permeation is constant. In contrast, Equation B is time dependent, which reflects the experimental observation of non-steady-state diffusion.

Table 4-11 summarizes the oxygen permeability constant (*P.l*) of TC in dry oxygen at 1589 K as calculated using Equation B (Equation (3.48)). Different exposure times of 100 hr, 500 hr, and 1000 hr are considered, whereby the top coat thickness is assumed to remain constant at 250 μm irrespective of the exposure time [36].

$$P.l = \frac{2.2*10^{6}*\text{Ɣ}SiO2}{60*t*3600} *(250*10^{-6}) \quad (3.48)$$

The data of the thermally grown oxide volume per unit area ($\tilde{\mathbb{V}}_{SiO_2}$) as a function of exposure time are taken from the literature [36].

Table 4-11: Top coat oxygen permeability constant estimated using Equation B and literature data [36] of the thermally grown oxide volume per unit permeation area in dry oxygen.

Time (t, in hr)	$\tilde{\mathbb{V}}_{SiO_2}$ **(m^3/m^2)**	$\frac{\tilde{\mathbb{V}}_{SiO_2}\left(\frac{m3}{m2}\right)}{t\,(sec)}$	**Oxygen permeability constant, TC (mol/m.sec)**
100	$0.80*10^{-6}$	$8*10^{-9}$	$2.04*10^{-11}$
500	$2.0*10^{-6}$	$4*10^{-9}$	$1.0185*10^{-11}$
1000	$3.3*10^{-6}$	$3.3*10^{-9}$	$8.402*10^{-12}$

* exposed for 100 hr, 500 hr, and 1000 hr in dry oxygen (21% O_2) at 1589 K. top coat thickness (*l*) fixed constant at 250μm

As expected from non-steady-state diffusion, the oxygen permeability constant decreases with exposure time. The decrease is by 50% and 17% from 100 hr to 500 hr and from 500 hr to 1000 hr, respectively. This is reflected in Equation B in the direct proportionality between the oxygen permeability and the ratio $\frac{\tilde{\mathbb{V}}_{SiO_2}}{t}$ of the thermally grown oxide volume per unit area per exposure time.

The oxygen permeability constant of TC calculated earlier in section 4.1 using Equation A is $1.343*10^{-11}$ mol/m.sec, which lies between $2.04*10^{-11}$ and $1.0185*10^{-11}$ as calculated from Equation B at 100 hr and 500 hr of exposure time, respectively.

The estimated oxygen permeability constants of TC in wet environment (90% H_2O + 10% O_2) at 1589 K are summarized in Table 4-12 for 100 hr, 500 hr, and 1000 hr exposure times.

Table 4-12: Top coat oxygen permeability constants estimated using Equation B and literature data of the thermally grown oxide volume per unit permeation area in wet environment.

Time (t, in hr)	$\bar{V}_{SiO2}$ **(m^3/m^2)**	$\frac{\bar{V}_{SiO_2}(m^3/m^2)}{t(hr)}$	**Oxygen permeability constant, TC (mol/m.sec)**
100	$4.7*10^{-6}$	$4.7*10^{-8}$	$1.20*10^{-10}$
500	$10.6*10^{-6}$	$2.12*10^{-8}$	$5.40*10^{-11}$
1000	$13.2*10^{-6}$	$1.32*10^{-8}$	$3.36*10^{-11}$

*exposed for 100 hr, 500 hr, 1000 hr, in wet environment (90% H_2O + 10% O_2) at 1589K and fixed top coat thickness (l) = 250μm.

Here too, the non-steady-state nature of the diffusion through the top coat is reflected in decreasing oxygen permeability constant with exposure time, with drops by 55% and 37% as the exposure time increases from 100 to 500 hrs and from 500 to 1000 hrs, respectively.

4.2.2 Effect of temperature

Figure 4-5 shows the oxygen permeability constant curves for the top coat vs temperature as calculated using equation A. Dry oxygen (p = -1/6, q = 3/16) and wet oxygen (p = -1/3, q = 3/8) conditions as well as different temperatures of 1423K, 1473K, 1523 K, and 1573K are considered. The total pressure is considered constant at 1 atm, with 50% H_2O + 50% O_2 for the wet environments. As such, the obtained total oxygen permeability is the result of both the dry oxygen and the water vapor contributions. The data points calculated for the wet oxygen condition using Equation B are also plotted in Figure 4-5 and show a good agreement with the total permeability constant values obtained from Equation A. For calculations using Equation B, the input

data are collected from literature [66] where the authors reported experimental variation of the TGO thickness with temperature as shown in Table 4-13. Here, the constant top coat thickness *l* is 50 μm.

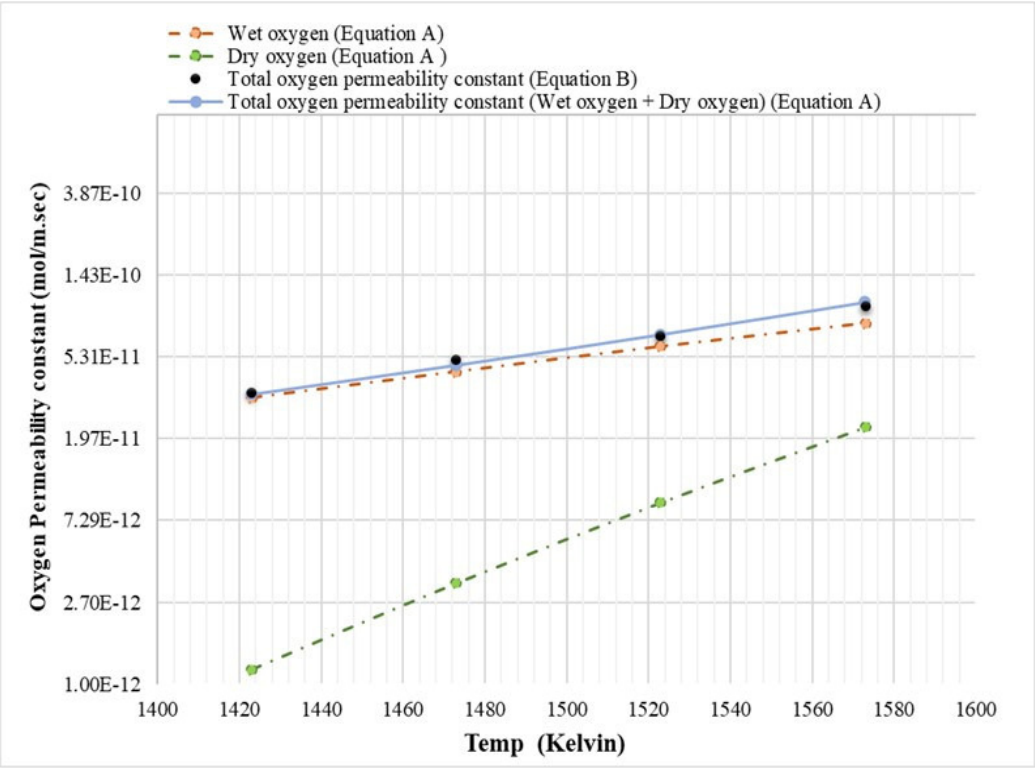

Figure 4-5: Oxygen permeability constant through YbDS top coat vs. temperature, as calculated for wet environment (50% H_2O + 50% O_2), and 200 hr exposure time.

Table 4-13: Experimental literature data of the thermally grown oxide thickness vs. temperature [66] used for Equation B calculations.

Temperature (Kelvin)	**TGO thickness (m)**
1423	$1.60*10^{-6}$
1473	$2.40*10^{-6}$

1523	$3.20*10^{-6}$
1573	$3.52*10^{-6}$

* exposed to wet environments of 50% H_2O + 50% O_2 for 200 hours.

The calculation results clearly show an increase in oxygen permeability constant as the exposure temperature increases. Furthermore, the oxygen permeability due to water vapor is much higher than that due to dry oxygen.

Thermodynamically, the temperature dependence of permeation processes can be described using the Arrhenius Equation (3.53), allowing the estimation of the frequency factor (A^*) and the activation energy (Q_i) for both oxygen and ytterbium ion diffusion. The determination of the two constants is done using curve fitting of Equation A for water vapor values in Figure 4-5. The results are presented in Table 4-14.

$$A_i = A_i^* \exp(^{-Q_i}/_{RT}) \tag{3.53}$$

In Equation (3.53), A_i stands for the A_0 and A_{yb} for oxygen and ytterbium ion diffusion in Equation (4.2), respectively.

Table 4-14: Pre-exponential frequency factor and activation energy for oxide and ytterbium ion as estimated by curve fitting.

Ion type	**Pre-exponential frequency factor (A_i , mol/m.sec.Pa^n)**	**Activation energy (Q_i , kJ/mol)**
Oxide	$2.56*10^{-2}$	288.35
Ytterbium	$5.45*10^{1}$	619.2

Agreement of the Arrhenius equation and Equation A is obtained by introducing a correction factor β = 7 as shown in Equation 4.2:

$$\beta\ P.l = A_o(P_{O_2}(h_i)^p - P_{O_2}(lo)^p) + A_{y_b}(P_{O_2}(h_i)^q - P_{O_2}(lo)^q) \qquad (4.2)$$

The calculated constants A_o and A_{yb} are plotted over the temperature in Figure 4-6 and Figure 4-7, respectively.

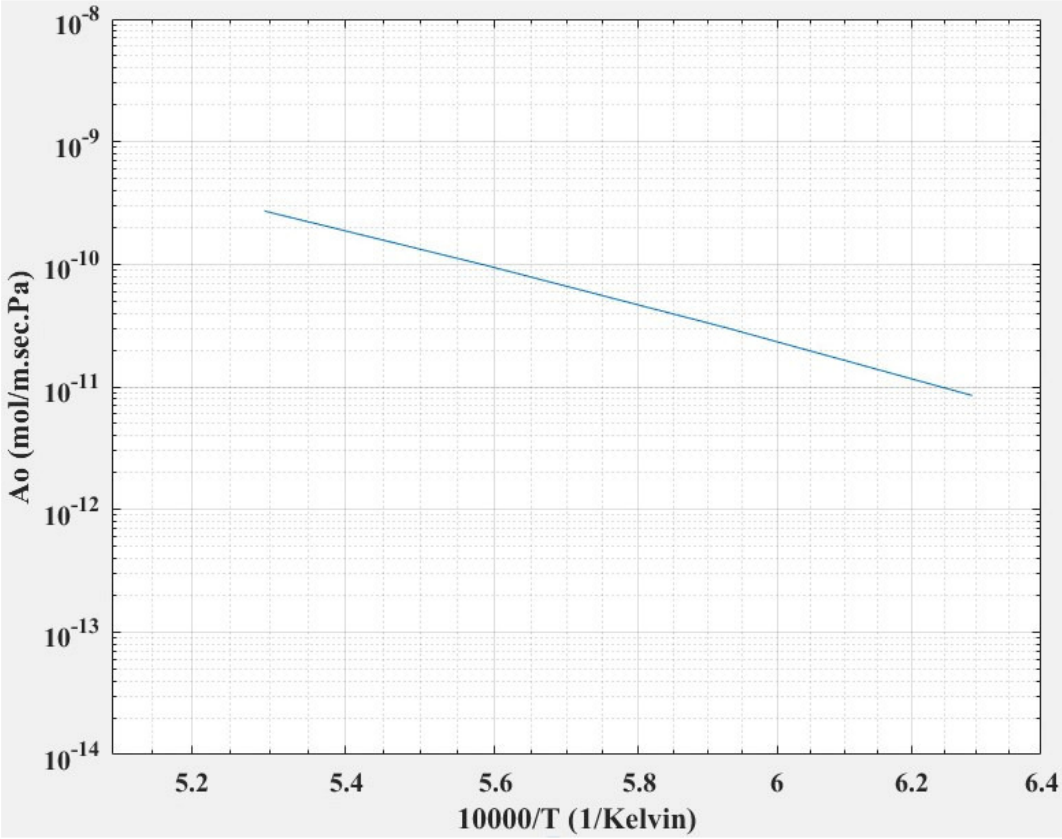

Figure 4-6: A_o vs. temperature for wet environment (50%H_2O + 50 %O_2).

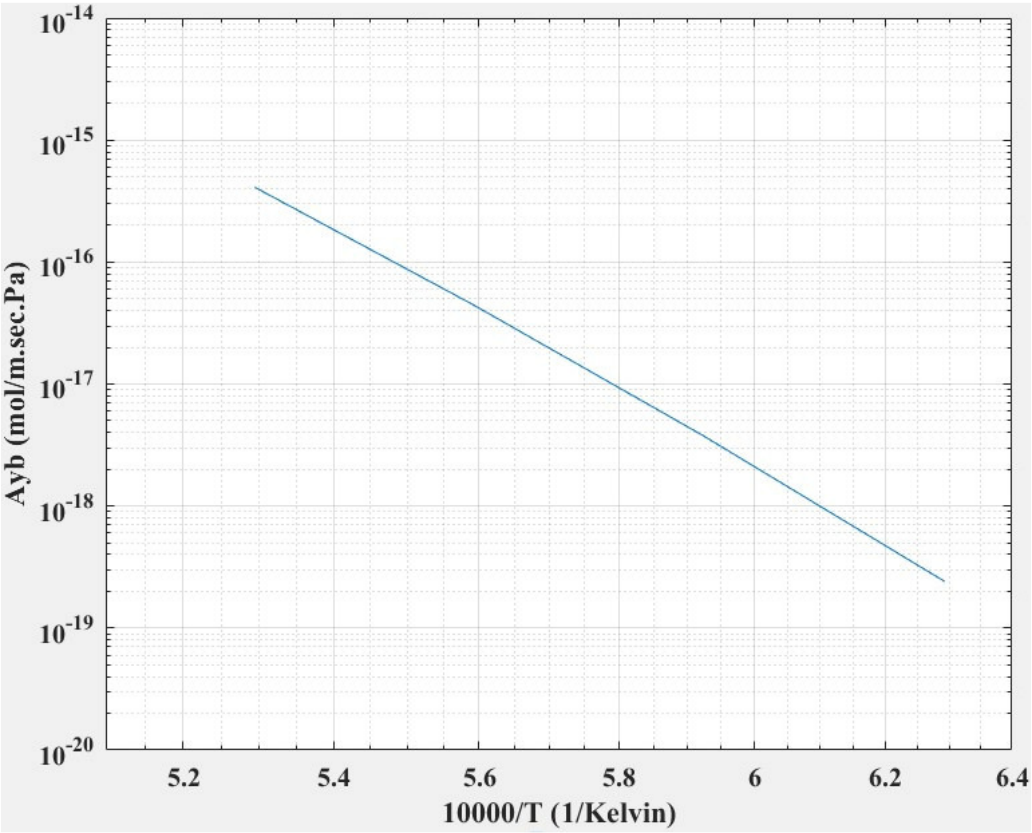

Figure 4-7: A_{yb} vs temperature for wet environment (50% H_2O + 50 %O_2).

Figure 4-8 comparatively shows the oxygen permeability constants of TC and TGO as calculated using Equation B and Equation C, respectively. The temperature dependent parabolic rate constants from literature and the resulting TGO oxygen permeability constant values as a function of temperature are shown in Table 4-15.

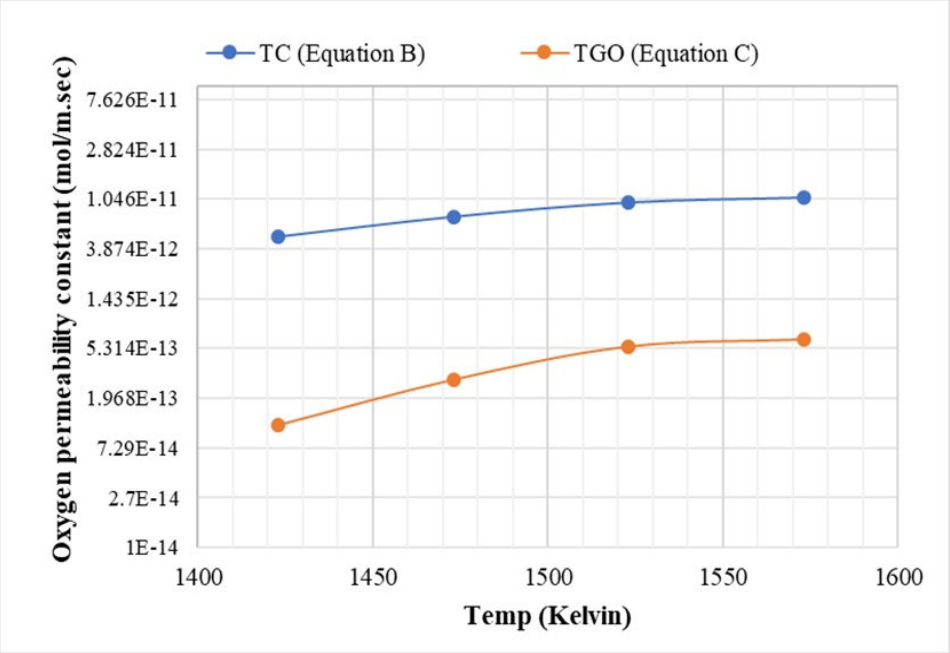

Figure 4-8: Temperature dependence of the oxygen permeability constant for top coat and TGO.

Table 4-15: Parabolic rate constant [66] and TGO oxygen permeability constant vs. temperature as calculated using Equation C.

Temperature (Kelvin)	**Parabolic rate constant, k_p ($\mu m^2/hr$)**	**Oxygen permeability constant TGO (mol/m.sec)**
1423	0.0114	$1.161*10^{-13}$
1473	0.0280	$2.852*10^{-13}$
1523	0.0539	$5.490*10^{-13}$
1573	0.0618	$6.295*10^{-13}$

* wet environment (50% H_2O + 50% O_2), exposed for 200 hours.

In agreement with earlier results, the oxygen permeability of the TGO is much lower compared to that of the TC. Also, for both layers, the oxygen permeability increases with temperature similar to the results shown earlier in Figure 4-5.

4.2.3 Effect of partial pressure

The oxygen permeability constants of TC for 200 hr exposure time as calculated using Equation A for a constant temperature of 1523 K and different wet environments 10% H_2O + 90% O_2, 50% H_2O + 50% O_2, and 90% H_2O + 10% O_2 are shown in Figure 4-9. For validation, the results from Equation B are also plotted in this graph. It can be seen that the individual permeability contributions of oxygen and water vapor continuously increase with their respective partial pressures. Similar to our earlier observation and previous literature [58] [59], water vapor plays a stronger role. Therefore, the overall oxygen permeability constant increases with the water vapor partial pressure.

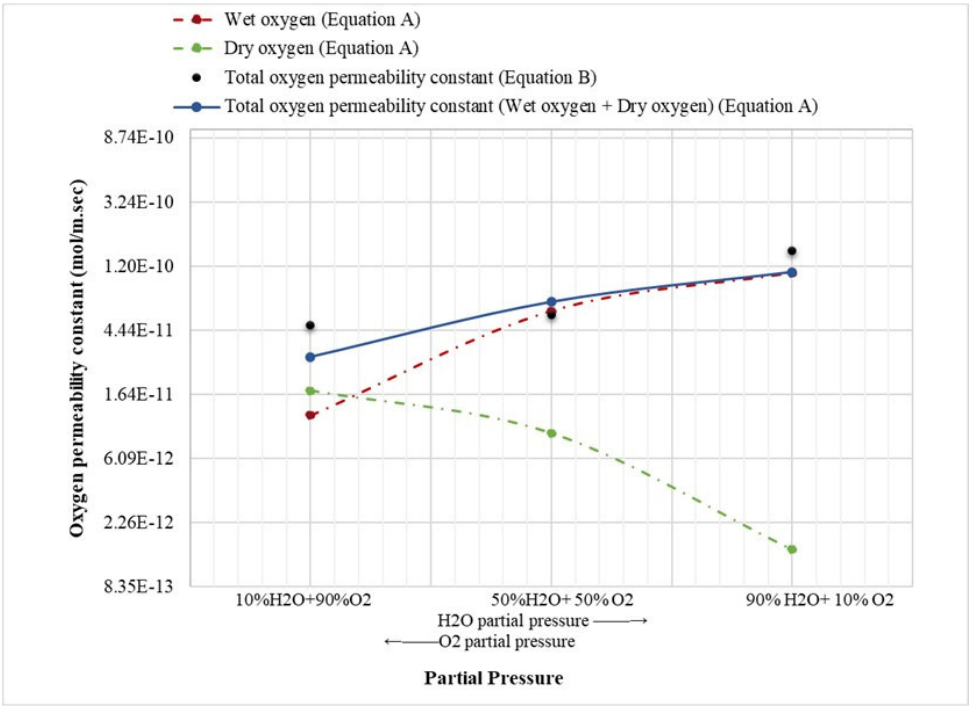

Figure 4-9: Top coat oxygen permeability constant as a function of the environment at 1523K after 200 hr exposure time.

For comparison, Figure 4-10 shows the oxygen permeability constants through TGO and TC as a function of partial pressures of both oxygen and water vapour. The much faster oxygen permeation through TC as compared to TGO can again be seen.

Table *4-16* contains the individual values of the parabolic rate constant (kp) [67] and calculated TGO oxygen permeability constant.

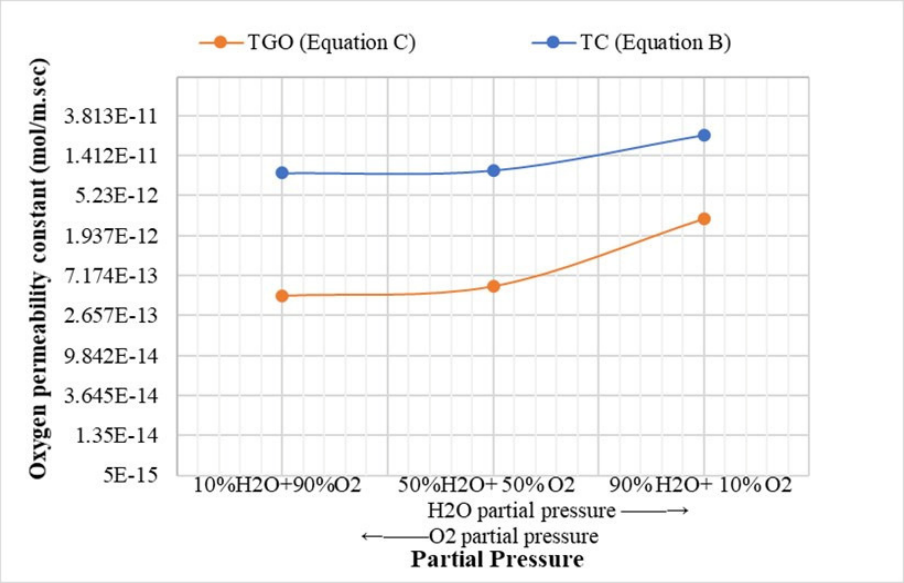

Figure 4-10: TGO and TC oxygen permeability constants for the three investigated partial pressure conditions at 1523 K.

Table 4-16: Parabolic rate constant [66] and oxygen permeability constant of TGO as a function of the environment.

Wet environment	**Oxygen permeability constant, TGO (mol/m. sec)**	**Parabolic rate constant, k_p (µm²/hr)**
10%H_2O+90%O_2	$4.33*10^{-13}$	0.0425
50%H_2O+50% O_2	$5.49*10^{-13}$	0.0539

90%H_2O+10% O_2	$2.94*10^{-12}$	0.289

* exposed for 200 hours at constant 1523K.

4.2.4 Effect of Modifiers

Modifiers are known to potentially alter the oxygen permeability. Therefore, the addition of modifiers to the YbDS top coat is studied. The investigation is limited to wet environments at 1589 K, for which existing literature data allow validations. Specifically, Lee [36] recorded the change in TGO thickness for 100 hr and 1000 hr exposure time. For this analysis, Equation B is used to calculate the oxygen permeability constant through the TC using the TGO thickness data from Table 4-1. For comparison, the oxygen permeability constant of TGO is also calculated by Equation C for the same temperature and environmental conditions. The results are summarized in Figure 4-11 for 1000 hrs exposure.

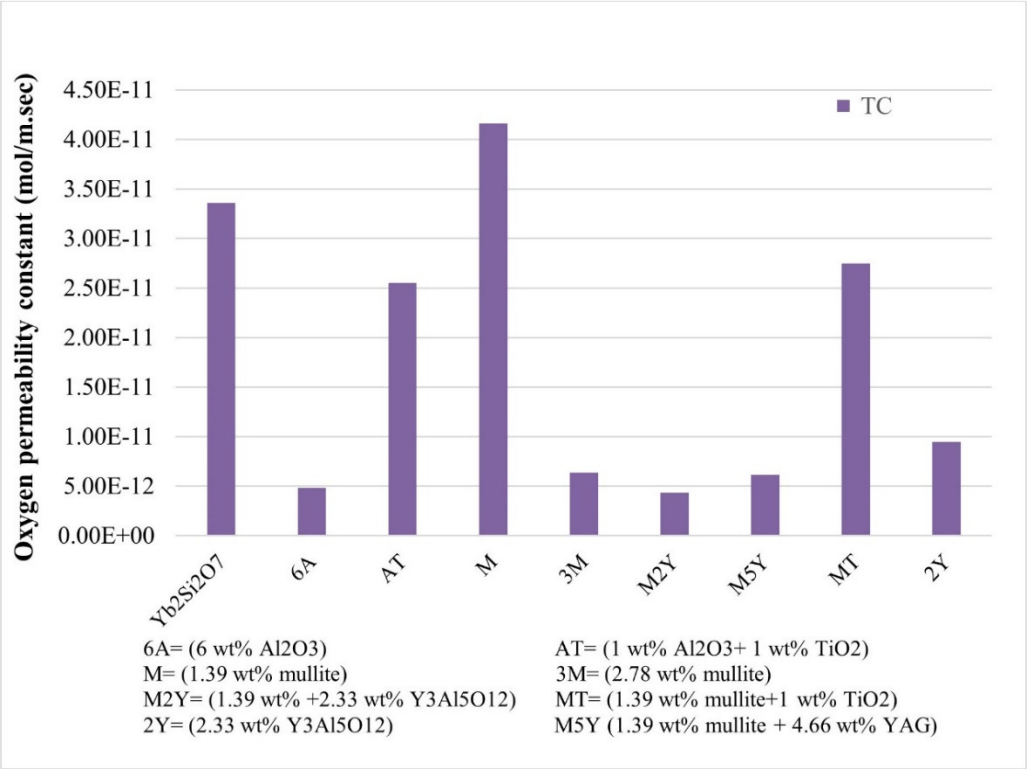

Figure 4-11: Comparative oxygen permeability constant values of TC without modifiers ($Yb_2Si_2O_7$) and with modifiers in wet oxygen condition (90% H_2O + 10% O_2) after 1000 hr exposure time.

Figure 4-11 indicates an increase in oxygen permeability constant with the M modifier, while reduced permeability is achieved with all other investigated modifiers. Moreover, the reduction in oxygen permeability constant is strongest with the 6A, M2Y, 3M, 2Y, M5Y modifiers, while it is only moderate with the AT and MT modifiers.

For comparison, Figure 4-12 shows the estimated oxygen permeability constants for the TGO layer as calculated by the proposed Equation C with the kp values taken from Table 4-2. In agreement with the results presented so far, Table 4-12 shows low ratios of TGO-to-TC oxygen permeability constants, confirming the much faster permeation through the top coat as compared to the TGO irrespective of the modifier type.

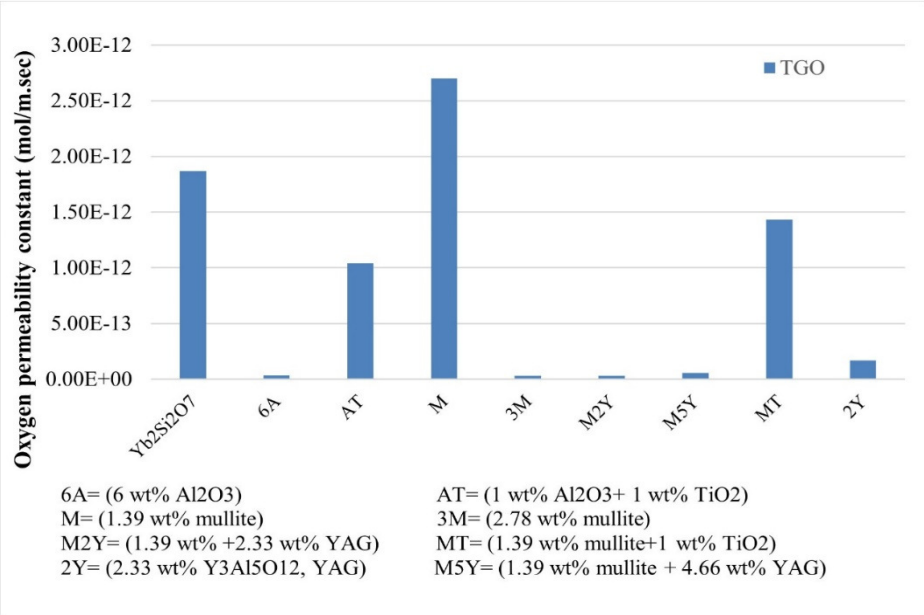

Figure 4-12: Comparative oxygen permeability constant values of TGO without modified top coat ($Yb_2Si_2O_7$) and with modified top coat (6A, AT, M, 3M, M2Y, M5Y, MT, 2Y) in wet environment (90% H_2O + 10% O_2) after 1000 hr exposure time.

Table 4-17: Ratio of TGO-to-TC oxygen permeability constants.

Top coat	**Ratio ($\frac{TGO}{TC}$)**
$Yb_2Si_2O_7$	0.0560
6A	0.0074
AT	0.0407
M	0.0650
3M	0.0047
M2Y	0.0074
M5Y	0.0088
MT	0.0520
2Y	0.0178

5 Discussion

The oxygen permeability constant (*P.l*) of TC and TGO is known to provide considerable insight into the permeability of oxidants through the EBC system. Investigations so far have primarily studied oxygen and water vapor as separate environments. In this study, we expand this knowledge by quantitatively investigating both dry and wet oxygen conditions, demonstrating the substantial acceleration of permeation by water vapor. Moreover, the study suggests that closed non-connected pores have limited impact on the oxidant permeability of the top coat, in contrast to open pores, interconnected pores, and through thickness cracks. Also, the results indicate that the TGO hinders the oxidant permeation much stronger than the TC in both the dry and wet oxygen conditions, suggesting that it is the diffusion rate controlling layer. This is in-line with the findings of Sullivan [67] whose model suggested 67 times faster permeability of oxygen in TC compared to TGO. The results are also in agreement with the work of Deal and Grove for both TC and TGO, although the values calculated in this study are an order of magnitude higher for the water vapor environment as seen earlier in Table 4-10. Finally, the estimations yield a negative oxygen permeability constant in the case of defect reaction with proton between water vapour and YbDS (TC), which means the oxidant flux would take place in the direction opposite to the partial pressure gradient in the absence of external driving forces. This is contrary to literature reports and fundamental diffusion laws. As such, this study suggests that the defect reaction in the EBC system is without proton instead.

As discussed earlier in section 2.1.4, the higher the Si-O bond population, the higher the stability of rare-earth silicates in water vapor environments. This is primarily due to the high strength of the Si-O bond that makes it difficult to break, reducing the mobility and permeation of oxygen ions. In this study, the TGO is found to have a higher Si-O bond population compared to the TC, which may explain the slower oxidant permeation through TGO compared to TC.

In general, a parabolic rate behavior hints to diffusion controlled oxidation kinetics for TGO growth, whereas a linear rate behavior indicates interface controlled kinetics [77]. In this aspect, the current study suggests a parabolic rate of TGO growth and indicates that the oxidant permeation through TGO is the TGO growth rate controlling step. Richards et al. [29] also reported that the oxidant permeation through TC is lower than through TGO. However, they experimentally demonstrated a linear growth rate for the TGO layer.

In dry oxygen conditions, the species for the oxidation of silicon-based materials can be molecular, ionic, or atomic oxygen [78]–[80]. Molecular permeation as O_2 through SiO_2 is directly proportional to the oxygen partial pressure [81]. It was reported across amorphous silica via open spaces at relatively low temperatures. The open spaces represent channels, through which the oxygen molecules permeate inertly, which means without ion exchange with the TGO ions Si^{+4} and O^{-2}. In contrast, the permeation of oxygen ion is considerable at high temperatures where interaction with TGO network oxygen is possible. Network oxygen is the bridging oxygen in the SiO_2 system and oxygen ions permeate either via vacancy or interstitially [78] [82]. As such, the oxygen ion transportation mechanism involves the breaking and reforming of Si-O bonds. Thus, the activation energy for oxygen ion permeation can be expected to be high

compared to that for molecular oxygen permeation, making it only possible at higher temperatures. From literature, the activation energies range from 80 to 120 kJ/mol [66] [83] for molecular oxygen diffusion, and from 200 to 460 kJ/mol for ionic oxygen diffusion [66] [84].

In this study, we assumed that the formation of TGO takes place at the TGO/bond coat interface. Thus, oxidants have to permeate through both TC and TGO layers to reach the TGO/bond coat interface where silicon dioxide (TGO) forms. The total permeability through the TC is assumed to be due to oxygen ion and ytterbium ion together, while the TGO oxidants are assumed to be molecular O_2 alone. The considered oxidation mechanism is as follows: (1) oxygen dissociates at the gas/TC interface; (2) the formed oxygen ions diffuse through the TC to reach at the TC/TGO interface; (3) the oxygen ions re-associate into molecular oxygen; (4) molecular oxygen diffuses through the TGO to be delivered at the TGO/bond coat interface; (5) molecular oxygen reacts with Si to form the SiO_2 TGO.

In this study, molecular oxygen would only be necessary for TGO formation and growth at the TGO/bond coat interface, while assuming oxygen ion diffusion permeating through the TGO allows the consideration of TGO formation at either the TC/TGO or the TGO/bond interfaces. However, oxygen ion diffusion may require parallel accompanying silicon ion diffusion in the opposite direction to maintain space charge neutrality. If Si ion diffusion is dominant, the TC/TGO interface would be the favourable location for TGO formation. Otherwise, TGO would form at the TGO/bond coat interface. The activation energy for Si ion diffusion in silicon dioxide is 457 kJ/mol [84], which is close to the Si-O bond energy of 434 kJ/mol [78]. Like in the top coat, Si ion mass transfer through the TGO would necessitate cation and oxygen ion mass

transfer in opposite directions. This is similar to literature reports on the mass transfer mechanism through the TGO layer in the TBC system, where aluminum ions and oxygen ions contribute to alumina TGO formation at both the top coat/TGO and the TGO/bond coat interfaces. For TBCs, the reported activation energies for oxygen ions and aluminum ions are 467 kJ/mol and 604 kJ/mol, respectively. Here too, the dominant diffusing species depends on the oxygen partial pressure gradient or the chemical potentials [57]. As such, similar mass transportation processes can be expected in EBC systems, although no experimental confirmation of the EBC TGO growth kinetics can be found in existing literature so far.

Extending to the effect of water vapor, the permeability of oxygen through TC is also much faster than through TGO. The current results suggest activation energies of 288.35 kJ/mol and 619.2 kJ/mol for oxygen ion and ytterbium ion diffusion through the TC in wet environments, respectively. Comparing these values with those in dry oxygen environment of 420 kJ/mol and 388 kJ/mol, respectively, it can be seen that the activation energy for oxygen ion permeation is lower, while the activation energy for ytterbium ions is higher in wet environment. This may explain the strong acceleration in permeability of oxygen in the presence of water vapour as compared to the dry oxygen environment. It also rationalises the earlier observation of mass transport through the top coat primarily by oxygen ion.

The permeability of oxygen slows down over time as shown in Table 4-11 and Table 4-12 irrespective of whether the EBC system is in dry or wet environment. In elemental or molecular mass transfer with no electric charge, this phenomenon is generally caused by a reduction in concentration gradient as the permeating species flow from high to low partial pressure interfaces. In the case of ion diffusion, an additional factor is

possible attraction or repulsion due to space charges, as negatively charged oxygen ions diffuse away from the gas/TC interface, leaving positively charged holes behind. The same applies to the outward movement of positively charged ytterbium ions that leaves behind negatively charged vacancies. As such, both negative and positive charges co-exist within the oxide layer but on the opposite interfaces. As the space charges accumulate over time, positive and negative space charges can reduce the mass transfer of ytterbium ions and oxygen ions, respectively.

In wet environments, the results of the current study suggest the following oxidation mechanism without protons: (1) water molecules dissociate into oxygen and hydrogen molecules; (2) the oxygen molecules interact with existing defects, such as Schottky defects, in the YbDS top coat. The hydrogen molecules can either dissociate at the surface without being directly involved in the defect reaction, or they could take part in the defect reaction. If we assume that the hydrogen molecules get adsorbed as protons into the gas/TC interface due to high surface energy, then the adsorbed protons would induce positive charges at the gas/TC interface, with a parallel creation of negative charges at the TC/TGO interface for electroneutrality. This means, opposite space charges would spontaneously develop at the inner interfaces [85]. The resulting forward bias between the inner space charge could then increase the cation or anion migration, reducing the activation energy for oxygen ion diffusion as observed in this study. However, in the case of defect reactions with proton, positively charged $2OH_O^{\bullet}$ ions would be created that generally locate at interstitial sites in the YbDS top coat lattice. These positively charged protons would be accommodated within the electron cloud of oxygen ions, which would restrict their free movement, necessitating the higher activation energy for their diffusion as also observed in this study. Finally, in cases

where the outward movement of ytterbium ions is dominant in the total oxygen permeability through TC, the YbDS near the TGO interface would eventually become deficient in ytterbium ions, increasing the relative prevalence of Si-O bonds. This would possibly make the TGO thickness larger than would be expected from TGO formation due to the oxidation of the bond coat alone.

The results of this study suggest that modifiers added to the TC reduce its permeability of oxygen, except for the TC modified with 1.39wt% of mullite. As the study suggests oxygen ion diffusion as dominant for mass transfer in wet environments, it can be concluded that the modifiers effectively hinder oxygen ion permeation. This hindrance proves to be strongly composition sensitive. For instance, 1.39wt % mullite addition causes an increase in TC oxygen permeability whereas 3wt% mullite addition achieves a strong drop in permeability as compared to YbDS without modifiers. Furthermore, titania seems to counter the effect of other individual modifiers. For example, 1wt% of alumina with 1wt% of titania as modifier resulted in higher oxygen permeation through TC as compared to the addition of 6wt% alumina alone. As another example, while 1wt% mullite addition increased the oxygen permeation, together with 1wt% titania, it achieves a drop in TC oxygen permeation. Overall, the results suggest that as the content of individual modifiers increases, their capacity to reduce oxygen permeation also increases. However, the combination of multiple modifiers seems to have a counterproductive result. The exception is yttrium alumina garnet (Y) that seems to be an effective dopant to hinder oxidant permeation irrespective of percent addition and combination with other modifiers. This is in agreement with the results of Matsudaira et al. [86] who studied the effect of yttrium alumina garnet doping on the permeability of oxygen in alumina. Their work concluded that yttrium effectively suppresses oxygen

mobility, but had no effect on aluminum ion mobility. A similar trend was observed for the permeability of oxygen through TGO.

6 Conclusions

The focus of the thesis is to investigate the oxidation mechanisms and the factors affecting the permeability through the EBC system. The following conclusions can be drawn:

1) Three equations A, B, and C are proven to efficiently estimate the oxygen permeability constant. Equation A for TC is taken from literature and is successfully modified in this study to include the water vapor effect. Equation B is taken from literature as well and is successfully used to estimate the total permeability of oxygen through TC based on the change in TGO volume per unit time. Equation C is newly derived in this work and estimates the oxygen permeability constant of TGO with considerable accuracy.
2) The porosity of the YbDS (TC) is measured to be below 7% and is found to decrease at high temperature, which indicates some sintering as the exposure time increases. This level of close pore concentration seems not to considerably affect oxygen permeation in contrast to through thickness cracks and open pores that are reported in the literature to play a big role.
3) The study provides evidence that the TGO effectively hinders oxidant permeation and seems to be the diffusion rate controlling layer in the EBC system. This can be rationalized by the higher Si-O bond population in the TGO as compared to the YbDS top coat.
4) The presence of water vapor strongly accelerates the permeation of oxidants through TC by almost factor 2.5 compared to permeation in dry oxygen. This seems to be related to the capacity of water vapor to lower the activation energy for oxidant diffusion.

5) The total oxygen permeability constant from both dry oxygen and added water vapor increases with increasing temperature, partial pressure gradient and water vapor content, with the latter playing the dominant role.
6) The effect of top coat oxide modifiers on oxygen permeation is composition sensitive and seems to also be related to their interaction with oxygen ions and their mobility.

7 Future Work

The approach used in this work can be implemented to model and quantify the permeation of oxidants through the individual EBC system layers considering the active defect reactions for TC and the parabolic rate constant for TGO. However, the study has a number of limitations that could be addressed in subsequent studies. They include:

- The current investigation is limited to permeation through top coat and TGO. Expanding the approach to tri-layer EBC systems could provide more insight into the mechanisms of oxidant diffusion and its impact on the oxidation of EBCs and their failures.
- The current study assumes that only Yb^{3+} and O^{2-} ions participate in the total diffusion through the YbDS TC. However, the activation energies for Yb^{3+} and Si^{4+} cations are comparable. The possibly that Si^{4+} also contributes to the cation mass transfer could be investigated. Moreover, it may be important to consider the mass transfer of both anion and cation in opposite direction.
- The defect interactions in TC are assumed to be solely dependent on the Schottky defects. Including other possibilities like Frenkel defects or the combination of both defects could provide more accurate results.
- Also, the study is limited to closed pores that prove to have no considerable impact on oxidant diffusion. Investigating the potentially stronger effects of interconnected pores, microcracks and through thickness cracks could provide a better estimate of the impact of coating defects in both the TC or TGO.

- The modified exponent for the TC Equation A does not consider defect pairs such as hydroxide and oxygen ions at interstitial positions. As such, there is room for further improvements.
- The proposed TGO equation is limited to the parabolic growth mechanism. The linear growth has previously been reported in the literature for some systems and environments. Therefore, it could be investigated as an alternative to the current work.
- Literature data used in this study are limited and do not allow a comprehensive investigation of the top coat dopant impact. Therefore, to understand how dopants individually affect the anion or cation diffusion activation energies, it is necessary to perform more experimental tests at different temperatures, partial pressures, exposure time, and for more dopant types.

References

[1] B. T. Richards and H. N. G. Wadley, “Plasma spray deposition of tri-layer environmental barrier coatings,” J. Eur. Ceram. Soc., vol. 34, pp. 3069–3083, 2014.

[2] J. T. DeMasi-Marcin and D. K. Gupta, “Protective coatings in the gas turbine engine,” Surf. Coatings Technol., vol. 68–69, pp. 1–9, 1994.

[3] M. Belmonte, “Advanced ceramic materials for high temperature applications,” Adv. Eng. Mater., vol. 8 , pp. 693–703, 2006.

[4] B. T. Richards, “Ytterbium Silicate Environmental Barrier Coatings,” Ph.D dissertation, University of Virginia, 2015.

[5] H. Kaya, “The application of ceramic-matrix composites to the automotive ceramic gas turbine,” Compos. Sci. Technol., vol. 59, pp. 861–872, 1999.

[6] H. F. Chen, C. Zhang, Y. C. Liu, P. Song, W.X. Li, G. Yang and B. Liu, “Recent progress in thermal/environmental barrier coatings and their corrosion resistance,” Rare Met., vol. 39, pp. 498–512, 2020.

[7] B. Gleeson, “Thermal Barrier Coatings for Aeroengine Applications Thermal Barrier Coatings for Aeroengine Applications,” J. Propuls. Power, vol. 22, pp. 375–383, 2016.

[8] K. N. Lee, “Special issue: Environmental barrier coatings,” Coatings, vol. 10, pp. 1–4, 2020.

[9] J. Xu, V. K. Sarin, S. Dixit, and S. N. Basu, “Stability of interfaces in hybrid

EBC/TBC coatings for Si-based ceramics in corrosive environments," Int. J. Refract. Met. Hard Mater., vol. 49, pp. 339–349, 2015.

[10] S. Schmidt, S. Beyer, H. Knabe, H. Immich, R. Meistring, and A. Gessler, "Advanced ceramic matrix composite materials for current and future propulsion technology applications," Acta Astronaut., vol. 55, pp. 409–420, 2004.

[11] N. Al Nasiri, N. Patra, M. Pezoldt, J. Colas, and W. E. Lee, "Investigation of a single-layer EBC deposited on SiC/SiC CMCs: Processing and corrosion behaviour in high-temperature steam," J. Eur. Ceram. Soc., vol. 39, pp. 2703–2711, 2019.

[12] N. P. Padture, "Environmental degradation of high-temperature protective coatings for ceramic-matrix composites in gas-turbine engines," npj Mater. Degrad., vol. 3, art. no. 11, 2019.

[13] B. Lv, X. Jin, J. Cao, B. Xu, Y. Wang, and D. Fang, "Advances in numerical modeling of environmental barrier coating systems for gas turbines," J. Eur. Ceram. Soc., vol. 40, pp. 3363–3379, 2020.

[14] K. N. Lee, "Environmental Barrier Coatings for SiC_f / SiC," in Ceramic Matrix Composites: Materials, Modeling and Technology, Indianapolis, IN, USA: John Wiley & Sons, Inc, pp. 430–451, 2014.

[15] Y. Xu, X. Hu, F. Xu, and K. Li, "Rare earth silicate environmental barrier coatings: Present status and prospective," Ceram. Int., vol. 43, pp. 5847–5855, 2017.

[16] K. N. Lee, D. S. Fox, and N. P. Bansal, "Rare earth silicate environmental barrier

coatings for SiC/SiC composites and Si_3N_4 ceramics," J. Eur. Ceram. Soc., vol. 25, pp. 1705–1715, 2005.

[17] H. Klemm, K. Schönfeld, and W. Kunz, "Delayed Formation of Thermally Grown Oxide in Ceramic Matrix Composites," Coatings, vol. 4, pp. 1–11, 2020.

[18] D. W.Richerson, "Ceramics and Components in Energy Conversion Systems," in 28th International Conference on Advanced Ceramics and Composites A: Ceramic Engineering and Science Proceedings, Salt Lake City, Utah, vol. 25, pp. 3–32, 2004.

[19] A. Chamberlain and J. Lane, "SiC / SiC Ceramic Matrix Composites – A Turbine Engine Perspective," in Engineering Conferences International: Ultra-high Temperature Ceramics Materials for Extreme Environment Applications II Proceedings,Hernstein, Asutria, 2013.

[20] E. J. Opila, and R. E. Hann, "Paralinear oxidation of CVD SiC in water vapor," J. Am. Ceram. Soc., vol. 80, pp. 197–205, 1997.

[21] N. S. Jacobson, "Corrosion of Silicon-Based Ceramics in Combustion Environments," J. Am. Ceram. Soc., vol. 76, pp. 3–28, 1993.

[22] K. L. More, P. F. Tortorelli, L. R. Walker, J. B. Kimmel, N. Miriyala, J. R. Price, H. E. Eaton, E. Y. Sun, and G. D. Linsey , "Evaluating environmental barrier coatings on ceramic matrix composites after engine and laboratory exposures," Am. Soc. Mech. Eng. Int. Gas Turbine Institute, Turbo Expo IGTI, vol. 4 A, pp. 155–162, 2002.

[23] K. N. Lee, D. S. Fox, J. I. Eldridge, D. Zhu, R. C. Robinson, N. P. Bansal, and

R. A. Miller, “Upper temperature limit of environmental barrier coatings based on mullite and BSAS,” J. Am. Ceram. Soc., vol. 86, pp. 1299–1306, 2003.

[24] K. N. Lee, R. A. Miller, and N. S. Jacobson, “New Generation of Plasma-Sprayed Mullite Coatings on Silicon Carbide,” J. Chem. Inf. Model., vol. 53, pp. 1689–1699, 2013.

[25] K. N. Lee, “Current status of environmental barrier coatings for Si-based ceramics,” Surf. Coatings Technol., vol. 133–134, pp. 1–7, 2000.

[26] G. C. C. Costa, and N. S. Jacobson, “Mass spectrometric measurements of the silica activity in the Yb2O3-SiO2 system and implications to assess the degradation of silicate-based coatings in combustion environments,” J. Eur. Ceram. Soc., vol. 35, pp. 4259–4267, 2015.

[27] J. Felsche, “The crystal chemistry of the rare-earth silicates,” in Structure and Bonding, Zürich, Switzerland, vol. 13 pp. 99–197, 1973.

[28] D. Zhu, and Robert A. Miller, “Barrier and Coatings Diesel for Advanced Engines Gas Turbine,” Cleveland, Ohio 44135, US, 1999.

[29] B. T. Richards, K. A. Young, F. De Francqueville, S. Sehr, M. R. Begley, and H. N. G. Wadley, “Response of ytterbium disilicate-silicon environmental barrier coatings to thermal cycling in water vapor,” Acta Mater., vol. 106, pp. 1–14, 2016.

[30] D. Zhu, and R. A. Miller, “Thermal and environmental barrier coatings for advanced propulsion engine systems,” Annu. Forum Proc. - Am. Helicopter Soc., vol. 1 , pp. 703–709, 2004.

[31] A. Abdul-Aziz, “Durability modeling review of thermal- and environmental-barrier-coated fiber-reinforced ceramic matrix composites part I,” Materials (Basel)., vol. 10, 2018.

[32] E. Bakan, D. Marcano, D. Zhou, Y. J. Sohn, G. Mauer, and R. Vaßen, “$Yb_2Si_2O_7$ Environmental Barrier Coatings Deposited by Various Thermal Spray Techniques: A Preliminary Comparative Study,” J. Therm. Spray Technol., vol. 26, pp. 1011–1024, 2017.

[33] Y. Lu, Y. Cao, and X. Zhao, “Optimal rare-earth disilicates as top coat in multilayer environmental barrier coatings,” J. Alloys Compd., vol. 769, pp. 1026–1033,2018.

[34] K. N. Lee, J. I. Eldridge, and R. C. Robinson, “Residual stresses and their effects on the durability of environmental barrier coatings for SiC ceramics,” J. Am. Ceram. Soc., vol. 88, pp. 3483–3488, 2005.

[35] B. J. Harder, J. Ramírez-Rico, J. D. Almer, K. N. Lee, and K. T. Faber, “Chemical and mechanical consequences of environmental barrier coating exposure to calcium-magnesium-aluminosilicate,” J. Am. Ceram. Soc., vol. 94, pp. s178–s185, 2011.

[36] K. N. Lee, “$Yb_2Si_2O_7$ Environmental barrier coatings with reduced bond coat oxidation rates via chemical modifications for long life,” J. Am. Ceram. Soc., vol. 102, pp. 1507–1521, 2019.

[37] E. Opila, R. Golden, C. Parker, and M. Ridley, “Microstuctural Evolution of Environmental Barrier Coatings in High-Temperature Steam,” in Engineering Conferences International, vol. 2, pp. 1–4, , 2017.

[38] Y. Wang, and J. Liu, "First-principles investigation on the corrosion resistance of rare earth disilicates in water vapor," J. Eur. Ceram. Soc., vol. 29, pp. 2163–2167, 2009.

[39] N. Maier, K. G. Nickel, and G. Rixecker, "High temperature water vapour corrosion of rare earth disilicates $(Y,Yb,Lu)_2Si_2O_7$ in the presence of $Al(OH)_3$ impurities," J. Eur. Ceram. Soc., vol. 27, pp. 2705–2713, 2007.

[40] H. Klemm, "Silicon nitride for high-temperature applications," J. Am. Ceram. Soc., vol. 93, pp. 1501–1522, 2010.

[41] A. Abdul-Aziz, F. Abdi, R. T. Bhatt, and J. E. Grady, "Durability Modeling of Environmental Barrier Coating (EBC) Using Finite Element Based Progressive Failure Analysis," J. Ceram., vol. 2014, article id 874034, 2014.

[42] L. Łatka, "Thermal Barrier Coatings Manufactured by Suspension Plasma Spraying - A Review," Adv. Mater. Sci., vol. 18, pp. 95–117, 2018.

[43] R. E. Smallman, and A. H. W. Ngan, "Point Defect Behaviour," in Modern Physical Metallurgy, 8th ed., Elsevier, pp. 251–285, 2014.

[44] R. J. D. Tilley, "Nonstoichiometry and Extrinsic Electronic Conductivity," in Defects in Solids, John Wiley & Sons, Inc, pp. 351–398, 2008.

[45] W. Zhao, "Steam Effect on Oxidation Behavior of Alumina-Scale Forming Nickel-Based Alloys and A Kinetics Analysis of Complex Scale Evolution During Isothermal Oxidation," Ph.D dissertation, University of Pittsburgh, 2012.

[46] H. L. Tuller, and S. R. Bishop, "Point Defects in Oxides: Tailoring Materials Through Defect Engineering," Annu. Rev. Mater. Res., vol. 41, pp. 369–398,

2011.

[47] D. M. Smyth, “Defect Equilibria in Perovskite Oxides,” in Geophysical Monograph Series, Materials Research Centre, Lehigh University, vol. 45, pp. 2127–2130, 1989.

[48] I. G. Wright, and R. B. Dooley, “A review of the oxidation behaviour of structural alloys in steam,” Int. Mater. Rev., vol. 55, pp. 129–167, 2010.

[49] T. Norby, M. Widerøe, R. Glöckner, and Y. Larring, “Hydrogen in oxides,” Dalt. Trans., no. 19, pp. 3012–3018, 2004.

[50] T. Norby, and Y. Larring, “Concentration and transport of protons in oxides,” Elsevier, vol. 2, pp. 593–599, 1997.

[51] C. G. Zhou, and Y. X. Song, “Oxidation and hot corrosion of thermal barrier coatings (TBCs),” Therm. Barrier Coatings, Metals and Surface Engineering, pp. 193–214, 2011.

[52] A. Atkinson, “Wagner theory and short circuit diffusion,” Mater. Sci. Technol. (United Kingdom), vol. 4, pp. 1046–1051, 1988.

[53] R. E. Smallman, and A. H. W. Ngan, “Oxidation, Corrosion and Surface Engineering,” Mod. Phys. Metall., pp. 617–657, 2014.

[54] R. A. Rapp, “The high temperature oxidation of metals forming cation-diffusing scales,” Metall. Trans. B, vol. 15, pp. 195–212, 1984.

[55] D. J. Young, “High Temperature Oxidation and Corrosion of Metals, ” 2nd ed. New South Wales, Sydney: Elsevier Ltd, 2016.

[56] S. Kitaoka, T. Matsudaira, and M. Wada, “Mass-transfer mechanism of alumina ceramics under oxygen potential gradients at high temperatures,” Mater. Trans., vol. 50, pp. 1023–1031, 2009.

[57] M. Wada, T. Matsudaira, and S. Kitaoka, “Mutual grain-boundary transport of aluminum and oxygen in polycrystalline Al_2O_3 under oxygen potential gradients at high temperatures,” J. Ceram. Soc. Japan, vol. 119, pp. 832–839, 2011.

[58] M. Wada, T. Matsudaira, N. Kawashima, S. Kitaoka, and M. Takata, “Mass transfer in polycrystalline ytterbium disilicate under oxygen potential gradients at high temperatures,” Acta Mater., vol. 135, pp. 372–381, 2017.

[59] S. Kitaoka, T. Matsudaira, M. Wada, N. Kawashima, D. Yokoe, and M. Takata, “Mass transfer in Yb silicate environmental barrier coatings at high temperatures,” Mater. Sci. Forum, vol. 941, pp. 1898–1903, 2018.

[60] D. H. Olson, J. T. Gaskins, J. A. Tomko, E. J. Opila, R. A. Golden, G. J. K. Harrington, A. L. Chamberlain, and P. E. Hopkins , “Local thermal conductivity measurements to determine the fraction of α-cristobalite in thermally grown oxides for aerospace applications,” Scr. Mater., vol. 177, pp. 214–217, 2020.

[61] R. Anton, N. Laska, U. Schulz, S. Obert, and M. Heilmaier, “Magnetron Sputtered Silicon Coatings as Oxidation Protection for Mo-Based Alloys,” Adv. Eng. Mater., vol. 2000218, pp. 1–8, 2020.

[62] E. J. Opila, “Water Effects on Silica-Forming Ceramics,” Cleveland, OH 44115, 2000.

[63] N. Birks, G. H. Meier, and F. S. Pettit, “Introduction to the High Temperature

Oxidation of Metals, ” 2nd ed. Cambridge: Cambridge University Press, 2006.

[64] J. Roy, S. Chandra, S. Das, and S. Maitra, “Oxidation behaviour of silicon carbide - A review,” Rev. Adv. Mater. Sci., vol. 38, pp. 29–39, 2014.

[65] Z. Zheng, “Oxidation of Single-Crystal Silicon Carbide,” J. Electrochem. Soc., vol. 137, p. 2812, 1990.

[66] Y. Lu, and Y. Wang, “Formation and growth of silica layer beneath environmental barrier coatings under water-vapor environment,” J. Alloys Compd., vol. 739, pp. 817–826, 2018.

[67] R. M. Sullivan, “Reformulation of oxide growth equations for oxidation of silicon bond coat in environmental barrier coating systems,” J. Eur. Ceram. Soc., vol. 39, pp. 5403–5409, 2019.

[68] D. Calvert, and F. J. Norton, “Permeation of Gaseous Oxygen through Vitreous Silica,” p. 4789, 1961.

[69] E. L. Courtright, J. T. Prater, C. H. Henager, and E. N. Greenwell, “Oxygen Permeability for Selected Ceramic Oxides in the Range 1200°C -1700°C,” Tech. Rep., vol. WL-TR-91-4, 1991.

[70] O. Yuzur, K. Masayuki, M. Tatsuo, N. Akira, and T. Sekigawa, “Oxygen Permeability of Y2SiO5,” Mater. Trans., vol. 42,, pp. 1124–1130, 2001.

[71] S. Kitaoka, T. Matsudaira, D. Yokoe, T. Kato, and M. Takata, “Oxygen permeation mechanism in polycrystalline mullite at high temperatures,” J. Am. Ceram. Soc., vol. 100, pp. 3217–3226, 2017.

[72] S. Kitaoka, T. Matsudaira, N. Kawashima, D. Yokoe, T. Kato, and M. Takata, “Mass transfer mechanism in mullite under oxygen potential gradients at high temperatures,” Ceram. Eng. Sci. Proc., vol. 37, pp. 261–270, 2017.

[73] B. E. Deal and A. S. Grove, “General relationship for the thermal oxidation of silicon,” J. Appl. Phys., vol. 36, pp. 3770–3778, 1965.

[74] T. Matsudaira, S. Kitaoka, N. Shibata, T. Nakagawa, and Y. Ikuhara, “Mass transfer through a single grain boundary in alumina bicrystals under oxygen potential gradients,” J. Mater. Sci., vol. 46, pp. 4407–4412, 2011.

[75] C. W. Bale, E. Bélisle, P. Chartrand, S. A. Decterov, G. Eriksson, K. Hack, I. H. Jung, Y. B. Kang, J. Melançon, A. D. Pelton, C. Robelin, and S. Petersen, “FactSage thermochemical software and databases - recent developments,” Calphad Comput. Coupling Phase Diagrams Thermochem., vol. 33, pp. 295–311, 2009.

[76] X. Zhong, Y. Niu, H. Li, Y. Zeng, X. Zheng, C. Ding, and J. Sun, “Microstructure evolution and thermomechanical properties of plasma-sprayed Yb2SiO5 coating during thermal aging,” J. Am. Ceram. Soc., vol. 100, pp. 1896–1906, 2017.

[77] T. Narushima, T. Goto, and T. Hirai, “High-Temperature Oxidation of Chemically Vapor-Deposited Silicon Carbide in Wet Oxygen at 4823 to 4923 K,” J. Am. Ceram.Soc., vol. 84, pp. 3580–3584, 1990.

[78] M. A. Lamkin, F. L. Riley, and R. J. Fordham, “Oxygen mobility in silicon dioxide and silicate glasses: a review,” J. Eur. Ceram. Soc., vol. 10, pp. 347–367, 1992.

[79] T. Goto, H. Homma, and T. Hirai, “Effect of oxygen partial pressure on the high-temperature oxidation of CVD SiC,” Corros. Sci., vol. 44, pp. 359–370, 2002.

[80] L. Luo, Y. Wang, L. Liu, L. Duan, G. Wang, and Y. Lu, “Ablation behavior of C/SiC composites in plasma wind tunnel,” Carbon N. Y., vol. 103, pp. 73–83, 2016.

[81] J.Rodriguez-Viejo, F.Sibieude, and M. T. Clavaguera-Mora, “High-Temperature Oxidation of CVD-SiC Part II . Relation between Oxygen Diffusion Coefficients and Parabolic Rate Constants,” J. Eur. Ceram.Sic, vol. 13, pp. 177–184, 1993.

[82] C. E. Ramberg, and W. L. Worrell, “Oxygen Transport in Silica at High Temperatures: Implications of Oxidation Kinetics,” J. Am. Ceram. Soc., vol. 84, pp. 2607–2616, 2001.

[83] R. L. MEEK, “Diffusion Coefficient for Oxygen in Vitreous SiO2,” J. Am. Ceram. Soc., vol. 56, pp. 341–342, 1973.

[84] D. Tsoukalas, C. Tsamis, and P. Normand, “Diffusivity measurements of silicon in silicon dioxide layers using isotopically pure material,” J. Appl. Phys., vol. 89, pp. 7809–7813, 2001.

[85] T. Matsudaira, S. Kitaoka, N. Shibata, Y. Ikuhara, M. Takeuchi, and T. Ogawa, “Effects of an oxygen potential gradient and water vapor on mass transfer in polycrystalline alumina at high temperatures,” Acta Mater., vol. 151, pp. 21–30, 2018.

[86] T. Matsudaira, M. Wada, and S. Kitaoka, “Effect of dopants on the distribution of aluminum and oxygen fluxes in polycrystalline alumina under oxygen

potential gradients at high temperatures," J. Am. Ceram. Soc., vol. 96, pp. 3243–3251, 2013.

Appendix:

FactSage Steps:

Step 1: Insert the system to be studied:

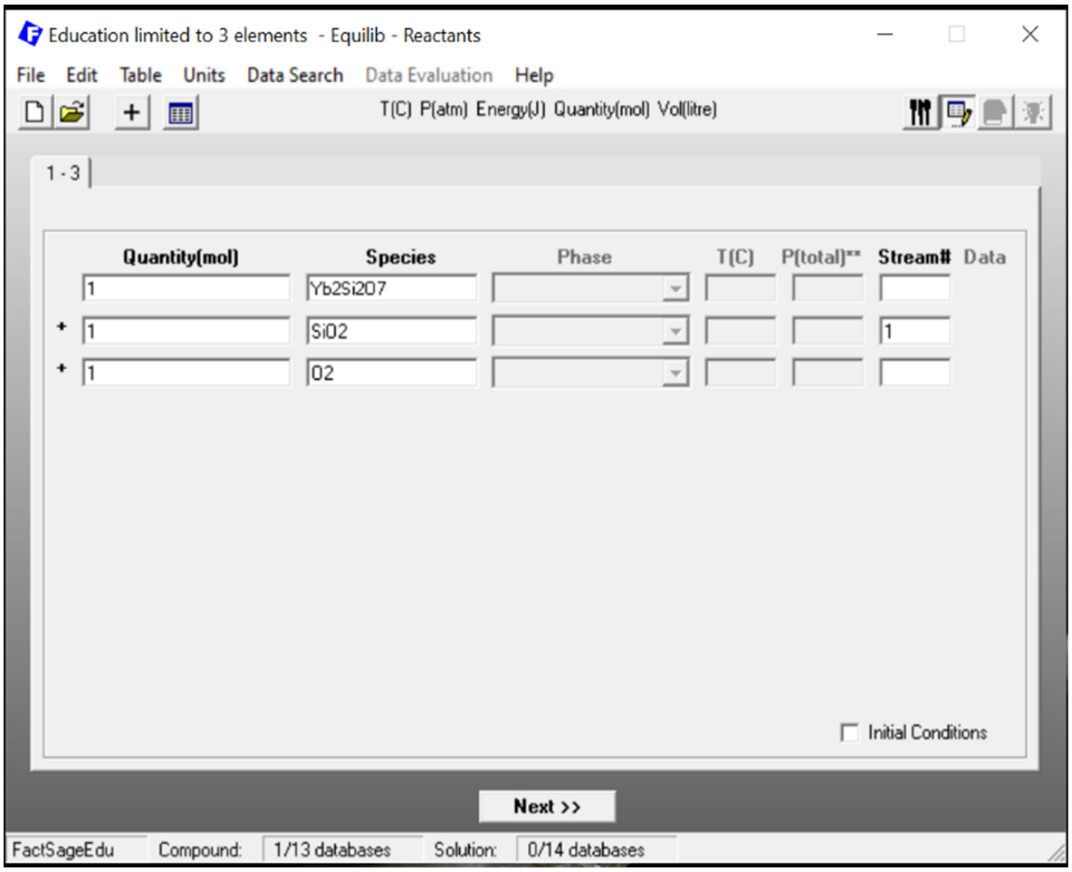

Figure A-1: FactSage Edu, insert the system to be studied.

Step2: Put the initial conditions (temperature and total partial pressure), also select the product type (solid/liguid/gas)

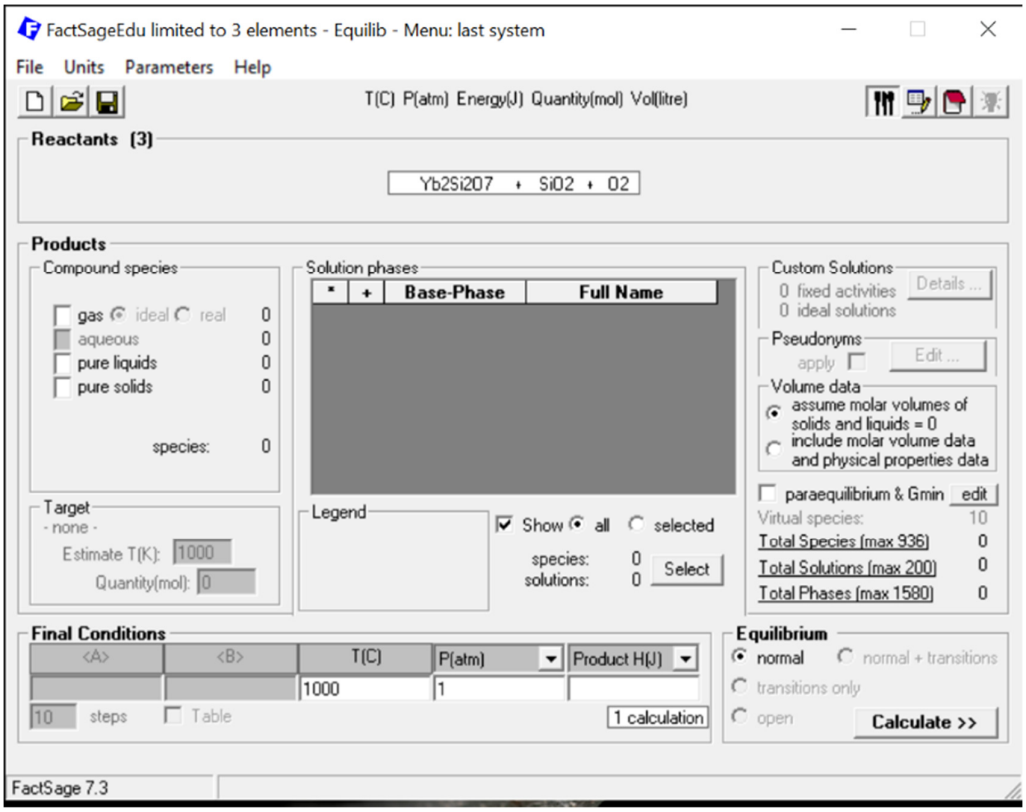

Figure A-2: Select the initial conditions (temperature and total partial pressure), and the product type (solid/liquid/gas).

Limitation with more than 3 elements!

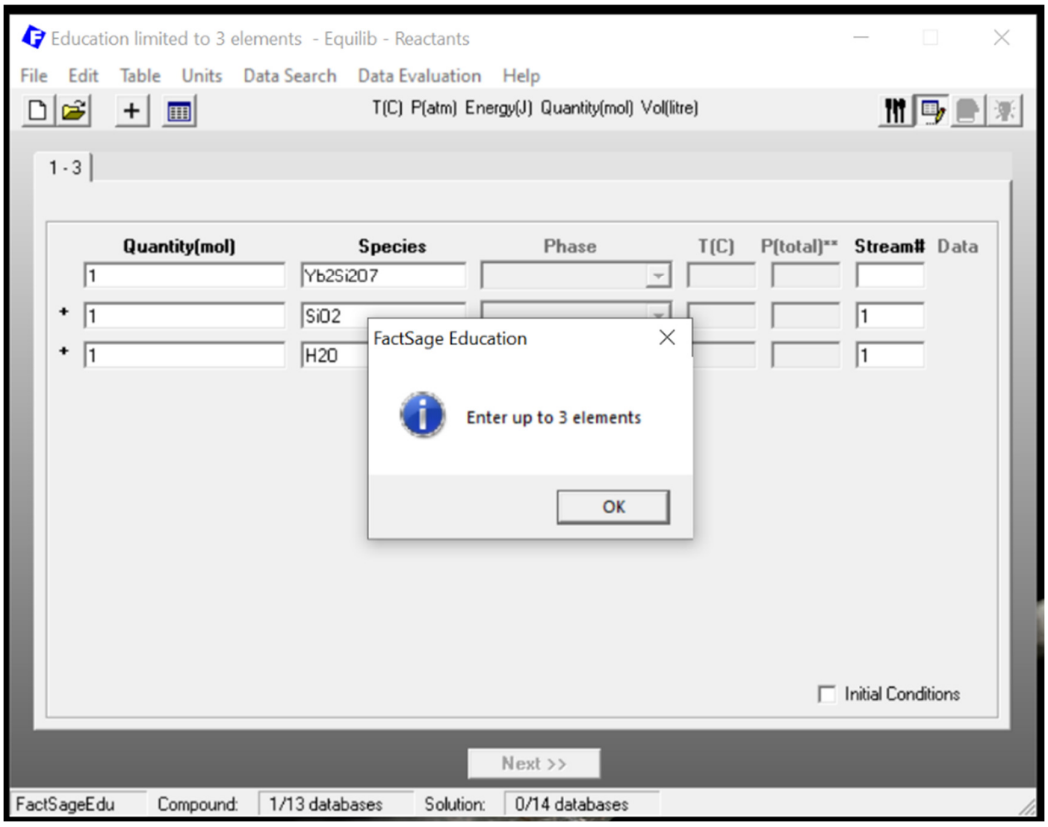

Figure A-3: Limitation with FactSage Edu (open software) is only 3 element system can be studied.

In reference to Figure 4-1

Table A-1: Percentage porosity in Top coat with variable composition for the wet oxygen condition (90% H_2O + 10% O_2) at 1589 K.

Top coat	**%age porosity (As-sprayed)**	**%age porosity (After 1000 cycles)**
Yb2Si2O7	6.866	4.956
6A	3.877	2.602

AT	4.632	3.115
M2Y	4.329	2.966

(a) $Yb_2Si_2O_7$ (As-sprayed)

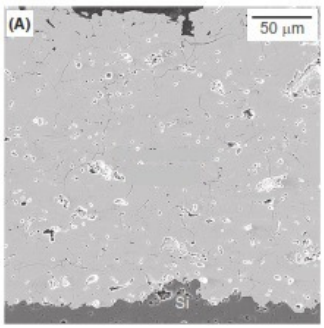

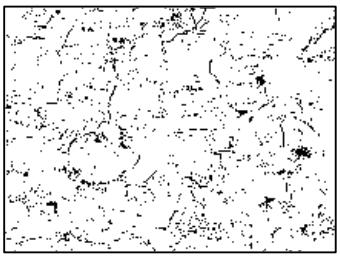

(b) $Yb_2Si_2O_7$,1000 cycles

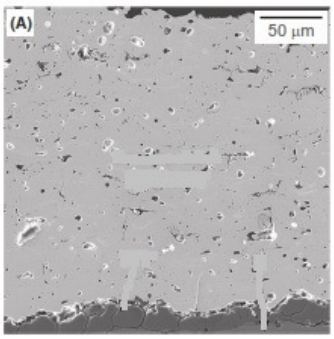

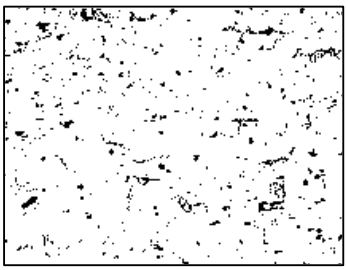

(c) 6A, As-sprayed

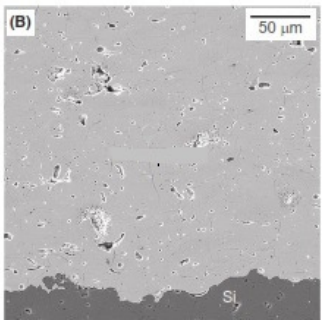

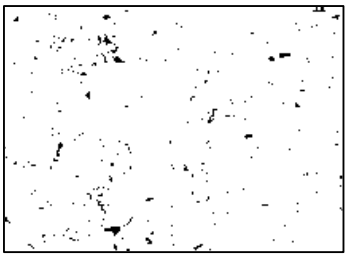

(d) 6A, 1000 cycles

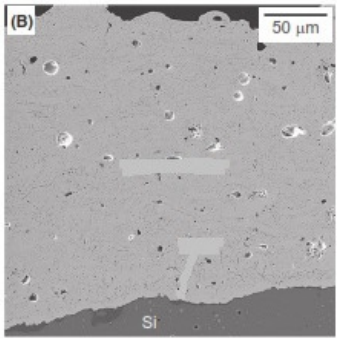

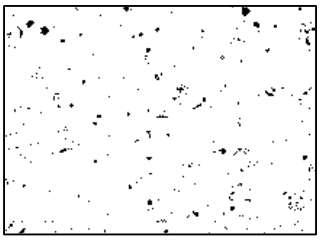

(e) AT, as-sprayed

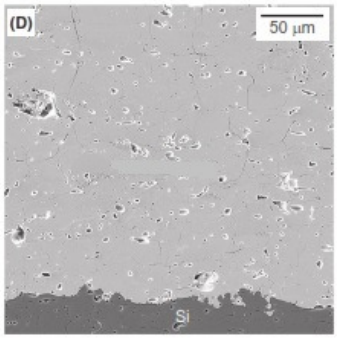

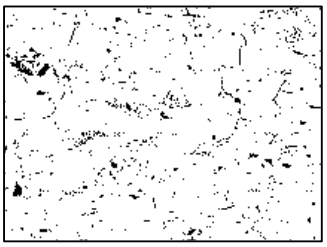

(f) AT, 1000 cycles

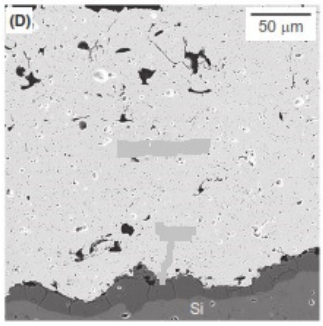

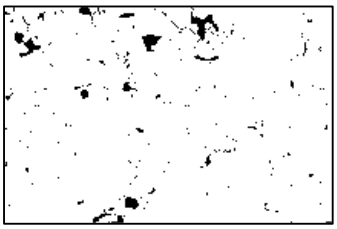

(g) M2Y, as-sprayed

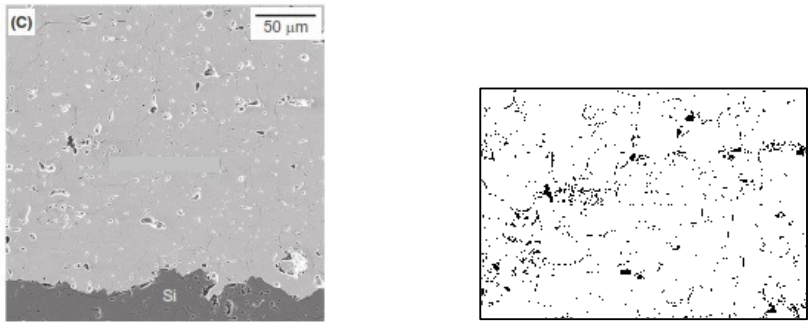

(h) M2Y, 1000 cycles

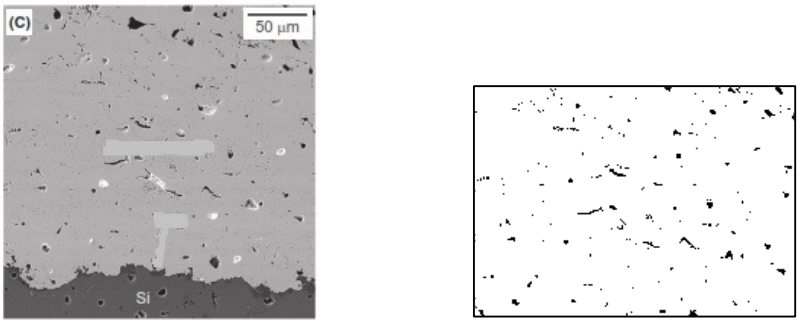

Figure A-4: Microstructure of Top coat as-sprayed and after 1000 cycles in the wet environments (90% H2O + 10% O2) at 1589 K, (a) Yb2Si2O7 (As-sprayed), (b) Yb2Si2O7,1000 cycles, (c) 6A, As-sprayed, (d) 6A, 1000 cycles, (e) AT, as-sprayed, (f) AT, 1000 cycles, (g) M2Y, as-sprayed, (h) M2Y, 1000 cycles [36].

In reference to Figure 4-2.

Table A-2: Oxygen permeability constant vs. temperature in dry oxygen conditions for diffusion through silicon dioxide (TGO) [69].

Temperature (Kelvin)	**10000/T (1/Kelvin)**	**Oxygen permeability constant (mol/m/sec)**
1345	0.74	$1.71*10^{-13}$
1372	0.73	$2.04*10^{-13}$
1395	0.72	$2.27*10^{-13}$

1419	0.70	$2.60*10^{-13}$
1443	0.69	$3.01*10^{-13}$
1469	0.68	$3.45*10^{-13}$
1496	0.67	$3.94*10^{-13}$
1523	0.66	$4.49*10^{-13}$
1552	0.64	$5.13*10^{-13}$
1582	0.63	$5.85*10^{-13}$
1613	0.62	$6.67*10^{-13}$
1645	0.61	$7.61*10^{-13}$
1678	0.60	$8.69*10^{-13}$
1713	0.58	$9.91*10^{-13}$
1750	0.57	$1.13*10^{-12}$
1788	0.56	$1.29*10^{-12}$
1827	0.55	$1.47*10^{-12}$
1869	0.54	$1.68*10^{-12}$
1912	0.52	$1.92*10^{-12}$
1958	0.51	$2.19*10^{-12}$
2005	0.50	$2.49*10^{-12}$
2055	0.49	$2.86*10^{-12}$
2108	0.47	$3.25*10^{-12}$
2163	0.46	$3.72*10^{-12}$
2166	0.46	$3.81*10^{-12}$
2224	0.45	$4.35*10^{-12}$
2286	0.44	$4.97*10^{-12}$

Table A-3: Parabolic rate constant vs. temperature in dry oxygen conditions [73], and the corresponding calculated Oxygen permeability constant for silicon dioxide.

T (Kelvin)	10000/T (K)	Parabolic rate constant, kp ($\mu m^2/hr$)	Oxygen permeability constant (mol/m/sec) (Equation C)
1071	0.93	0.00103	$1.05*10^{-14}$
1190	0.84	0.00463	$4.71*10^{-14}$
1271	0.79	0.0106	$1.08*10^{-13}$
1372	0.73	0.0253	$4.43*10^{-13}$
1496	0.67	0.0435	$6.11*10^{-13}$
1582	0.63	0.11	$1.63*10^{-13}$

In reference to Figure 4-3.

```
clc;
%% permeability versus oxygen partial pressure.
z = 0:1:6;
Y= ((10.^z)./(10.^-4));
T=1589;
R=8.314;
q=3/16; %% power on Yb ion
p= (-1/6); %% power on Oxygen ion
Ayb= 3.160*10^1.*exp(-388000./(R*T))/4;
Ao = 2.775*10^2.*exp(-420000./(R*T))/4;
 %% for Yb dominant permeability
Py = Ayb*(((((2.13*10.^z)).^q))-((1.165*10.^-4).^q));
%% for Oxide dominant permeability
```

```
Po = -Ao*(((((2.13*10.^z)).^p))-(((1.165*10.^-4).^p)));
%% total permeability
PT = Py+Po;
loglog(Y,PT);
```

In reference to Figure 4-4.

```
clc;
%% permeability versus oxygen partial pressure.
z = 0:1:6;
Y= ((10.^z)./(10.^-4));
T=1589;
R=8.314;
 q= (3/8); %% power on Yb ion
p= (-1/3); %% power on Oxygen ion
Ayb= 3.160*10^1.*exp(-388000./(R*T))/4;
Ao = 2.775*10^2.*exp(-420000./(R*T))/4;
%% for Yb dominant permeability
Py = Ayb*(((((9.13*10.^z)).^q))-((1.165*10.^-4).^q));
%% for Oxide dominant permeability
Po = -Ao*(((((9.13*10.^z)).^p))-(((1.165*10.^-4).^p)));
%% total permeability
PT = Py+Po;
 loglog(Y,PT);
```

In reference to Figure 4-5.

Table A-4: Oxygen permeability constant through YbDS top coat vs. temperature, calculated in wet conditions (0.50atm O_2+0.50atm H_2O), different temperatres and 200 hr exposure time.

Temperature (Kelvin)	**Equation B**	**Equation A (p= -1/3,q=3/8)**	**Equation A (p= -1/6,q=3/16)**
1423	$4.89*10^{-12}$	$3.23*10^{-11}$	$1.19*10^{-12}$
1473	$7.33*10^{-12}$	$4.43*10^{-11}$	$3.4*10^{-12}$
1523	$9.78*10^{-12}$	$6.00*10^{-11}$	$9.04*10^{-12}$
1573	$1.4*10^{-11}$	$7.95*10^{-11}$	$2.26*10^{-11}$

In reference to Figure 4-9.

```
clc;
%% permeability versus oxygen partial pressure.
T=1589;
R=8.314;
p= (-1/3); %% power on Oxygen ion
q= 3/8; %% power on Yb ion
Ayb= 1.09*10^2.*exp(-619200./(R*T))/2;
Ao = 5.11*10^-2.*exp(-288350./(R*T))/2;
%% for Yb dominant permeability
Py = Ayb*(((((9.12*10.^4)).^q))-((1.17*10.^-4).^q));
%% for Oxide dominant permeability
Po = -Ao*(((((9.12*10.^4)).^p))-(((1.17*10.^-4).^p)));
%% total permeability
PT = Py+Po;
```

In reference to Figure 4-6 and Figure 4-7.

```
clc;
T=1589:100:1973;
z = (10000./T);
R=8.314;
Ayb= 1.09*10^2.*exp(-619200./(R*T))/2;
Ao = 5.11*10^-2.*exp(-288350./(R*T))/2;
Loglog (z,Ao,z, Ayb);
legend ('Al','Oxygen');
axis ([5.1 6.4 10^-14 10^-8])
```

Table A-5: Total oxygen permeability constant through YbDS top coat vs. temperature, calculated using equation A and equation B for different environment conditions at 200 hr and 1250^{o}C[66].

Oxygen Partial pressure	**Equation B**	**Equation A (p= -1/3,q=3/8)**	**Equation A (p= -1/6, q=3/16)**
10%H_2O+90%O_2	$4.85*10^{-11}$	$1.19*10^{-11}$	$1.75*10^{-11}$
50%H_2O+50% O_2	$5.69*10^{-11}$	$5.99*10^{-11}$	$9.04*10^{-12}$
90%H_2O+10% O_2	$1.53*10^{-10}$	$1.08*10^{-10}$	$1.49*10^{-12}$

Curve fitting:

```
clc;
x=[1423 1473 1523 1573 1589];
y=[1.25*10^-10 1.84*10^-10 2.36*10^-10 3.19*10^-10 3.46*10^-10];
```

```
Plo=[1.10*10^-6 5.02*10^-6 2.07*10^-5 7.76*10^-5 1.17*10^-4];
Phi=5.07*10^4;
p=-1/3;
q=3/8;
R=8.314;
f = @(b,x) -b(1)*exp(b(2)./(x*R)).*((Phi.^p)-(Plo.^p))+ b(3)*exp(b(4)./(x*R)).*((Phi.^q)-(Plo.^q));
B = fminsearch(@(b) norm(y-f(b,x)), [277.5; -388000; 105; -400000])
figure
plot(x,y,'pg')
hold on
plot(x,f(B,x),'-r')
hold off
grid
xlabel('x')
ylabel('f(x)')
%%text(27, 105, sprintf('f(x) = %.1f\\cdote^{%.3f\\cdotx}%+.1f', B))
```

In reference to Figure 4-11.

Table A-6: The top coat oxygen permeability constant for YbDS with modified YbDS at 1589 K in 90% H_2O + 10% O_2 at 1000 hrs exposure time.

Top coat	$\tilde{V}_{SiO2}$ **(m^3/m^2)**	$\frac{\tilde{V}SiO2\ (\frac{m3}{m2})}{t}$	**Oxygen permeability constant, TC (mol/m. sec)**
$Yb_2Si_2O_7$	$13.2*10^{-6}$	$1.32*10^{-8}$	$3.36*10^{-11}$

6A	$1.9*10^{-6}$	$1.9*10^{-9}$	$4.85*10^{-12}$
M2Y	$1.7*10^{-6}$	$1.7*10^{-9}$	$4.34*10^{-12}$
3M	$2.5*10^{-6}$	$2.5*10^{-9}$	$6.38*10^{-12}$
2Y	$3.7*10^{-6}$	$3.7*10^{-9}$	$9.44*10^{-12}$
M5Y	$2.4*10^{-6}$	$2.4*10^{-9}$	$6.12*10^{-12}$
M	$16.3*10^{-6}$	$1.63*10^{-8}$	$4.16*10^{-11}$
AT	$10.0*10^{-6}$	$1.0*10^{-8}$	$2.55*10^{-11}$
MT	$10.8*10^{-6}$	$10.8*10^{-9}$	$2.75*10^{-11}$

*Calculated using equation B.

In reference to Figure 4-12.

Table A-7: Oxygen permeability constant for TGO and TC at 1589K, in 90% H_2O + 10% O_2, after 1000 hr exposure time [36].

Top coat	**TGO (mol/m. sec)**	**Oxygen permeability constant, TC (mol/m. sec)**
$Yb_2Si_2O_7$	$1.87*10^{-12}$	$3.36*10^{-11}$
6A	$3.61*10^{-14}$	$4.85*10^{-12}$
M2Y	$3.21*10^{-14}$	$4.34*10^{-12}$
3M	$2.97*10^{-14}$	$6.38*10^{-12}$
2Y	$1.68*10^{-13}$	$9.44*10^{-12}$
M5Y	$5.39*10^{-14}$	$6.12*10^{-12}$
M	$2.70*10^{-12}$	$4.16*10^{-11}$
AT	$1.04*10^{-12}$	$2.55*10^{-11}$
MT	$1.43*10^{-12}$	$2.75*10^{-11}$